Progress in Materials Science 85 (2017) 1–42

Contents lists available at ScienceDirect

Progress in Materials Science

journal homepage: www.elsevier.com/locate/pmatsci

A revisit to atomistic rationale for slip in shape memory alloys

Piyas Chowdhury, Huseyin Sehitoglu *

Department of Mechanical Science and Engineering, University of Illinois at Urbana-Champaign, 1206 W. Green St., Urbana, IL 61801, USA

ARTICLE INFO

Article history:
Received 13 July 2016
Received in revised form 23 September 2016
Accepted 25 October 2016
Available online 4 November 2016

Keywords:
Shape memory
Plastic deformation
Dislocation
Generalized stacking fault energy
Critical resolved shear stress
Density functional theory

ABSTRACT

Performance degradation in shape memory alloys (SMA) arises due to a gradual loss of strain recoverability attributable to slip mediated plasticity. The slip-induced changes in SMAs can be profound creating accumulation of permanent strains, altering the critical stress and hysteresis in an adverse manner. Slip nucleation in ordered SMA lattices can often be triggered due to energetically favorable dissociation reactions. Partial slip can dominate over full slip, generating planar defects (e.g. anti-phase boundary, superlattice or complex stacking faults) as evidenced through electron microscopy. Considerable advances are made lately on physically rationalizing the observed plastic micromechanism(s) benefitting from quantum mechanical models. In-depth analyses of crystal variables (e.g. lattice ordering, atomic stacking and stable/metastable fault structures) subjected to intrinsic solid-state effects have unequivocally established the genesis of empirical slipping propensity in terms of atomic fault energetics. This article systematically revisits the empirical physical evidence of slip in important SMAs from the literature, presents the pertinent experimental findings, and then embarks on reviewing the investigations of atomistic studies as exemplified by the authors' group. In closing, we discourse on the potential use of lattice scale theories in devising other important structure-property relationships such as role of precipitates, cracking resistance, constitutive modeling.

Contents

* Corresponding author.
E-mail address: huseyin@illinois.edu (H. Sehitoglu).

http://dx.doi.org/10.1016/j.pmatsci.2016.10.002
0079-6425/

Nomenclature

PN	Peierls-Nabarro
SMA	shape memory alloy
TEM	transmission electron microscopy
ECAE	equal channel angular extrusion
DFT	density functional theory
MD	molecular dynamics
GSFE	generalized stacking fault energy
CRSS	critical resolved shear stress
APB	anti-phase boundary
NNAPB	nearest neighbor APB
NNNAPB	next nearest neighbor APB
CSF	complex stacking fault energy
SISF	superlattice intrinsic stacking fault
A_s	austenite start temperature
A_f	austenite finish temperature
M_s	martensite start temperature
M_f	martensite finish temperature
M_d	highest temperature above which martensite transformation cannot be stress-induced
a	lattice constant of an SMA lattice (e.g. for B2 NiTi, a^{B2}_{NiTi})
$\underline{a}'$	lattice periodicity
b	Burgers vector
d	distance between two partial dislocations
γ	fault energy
γ_{us}	unstable stacking fault energy
γ_{isf}	intrinsic stacking fault energy
γ_{CSF}	complex stacking fault energy
γ_{APB}	anti-phase boundary energy
γ_{NN}	nearest neighbor anti-phase boundary energy
γ_{NNN}	next nearest neighbor anti-phase boundary energy
ζ	dislocation core half-width
υ	Poisson's ratio
u	shear displacement
x	position of a dislocation
$f_{disregistry}$	disregistry function
τ_{ideal}	idea shear strength
τ^{slip}_{CRSS}	critical resolved shear stress (CRSS) for slip nucleation

1. Introduction

1.1. Significance of plasticity in SMAs

Shape memory alloys possess a unique mechanical attribute of fully recovering large strains upon proper thermo-mechanical cue [1,2]. Such ability empowers SMAs as excellent multifunctional actuators in diversified industrial applications [3–5]. The extraordinary shape recoverability is rooted upon a reversible crystal transformation process i.e. austenite $\rightleftharpoons$ martensite [6,7]. In its service lifetime, an SMA-made engineering component is designed to undergo a number of load-unload cycles. Performance degradation would be elicited at any stage of the thermo-mechanical deformation pathways if the extent of dislocation slip reaches a damaging level [8–10]. Vital to maintaining protracted SMA functionalities is the safeguarding of two-way phase transformability while minimizing the irreversible deformations [11–14]. The SMA slipping propensity is a pressing issue restraining their prospects of high temperature applications [15,16]. Specifically, the possibility of widespread thermal activation of dislocations poses a critical design constraint in the hot section components [17–19], for example. From fabrication standpoint, it is desirable to have very high slip resistance both in austenitic and martensitic crystals in addition to low transformation and twinning stresses, and high recoverable strain [20–22]. To that end, developing predictive abilities for assessing the inherent slip propensity in SMA phases would be particularly worthwhile. In this article, we present a review of the literature in that regard, which deal with discrete lattice effects.

The manifestation of slip in SMAs can be a complex phenomenon to characterize particularly for a polycrystalline microstructure. It is well known that nominal plastic yield stress (as measured from the laboratory-scale constitutive responses) is much greater than the transformation stress in SMAs [23,24]. Plastic yielding in the pseudoelastic stress-strain curves, for example, is noted at macroscopic stress levels well beyond the martensitic transformation-induced stress plateau (i.e. followed by elastic deformation and detwinning of martensite). However, at a far lower stress than the manifested global plastic yield, considerable slip in conjunction with transformation can occur microscopically [25–27]. Such early co-existence of slip and martensite, it is inferred, may arise in order to satisfy strain compatibility across the austenite-martensite periphery. Microscale slip activities, despite sometimes not demonstrably giving rise to strain irreversibility on the global scale, would cause subtle yet incremental effects. For example, the reduction in transformation stress, strain and hysteresis as well as the overall instability of cyclic superelasticity are reported as the outcomes of the small-scale slipping in concurrence with transformation domains [28–30]. Ex-situ observation of dislocations relics in the deformed polycrystalline microstructure attests to these conclusions. We will elaborate more on this issue with a specific example considering NiTi SMA in Section 4.

The fact that the macroscale plastic yielding is not indicative of the actual initiation of microscale dislocation activities points to the dominant roles of mesoscale factors [31,32]. For instance, local preferential sites such as grain boundaries, triple joints may pave the way for reaching high localized stress conducive to dislocation slip. Some grains could be specifically susceptible to slipping while others not. However, it is undeniable that the intrinsic slipping propensity (in terms of overcoming shear energy barriers at the atomistic level) of a certain lattice type should be unique. The mesoscale factors are merely the instigators for initiating plastic flow and its interaction with transformed material. Predicting slip predisposition by considering combined effects of all mesoscale variables (e.g. grain size, texture, interface, residual martensite) remains a prominent modeling objective [33,34]. In this regard, it would be particularly worthwhile to assess the plastic strength of a certain phase in its pristine and isolated form i.e. free of other mesoscopic influences. Specifically, such an approach can establish the intrinsic shear resistance of a crystal structure by establishing the slip energy barriers, say, from first principles. To that end, we have at our disposal the quantum mechanics based simulation tools addressing the sub-nanometer length-scale phenomena [35,36]. In this article, we discuss the state of the art on computing the slipping energetics and their

utilization in predicting Peierls stresses. Such modeling endeavors essentially constitute the first step, we argue, towards understanding the role of slip on influencing the SMA behaviors.

1.2. Importance of capturing atomistic energetics

Regarding the material slip tendency, one of the most significant information that one can extract from discrete lattice is the Peierls energy valley [37,38]. The so-called γ surface (also known as generalized stacking fault energy, GSFE) represents [39] the Peierls energy landscape for slip for a specific plane/direction [40,41]. It can be computed upon rigidly shearing two crystal blocks, and tracking their free energy differentials. The peak energy encountered for a certain slip system (i.e. a specific set of plane and direction) is termed "unstable stacking fault energy" and denoted γ_{us} [38]. In our subsequent discussion, we utilize the computed γ_{us} (from first principles) to compare strengths of various slip systems. Dislocation slip in an otherwise perfect crystal is associated with a non-dilatational shear, the magnitude of which is given by its Burgers vector [42,43]. For example, a very low energy barrier to create the corresponding shear displacement would make slip nucleation spontaneous. The exact topography of the Peierls energy surface depends on: (a) the crystal lattice structure and (b) effects of alloying [37,44,45].

In a certain crystal lattice, very specific sets of planes and directions offer the lowest energy barriers for shearing, which are typically the mostly densely packed ones [40]. Effects of alloying on slipping in a multi-element lattice are a function of bonding length/strength and material anisotropy. Evidently, this behavior is unlike that in pure metals (e.g. pure fcc metals) where, for example, critical resolved shear stress (CRSS) for a specific family of slip system remains the same [42,46]. The most influential lattice scale variables that would dictate the γ surface are related to the underlying solid-state effects. For example, the outcomes of mixing diverse elements would be dictated by the physical factors such as: (i) the relative atomic volumes [47,48], (ii) the intrinsic magnetic characteristics [49,50], (iii) the valence shell electronic configuration [51,52], and (iv) the short/long range atomic ordering [53,54]. To illustrate, if the solute atoms from different chemical species have substantial volumetric mismatch, a strong elastic stretching would be created, which would ultimately influence lattice-shearing resistance. The magnetic attributes (as largely controlled by the electronic spin properties) of individual chemical species would strongly contribute to the bonding energy landscape. It should be noted that majority of the SMAs consist of transition metals whose bonding characteristics are direct consequences of partial or full occupation of the outermost shell d orbitals [35]. All the foregoing sub-lattice considerations are very important to understand SMA properties, in that their combined influences would determine the exact nature of the γ surface [55].

While the computed γ surface serves as an energetic indicator of inherent slip propensity, further meso-scale normalizations could be adopted, for example, to predict the exact CRSS levels for a specific slip system [56–59]. This can be accomplished within the conditions of generic Peierls-Nabarro framework [60,61] with the γ surface as the most vital input. Given the importance of the SMAs in technological sectors (e.g. stents in biomedical industries, torque tubes in aeronautical structures), we envision that the currently emerging atomistics would uncover the physical origin of SMA behaviors and eventually contribute to enhancing their further applications (Fig. 1). With advent of the modern quantum mechanical models, it is necessary to make the most of these tools at our disposal to work towards linking multiple lengthscale phenomena [62]. By elaborating on recent works, we hope to instigate further research, which can address the outstanding issues in the

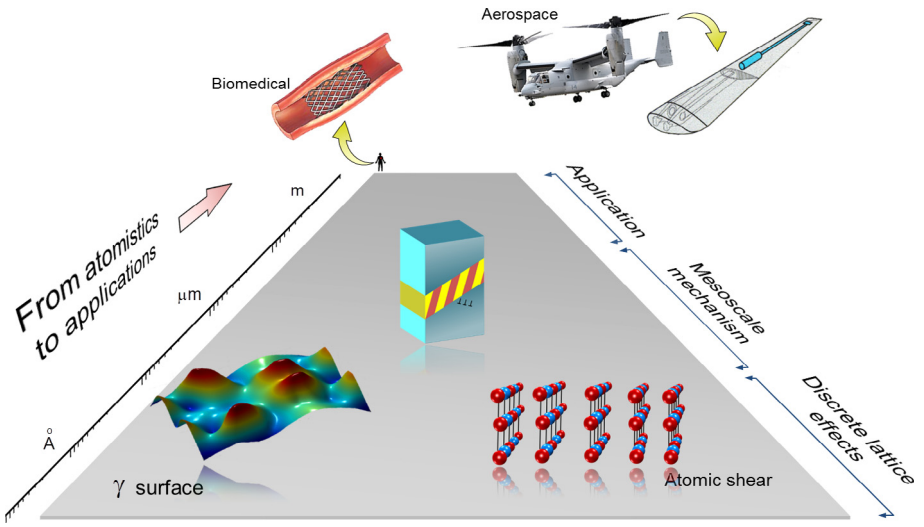

Fig. 1. A perspective on the broad objective and the associated lengthscales of atomistic modeling of slip in SMAs. The discrete lattice based predictions are envisioned to ultimately lead to important technological innovations by reducing the experimental trial-and-error in the long run.

SMA field in a concerted effort by materials and mechanics communities. We discuss the state of the art drawing from important case studies on Ni-Ti, Ni-Ti-Pt, Ni-Ti-Pd, Ni-Fe-Ga, Ni-Ti-Hf and Ti-Nb based SMAs in contemporary literature.

2. Overview of general SMA mechanical behaviors

Prior to delving into the discussions of plasticity-induced performance deterioration, it is instructive to briefly overview the SMA mechanical responses and the associated sub-structural phase changes. Slip can affect any of these responses. On the basis of existing literature, we provide Fig. 2 detailing a comprehensive map of constitutive responses, the associated microstructural changes and the critical stresses demarcating them.

2.1. Mechanical attributes of SMAs

2.1.1. Shape memory effects

The shape memory effect consists of applying a mechanical load followed by a heating and then cooling [63,64]. In Fig. 2, the green loop represents loading of twinned martensite to form a detwinned one and its unloading. The residual strain can be recovered by heating the detwinned martensite (above A_f) where it becomes austenite again, and then cooling it to the initial temperature (below M_f). At temperatures lower than M_f (i.e. martensite finish temperature), the crystal structure becomes a twinned martensite [65]. It is a self-accommodated internally twinned martensite lattice [66,67]. On applying stress, the material reaches a critical stage where the twinned martensite starts becoming de-twinned. At this stage, one twin variant starts growing in thickness at the expense of other variants, eventually to become one fully de-twinned variant [68,69]. This de-twinned variant does not revert to the original self-accommodating structure on the removal of stress only. Also, the residual strain is not recovered. One has to apply heat slowly at a constant stress until the temperature is above A_f (i.e. austenite finish temperature). It should be noted that a single variant martensite does not create a habit plane with the austenite. Thus, it first becomes a multi-variant self-accommodated structure, which eventually transforms into austenite. As a result, the entire strain is recovered. The blue loop in Fig. 2 is referred as the isobaric shape memory effect. In such an effect, heating and cooling at a constant stress causes a two-way transformation and strain recovery. The foregoing behaviors and the associated sub-structural modifications have all been verified experimentally.

2.1.2. Superelasticity

Another important constitutive behavior characteristic of SMAs is the superelasticity (also known as pseudoelasticity) [70–72]. Superelasticity can be defined as complete recovery of forward transformation-induced macroscale strain upon

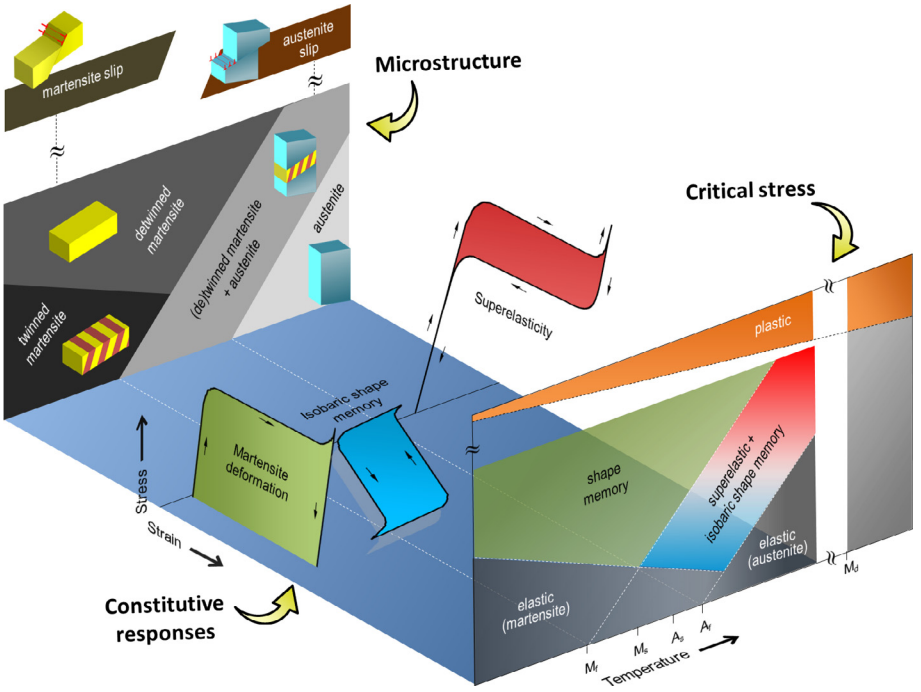

Fig. 2. A schematic map of SMA mechanical responses in stress-strain-temperature space, the associated microstructural phase transitions and the critical stresses marking the transition from one phase to another. Three distinct constitutive responses are expected of SMAs: (i) shape memory effects, (ii) isobaric shape memory behaviors and (iii) superelasticity. Underlying these responses are the reversible martensitic transformations and twinning/de-twinning processes. Critical stress for initiating plasticity is typically higher than that of transformation or twinning.

removal of stress (under isothermal condition) [73–75] due to reversibility of transformation. In Fig. 2, the red loop describes the superelastic response of SMAs. This occurs at temperature well above the A_f (i.e. when the structure is austenitic under zero mechanical load). At the sub-structural level, the material transforms from austenite to martensite (comprising twinned variants) during loading, often accompanied by other intermediate phases [76,77]. During unloading, reverse transformation occurs spontaneously since martensite is stable at such temperatures only under stress. Thus, removal of stress triggers martensite-to-austenite transition [78]. Consequently, the strain imposed during the loading is fully recovered upon unloading. Now, it is important to note that various shape memory materials would have different crystal structures at individual stages [79]. The behaviors described in Fig. 2 are the most generic ones. Therefore, a map of shape memory effects, elastic deformation (of martensite or austenite) and superelasticity and isobaric shape memory effects is presented in terms of the critical stress to initiate the associated phase transitions. It is also indicated that the plastic deformation is expected to occur at much higher critical stress levels, which also decreases with rising temperature. However, given the nature of the transformed microstructure, there will always be some phase and/or grain boundaries, which would act as preferential sites for slip nucleation. Gradually, the slip would accumulate at these microscopically stressed domains. As a result, the shape recovery attributes would be compromised at the macroscale [80,81].

2.1.3. Critical stresses

The 'critical stress' for any microstructural change is an important parameter, which demarcates a transition from one sub-structure to another such as phase transformation, slip nucleation, twinning etc. (Fig. 2). It also constitutes a vital metric for comparing the overall SMA mechanical performance. Ideally, the stresses for initiating various phase transformations should be considerably lower compared to that of slip based mechanism. However, the determination of the precise critical stresses for initiating slip in austenite or martensite could prove a complex task. As explained earlier, on the macroscopic stress-strain curves, the plastic yielding of austenite or martensite is noted at high temperature (at and above Md) and high stress (beyond the usual transformation plateau) respectively. Microscopically, considerable presence of slip, however, can be noticed in either phase at considerably lower stress than the nominal yielding. At this stage, the phase transformation is the predominant deformation mechanism with interspersed dislocation activities. The occurrence of microscopic slip activities can be attributed to a myriad of mesoscale factors (e.g. straining of interfaces, high stress localization in grains, self-accommodated structure for the case of martensite). Thus, an unequivocal assessment of critical plastic strengths of austenitic or martensitic (i.e. in their isolated defect-free condition) could prove challenging on experimental grounds. Furthermore, such an evaluation ought to be conducted at the same temperature as well as under the same microstructural condition. To that end, predicted critical stresses of slip (i.e. Peierls stress) in individual phases (free of mesoscale variables) can be particularly useful as we will discuss next.

As indicated in Fig. 2, the propensity of plastic deformation also increases with gradual elevation of temperature. Beyond a critical temperature (M_d), the SMAs behave like conventional metallic alloys, which deform by slip based mechanisms (i.e. no phase transformation whatsoever) [1]. The importance of determining these critical stresses can be of considerable importance [82], in that knowing their magnitude could assist in formulating better alloy design during manufacture stage. In this article, we will describe how the critical slip stresses to nucleate dislocation in various SMA lattices can be predicted using atomic-scale fault energies within Peierls-Nabarro formalism.

2.2. Slip-induced deterioration in SMA mechanical responses

Fig. 3 demonstrates how the slip-induced performance compromise would be reflected on isobaric shape memory effect and superelastic global constitutive behavior. The isobaric shape memory loops as discussed previously originate from cycling the temperature across the spectrum of the transformation temperatures (i.e. M_f and A_f). In the cycling process, the strain is fully recovered due to complete forward and reverse transformations. However, with increased number of cycles as well as at higher applied stress, it would become more likely to accrue localized slip at favorable microscopic sites (e.g. grain/phase boundaries, structural inhomogeneities, inclusions) [83–85]. The isobaric loops will thus be affected by the plastic strains in the form of non-closure during a full thermal cycle (Fig. 3). Similarly, the superelastic loops are inflicted with plasticity, resulting in residual strain upon complete unloading [9] as a consequence of multiple cycles, high temperature and strain-rate [23,86–88]. Plastic strains are increased with rising number of cycles and temperature [89–91].

3. Characterizing intrinsic material resistance to permanent deformation

3.1. Mesoscale factors and pristine behaviors of a single grain

In most engineering applications, the components made of SMAs have polycrystalline microstructure consisting of multiple grains. As noted earlier in the introduction section, the occurrence of dislocation slip is not contingent upon reaching the plastic yield point on the macroscale constitutive response [25–27]. Several mesoscopic factors can facilitate early slip nucleation during the martensitic transformation stage of deformation. For example, the necessity of strain accommodation at the incoherent interface between the twinned martensite and the parent austenite is one of the most likely causes of slip nucleation [92,93]. Mutually constrained grains can also generate high local stress exceeding the yield strength of either

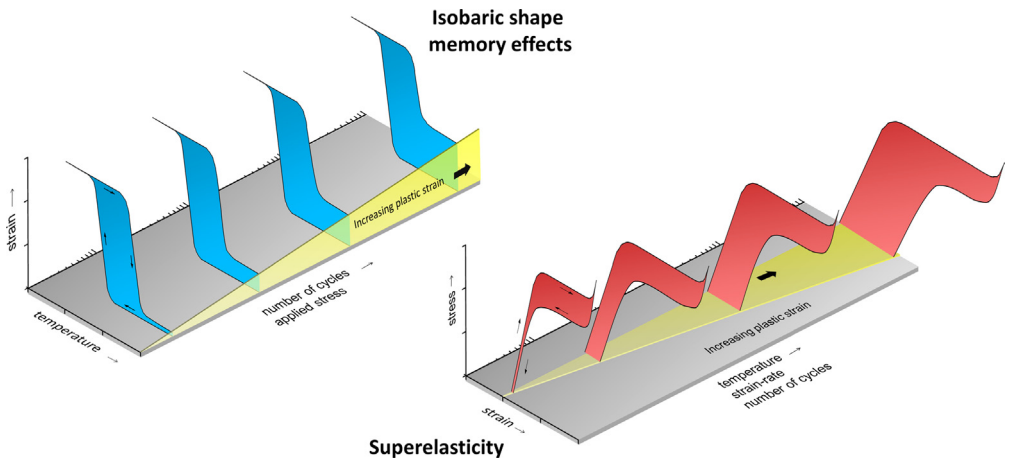

Fig. 3. Accumulation of plastic strain resulting in the deterioration of isobaric shape memory effects and the superelastic loops during experiments due to increasing number of cycles, applied stress and strain-rate.

phase thus triggering localized slip. Such dislocations can glide and transfer across the grain boundaries to reach other grains predominated by transformed domains. Generation of slip in such manners does not cause macroscopic yielding; however, they do affect the mechanical behavior significantly. It is conjectured that localized slipping assists in the retention of residual martensite at unloaded state. The combined effect of residual plastic and transformed material gives rise to the functional fatigue of many SMAs. From modeling standpoint, isolating the sole contribution of slipping is compounded due to the symbiotic nature of all mesoscopic factors in a polycrystalline microstructure.

A theoretical analysis of multi-grain structure would invariably involve investigating the role of texture, the grain size, the interface type and distribution, etc. [94–99]. While these factors are important, it would be more advantageous to begin theorizing an isolated single grain first [24,100–102]. With a view to establishing the actual plastic strength of a certain phase, the inherent slipping propensity can most conveniently be assessed under pristine condition. Of course, one can build upon the defect-free behavior, and develop theories delineating the intricate roles of other important mesoscale factors (e.g. grain orientation and boundaries, precipitates). We will discuss the latter issues towards the end of this article. First, we expound on how predictions based on a single crystal can be useful in understanding the slip response of a defect-free lattice.

Let us consider a most likely scenario of how slip may initiate in an SMA microstructure. Fig. 4 presents a closer inspection inside a grain from a generic polycrystalline SMA where the initial austenitic crystal is transforming into a martensitic one. The martensite consists of multiple twin-matrix pairs [103], i.e. variants. With the increasing volume fraction of martensite, the prevalence of twin boundaries is also augmented proportionately. In addition to the austenite-martensite interface (i.e. the habit planes) and grain boundaries, these twin boundaries would constitute localized domains of high internal stresses. Slip is most likely to initiate at these interfacial defects [9,104] despite the global stress state being well below the plastic yield point. While the highly stressed domains can serve as active sources, the subsequent accumulation and propagation of dislocations would be decided by the slipping resistance of the bulk material. This bulk slip resistance is what the atomistic calculations can uncover.

The slip nucleation demarcates the transition of deformation mechanism from a transformative or an elastic mode to a plastic one. Atomistically, this is equivalent to a situation where applied stresses help to overcome the Peierls energy barriers. At the discrete lattice level, the intrinsic frictional resistance of the individual phases would decide the extent of plastic deformation. Intuitively, the phase with lower impedance to slipping would be subjected to the greatest plastic damage. It is desirable that both austenitic and martensitic phases possess high slip energy barriers compared to transformation. Thus, any predictive measure indicating their relative plastic strengths would be immensely worthwhile. On theoretical grounds, quantification of respective energy pathways can facilitate such an achievement. In the next sections, we embark on discussing the slip energetics computed for various SMA phases and their significance.

3.2. γ surface and first principles

The fundamental steps of computing γ surface from density functional theory (DFT) involves [105]: (i) identification and creation of the stable, meta-stable or unstable structures, (ii) constructing the lattice space with atoms of various elements, (iii) configuring the elemental attributes (i.e. magnetism, chemical potential, electron exchange-correlation attributes) [56–59,106,107]. The DFT can account for these attributes. Computation of the γ energy landscape is performed by a rigid shear method [39]. In such an approach, the accurate prediction of the fault energetics relies on the solution of electronic charge densities of each valence electron for each atom [108]. As in Fig. 5, two crystal half-spaces are rigidly sheared with respect to each other with small increments of displacements. The first step is to determine the material slip plane and direc-

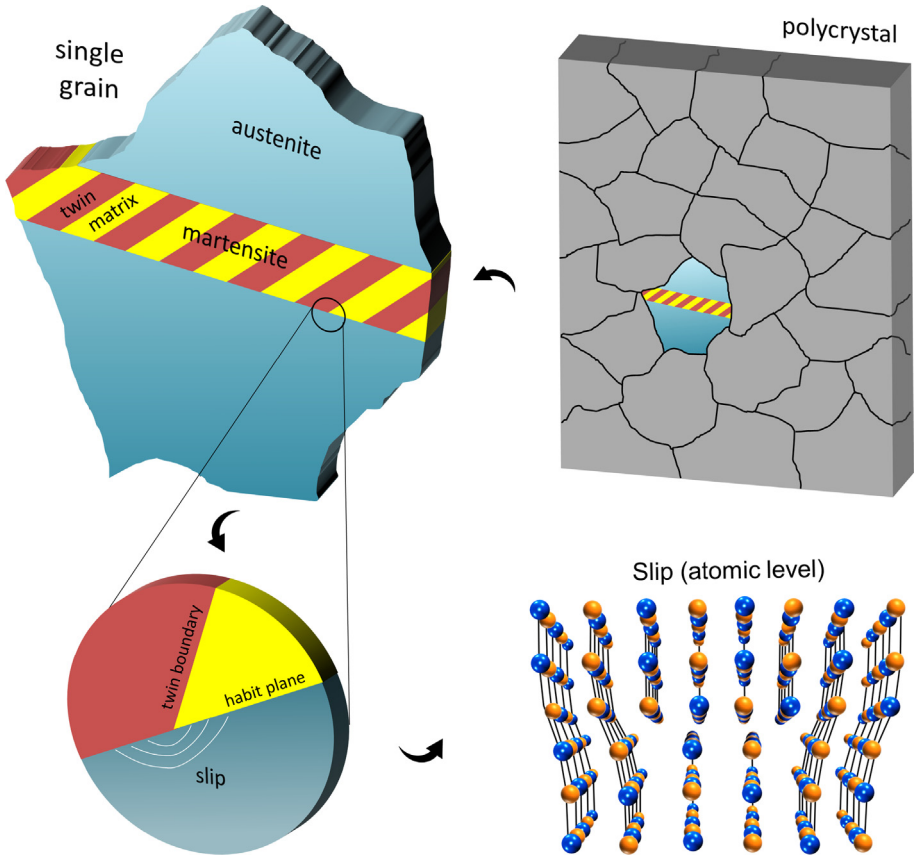

Fig. 4. Microstructure in real-life SMA components is polycrystalline in nature, where slip would emanate from local highly stressed sites (e.g. interfaces). Theorizing atomistic slip propensity in single crystals is an important first step towards understanding multi-grain behaviors involving roles of interface types, distribution, etc., which is outlined in the conclusion section of this article.

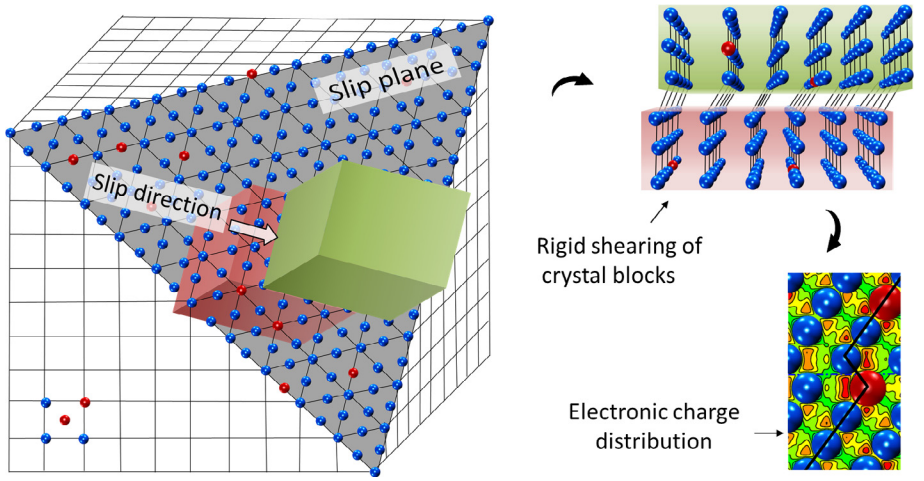

Fig. 5. The γ surface can be computed from density functional theory (DFT) simulations by shearing two adjoining crystal blocks for a specific slip system (i.e. on a certain plane along a certain direction). DFT calculations rely on the accurate solutions of the electronic charge distribution to generate fault energetics [108].

tions. The adjoining plane between these two blocks is the slip plane and the relevant direction to which one block should be displaced is the slip direction. Now, such type of rigid shear would essentially result in the simultaneous breaking all the atomic bonds across the slip plane. When the incremental displacement becomes equal to a Burgers vector, the total energy

pathway represents the energy expenditure to create such an amount of shear. This situation corresponds to overcoming ideal shear strength (τ_{ideal}) of materials. However, it is well accepted today that the creation of a dislocation slip necessitates much less stress than the τ_{ideal}. Atomistically, a perfect edge dislocation can be envisioned as the end line of an extra half plane inserted into an otherwise perfect lattice. The creation of the slip would result in the shearing of the lattice by an amount equal to the Burgers vector magnitude. Unlike the rigid shear case, however, this essentially involves much less mechanical force. The requisite critical resolved shear stress for slip nucleation (τ_{CRSS}^{slip}) is thus considerably lower than the ideal level. Nevertheless, the energy pathway to create a shear step equivalent to the Burgers vector is the first step to model slip nucleation stress. The γ energy profile in conjunction with further elastic distortion considerations are crucial input to predict the τ_{CRSS}^{slip} levels accurately (more detailed discussions provided in Section 11). In terms of uncovering the exact nature of the γ surface in various SMA phases, the density functional theory (DFT) [105,109] has presented itself as the most appropriate toolset.

The DFT simulations are about finding solutions to bonding electron densities from the Schrödinger equation. The thermodynamic observables (e.g. entropy, free energy) are constructed as the mathematical functionals of electron density [110,111]. Conventionally, DFT based materials models assume an atomic system in terms the so-called "wave function", accounting for the wave-particle duality of matter and energy. The temporal and spatial evolutions of such systems are allowed with an objective to seek the equilibrium condition as represented by the minimum energy. The physical observables (e.g. energy, entropy) are computed by conducting mathematical operations on the wave functions. A wave function maps the quantum states of the bonding electrons in the form of a complex number. For the sake of computational efficiency, a wave function is further simplified into a time-independent electron density parameter (hence the designation - density functional theory). The electron charge densities are solved numerically on an iterative basis. The atoms are construed as glued together by de-localized charge cloud. Iteratively, the total energy is minimized to reach a converged level within an acceptance criterion. Consequently, one can create different crystal structures and examine their most stable configurations with remarkable accuracy [105]. The relevancy of DFT in the context of SMA slip study is particularly important, in that the discrete lattice scale responses of constituent transition type chemical species (e.g. Ni, Ti, Hf, Ga, Fe, Nb, Ta) are dictated by quantum forces [52,112].

4. Slip in NiTi

4.1. Experimental observations

Since their discovery in 1960s [113], NiTi has remained a widely used and researched SMA [71,101,114–120]. As discussed in Section 3, microscopic slip activities can occur during martensite formation in polycrystalline NiTi, which causes the observed instability of superelastic response over cycles. A possible mechanism by which transformation and microplasticity may evolve in a multi-grain environment during the cyclic superelasticity is presented in Fig. 6 (adapted from [29]). To simplify, only two grains (labeled "A" and "B") are considered, which are initially in austenitic phase. Due to mutual constraint as well as different crystal orientation with respect to the global applied (tensile) stress, their deformation ten-

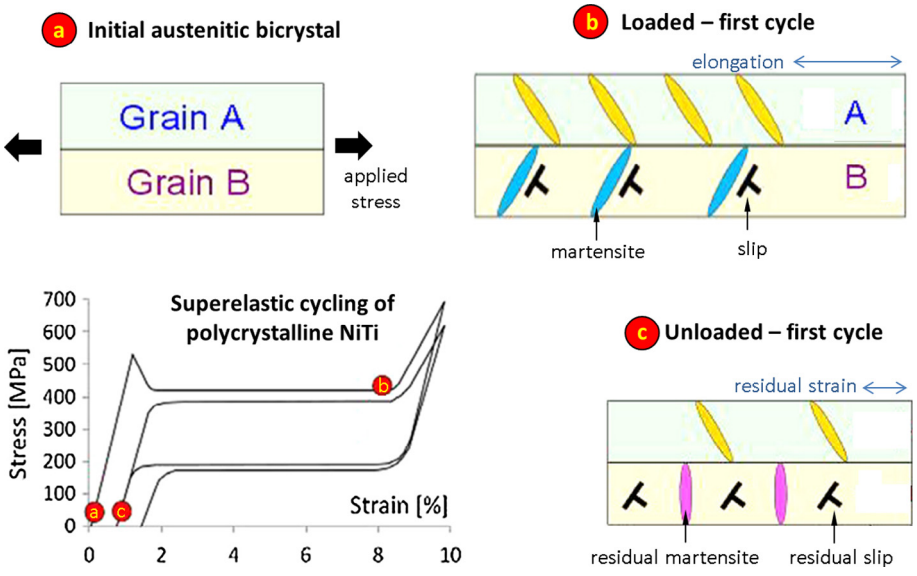

Fig. 6. A schematic illustration of how concurrent transformation and slip can occur in the polycrystalline microstructure of NiTi [29].

dency would be distinct. Upon loading, both grains start forming martensite plates while the grain B also undergoes slipping. The slip occurs at the interface between martensite and austenite to facilitate strain compatibility. On unloading, grain B retains martensite due to the irreversible nature of slip. Since the grain A is constrained by grain B, some residual martensite is retained within the grain A as a result of unloading. In other words, slipping of one grain is essentially responsible for the residual martensite in both grains. Consequently, the incremental accumulation of martensite would continue as a direct outcome of localized slip for subsequent cycles. The effect of such microscopic phenomena is reflected on the macroscale stress-strain curves in the form of functional fatigue (i.e. unstable hysteresis of superelastic loop) and subsequent loss of strain recoverability.

Thanks to rigorous electron microscopy studies, the exact nature of the dislocation slip structures as well as the predominant slip systems have been identified. Fig. 7 provides several examples of TEM evidence of dislocation in the austenitic phase of NiTi SMA based on Refs. [9,11,23,32,101,114]. Similarly, martensitic slip in NiTi was reported by some studies [115,116] as shown. The exact origin of the observed slip is challenging to ascertain on a quantitative basis from experiments. As discussed earlier, the formation of twin boundaries as well as austenite-martensite interfaces require strain compatibility satisfied. The slip within the martensite could be triggered due to prevalence of complex network of interfaces (i.e. sources of internal stresses) in the self-accommodated structure [65,115,116]. In the following sections, we discourse upon the theoretical works from Ezaz et al. and Hatcher et al. [106,107]. From their analyses, the relative resistances of the investigated slip systems are elucidated at the atomistic scale.

4.2. $(0\,1\,1)[1\,\bar{1}\,1]$ slip system in NiTi austenite

NiTi austenite has a cubic B2 type lattice [121]. Fig. 8 demonstrates the stacking of atomic layers on the $(0\,1\,1)$ plane in B2 lattice. The associated GSFE profile for this slip system is also shown in the same figure (which is constructed from the published data from [106]). A projected perspective of atomic arrangement as viewed from the $[\bar{2}\,\bar{1}\,1]$ direction is provided to facilitate understanding of the displaced crystal during the calculation of the energy pathways. The relative sizes of the atoms in the projected view indicate that they are from different $(\bar{2}\,\bar{1}\,1)$ planes. As can be seen, the stacking sequence is ABABAB. . .i.e. the atoms are repeated along $(0\,1\,1)$ direction every two planes. It should be mentioned here that establishing the atomic positions in the lattice is not trivial [35]. As we will demonstrate with examples, the apparent difference in the very atomic arrangements for different slip systems give rise to various fault energy landscapes (i.e. energy barriers to activate slip).

As for the GSFE curve (Fig. 8), when the upper half of the crystal is sheared by $\sqrt{3}a/3$ (i.e. when $u/a[1\,\bar{1}\,1] = 0.33$), the γ value reaches a peak at 660 mJ m^{-2}. At this stage, the atomic configuration is such that the near neighbor distance between two similar atoms (i.e. Ni or Ti) is shortest. Furthermore, when sheared by $u/a[1\,\bar{1}\,1] = 0.5$, a saddle point is reached at a γ magnitude of 515 mJ m^{-2}. This local minimum corresponds to the atomic structure where the near neighboring distance between two dissimilar atoms becomes shortest. The symmetric shape of $(0\,1\,1)[1\,\bar{1}\,1]$ GSFE (with a saddle point in the mid-

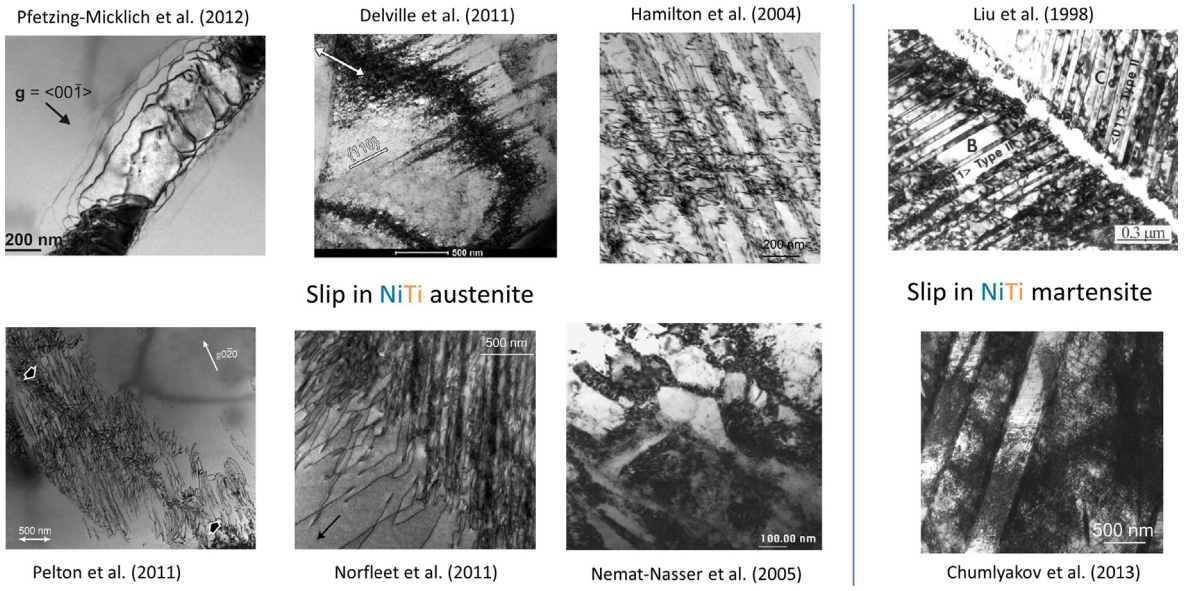

Fig. 7. (Left) TEM evidence of dislocation slip in austenite NiTi as evidenced by many research groups [9,11,23,32,101,114]. NiTi is one of the most researched SMAs as well as most widely used in commercial applications. (Right) TEM observation of slip in martensitic microstructure NiTi SMA [115,116]. The prevalence of interfacial defects (i.e. grain/twin boundaries, austenite-martensite interface) facilitates slipping of martensite.

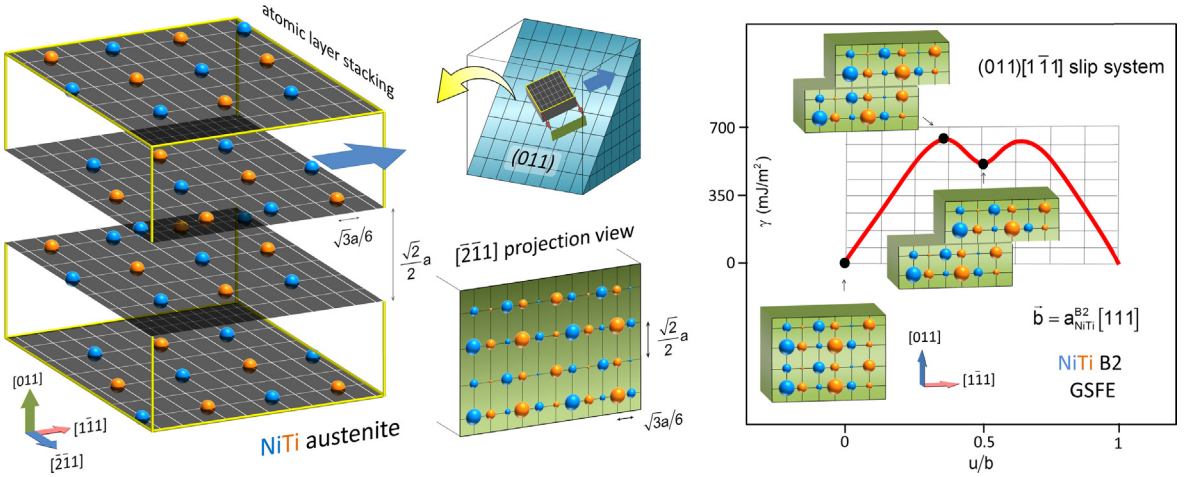

Fig. 8. (Left) schematic of the $(0\,1\,1)[1\,\bar{1}\,1]$ slip system and the associated atomic stacking on the $(0\,1\,1)$ plane in NiTi austenite. The $[\bar{2}\,\bar{1}\,1]$ projected view is shown to indicate in- and out-of-plane atoms. Atoms of the same size (either Ni or Ti) are on the same $[\bar{2}\,\bar{1}\,1]$ plane. (Right) the corresponding GSFE profile (adapted from [106]) with insets showing the atomic positions during shearing. The existence of an energy saddle point indicates a strong likelihood of planar fault formation in conjunction with slip.

dle) is essentially similar to that of an extended dislocation in an fcc lattice [122,123]. It is argued for such kind of GSFE shape that a full slip may undergo dissociation thereby creating two partials connected by a ribbon of planar fault. It can be conjectured that the $(0\,1\,1)[1\,\bar{1}\,1]$ slip might be facilitated by a propensity to generate a similar planar fault as permitted in the ordered B2 lattice of NiTi austenite. In most likelihood, two dislocations would be accompanied by a plane of antiphase boundary (APB) as has been observed in many other ordered lattices.

4.3. $(0\,1\,1)[0\,\bar{1}\,1]$ slip system in NiTi austenite

The atomic stacking for the $(0\,1\,1)$ plane is shown in Fig. 9. The Ni and Ti atoms are positioned in an ABAB. . . type stacking. It follows that the GSFE for $(0\,1\,1)[0\,\bar{1}\,1]$ slip system is symmetric about the midpoint [106]. The maximum energy to be overcome to create slip on the $(0\,1\,1)[0\,\bar{1}\,1]$ system is about 1545 mJ m^{-2}. It implies that this system would require a significantly large magnitude of applied stress to be active during the plastic deformation. The reason for encountering such a high barrier is the atomic arrangements of the sheared crystal. As seen in the inset figure, at the energy peak, atoms of the same element (i.e. either Ni or Ti) are positioned on top of each other. This is a highly unstable structure requiring an enhanced magnitude of shearing forces.

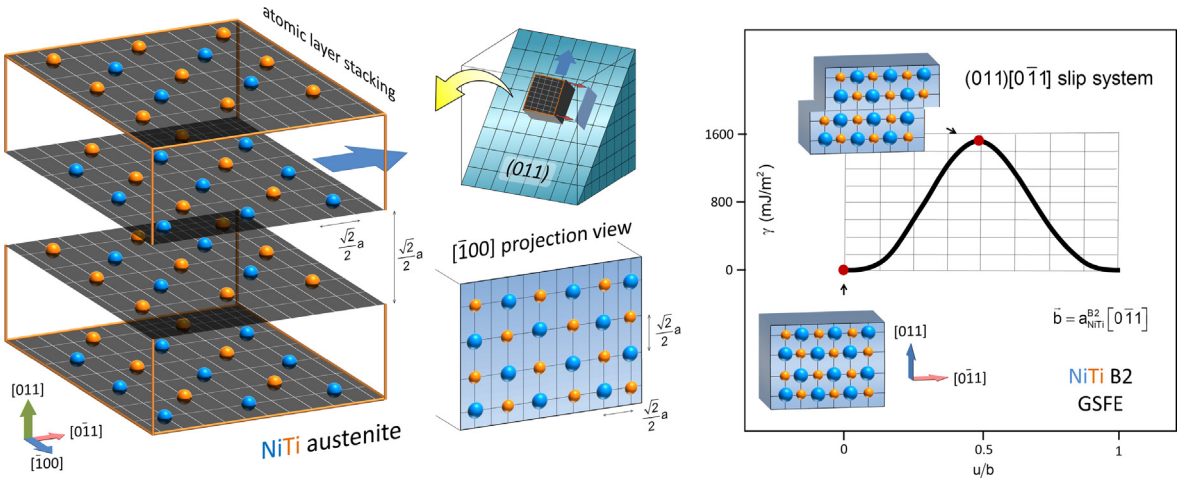

Fig. 9. (Left) atomic stacking on the $(0\,1\,1)$ plane in NiTi austenite for the GSFE calculation of $(0\,1\,1)[0\,\bar{1}\,1]$ system (re-plotted from published data [106]). The projection of atoms from different $(\bar{1}\,0\,0)$ planes is also shown (as lower middle inset).

4.4. $(0\,1\,1)[1\,0\,0]$ slip system in NiTi austenite

This slip system is predicted to be most favorable on an energetic ground [106]. Fig. 10 shows the distribution of atoms on the $(0\,1\,1)$ plane in a pristine lattice configuration. This layer-by-layer arrangement of atoms is found most densely packed. The GSFE curve for this slip system is asymmetric about the middle peak. The associated energy barrier is also considerably low (142 mJ m^{-2}). The asymmetric nature of the energy curve has been attributed to the difference in the bonding lengths among atoms after the two crystal halves are displaced by 50% of the Burgers vector. At this stage, a reduction in the average interatomic distance among the nearest neighbors is noted, which is believed to have lowered the shear resistance. Further elucidation can be obtained by examining the entire γ surface on the $(0\,1\,1)$ plane as computed by Hatcher et al. [107] as in Fig. 11. It follows that the $\langle 1\,0\,0\rangle$ direction offers the energetically most favorable pathway in order for the pristine crystal to be sheared. This is important observation simulation-wise since the $(0\,1\,1)[1\,0\,0]$ slip system is the one observed predominantly in experimental microscopy studies [106]. Hatcher et al. also performs a detailed sensitivity test on the role of atomic relaxation and number of layers used in computation. While notable variations are noted in terms of energy magnitudes, the fundamental conclusion regarding the minimum energy pathway for slip occurring along the $[1\,0\,0]$ remains unchanged despite these simulation-related artifacts.

4.5. $(0\,0\,1)\langle 0\,1\,0\rangle$ slip system in NiTi austenite

Fig. 12 illustrates the stacking of atoms on $(0\,0\,1)$ planes where each consecutive plane either contains Ni or Ti atoms. This special atomic arrangement gives rise to the calculated GSFE along the $[0\,1\,0]$ direction. The energy barrier to create slip for this system is found to be 863 mJ m^{-2} [106]. It follows that the GSFE plot is symmetric about the mid-point, which can be attributed to the symmetry of the atomic stacking. By examining the γ surface in this entirety on the $\{0\,0\,1\}$ plane, Hatcher et al. [107] arrived at a similar conclusion where the $[0\,1\,0]$ direction is found to offer least resistance to the shear displacement of two crystal half-spaces on the $(0\,0\,1)$ plane (Fig. 13).

4.6. $(\bar{2}\,1\,1)[1\,1\,1]$ slip system in NiTi austenite

Another possible slip system investigated by Ezaz et al. [106] was the $(\bar{2}\,1\,1)[1\,1\,1]$ (Fig. 14). It is observed that at a displacement of $u/a[1\,1\,1] = 0.5$, there exists a metastable crystal configuration. Also noteworthy is the fact that the energy barriers for slipping along $[1\,1\,1]$ versus $[\bar{1}\,\bar{1}\,\bar{1}]$ are not the same. This is an interesting finding, in that a slight directionality for slipping for this system is reported for the first time. The peak energy for the $[1\,1\,1]$ case is found to be 847 mJ m^{-2} at $u/a[1\,1\,1] = 0.33$ and the $[\bar{1}\,\bar{1}\,\bar{1}]$ as 795 mJ m^{-2} at $u/a[1\,1\,1] = 0.67$.

4.7. Significance of slip energetics in NiTi

The relative energetics of the studied systems reported above is compared in terms of the energy barrier (i.e. the unstable stacking fault energy, γ_{us}) in Fig. 15 (after [55,106]). The solid blocks of different colors imply the shearing of the lattice during slipping. The arrows indicate the slip direction on a certain plane. The arrows are colored in accordance with the mag-

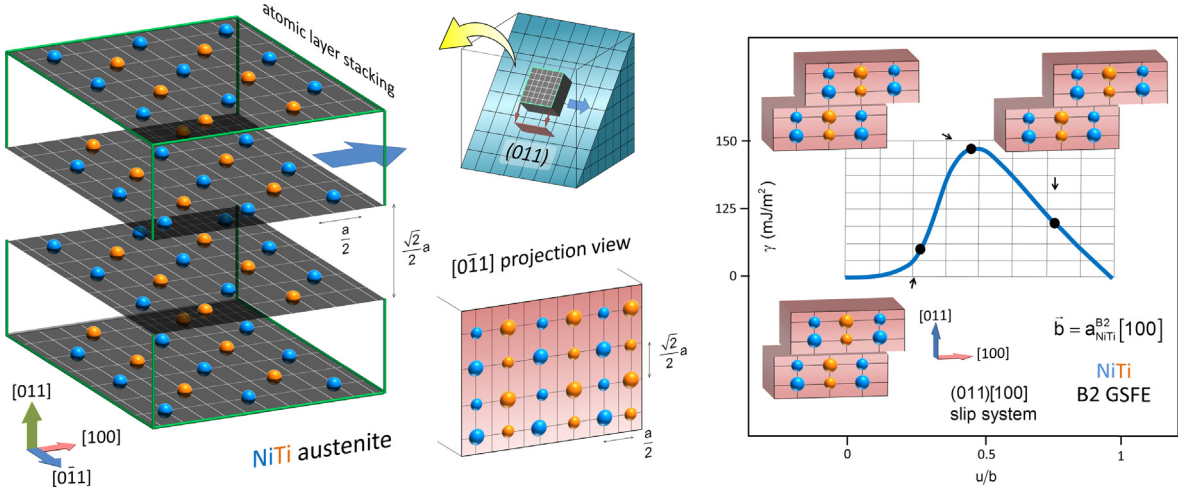

Fig. 10. Stacking of atoms and the GSFE profile for the $(0\,1\,1)\langle 1\,0\,0\rangle$ slip system. It is found that this system has the lowest magnitude of γ_{us} [106]. Notice in the projected view along the $[0\,\bar{1}\,1]$ direction, the atoms are repeated every other plane thereby giving rise to a strong symmetry.

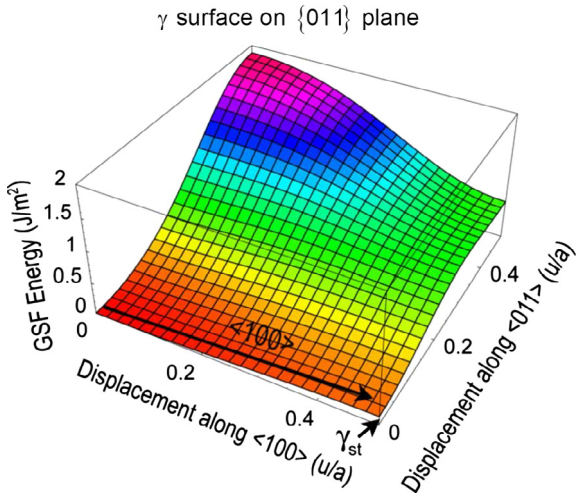

Fig. 11. The entire γ energy landscape on the {0 1 1} plane [107]. The arrow indicates crystallographic direction offering the minimum energy pathway for shearing.

nitude of the γ_{us}, which is shown in the color bar. It follows that the relative strength of these five slip systems can be energetically presented with the following order: $\gamma_{us}^{(0\,1\,1)[0\,1\,1]} > \gamma_{us}^{(0\,0\,1)[0\,1\,0]} > \gamma_{us}^{(\bar{2}\,1\,1)[\bar{1}\,0\,1]} > \gamma_{us}^{(0\,1\,1)[1\,\bar{1}\,1]} > \gamma_{us}^{(0\,1\,1)[0\,0\,1]}$. This is consistent with the predominance of the $(0\,1\,1)[1\,\bar{1}\,1]$ and $(0\,1\,1)[1\,0\,0]$ slip systems in electron microscopy studies [106].

The interesting aspect of the foregoing energy-based analysis is that a physical rationale as to why a certain slip system possesses enhanced propensity has emerged. For instance, the $(0\,1\,1)[1\,0\,0]$ slip system is the most observed one during the plastic deformation of NiTi austenite experimentally. Simulation-wise, this system has been associated with the lowest energy barrier of all the systems [106,107]. Similarly, the $(0\,1\,1)[1\,\bar{1}\,1]$ slip system (with the second lowest energy barrier) is also commonly observed [106]. From the atomistic analysis, the physical rationale for such a preference can be related with the close packing of nearest neighbor atoms around the dislocation line. The most favorable slip system has been found to be the one which achieves the shortest nearest neighbor distances during the shear displacements. In other words, the most likely slip plane/direction corresponds to the crystal structure with highest degree of atomic packing [55]. Moreover, further information regarding the nature of slip can be gleaned from the shapes of the computed GSFEs, particularly, the nucleation tendency of planar faults (e.g. antiphase boundary). For example, there exists an energetic well for the case of $(0\,1\,1)[1\,\bar{1}\,1]$ GSFE, which indicates a strong propensity towards forming anti-phase boundaries via slip dissociation reactions as follows.

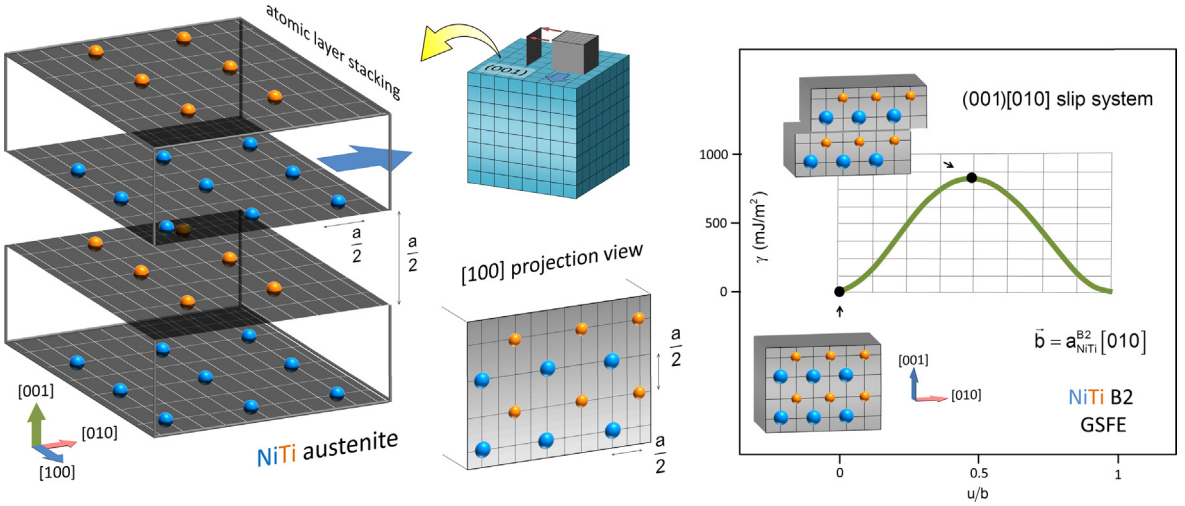

Fig. 12. (Left) atomic stacking on the (001) plane in NiTi austenite, each of which contains only one type of elements (either Ni or Ti). However, atoms on adjacent planes are placed with an offset displacement as can be seen in the projected view along the [100] direction. (Right) the predicted GSFE profile for the $(0\,0\,1)[0\,1\,0]$ slip system [106].

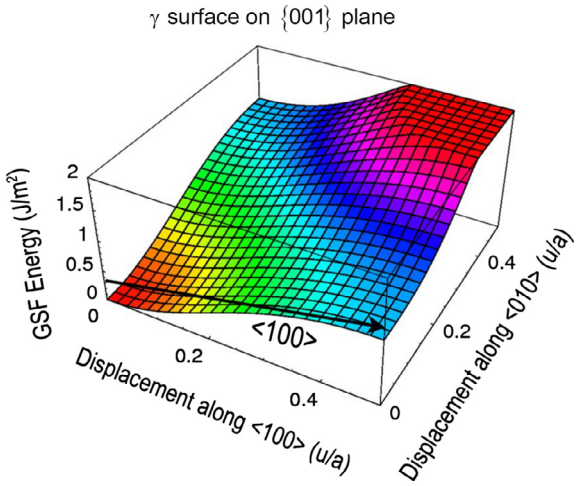

Fig. 13. The full γ energy landscape on the {0 0 1} plane [107]. The arrow is used to demonstrate the crystallographic path with least energy barrier against shear.

$$a[1\bar{1}1] = \frac{a}{2}[1\bar{1}1] + \frac{a}{2}[1\bar{1}1] \tag{1}$$

Such dissociation reaction is observed in other similar crystals (i.e. cubic B2 type) such as FeAl and CuZn [124]. In this case, the dissociated partial dislocations would assume stable positions as separated by a plane of APB. On similar reasoning, the $(\bar{2}11)[111]$ slip is also likely to undergo dissociation reaction such as the following one [106].

$$a[1\bar{1}1] = a[100] + a[0\bar{1}1] \tag{2}$$

5. Slip in Ni_2FeGa austenite (experiment and theory)

The Ni_2FeGa is a relatively new ternary shape memory alloy. This material reportedly possesses large recoverable strain, small hysteresis and low transformation stress [125] i.e. with an excellent blend of desired properties. Given its potential, understanding the slip energy pathways can prove crucial in plastic damage assessment. As in Fig. 16, the plasticity-induced deterioration can be noticed both in the isobaric strain-temperature curve and the superelastic loops [126,127]. With increasing temperature, the plastic strain was observed to be accumulating. Similarly, increasing applied stress level has resulted in the non-closure of the isobaric shape memory loops. In one study by Hamilton et al. [128], a substantial presence of dislocation slip has been reported as can be seen in Fig. 16. Analysis on which slip systems are more vulnerable has

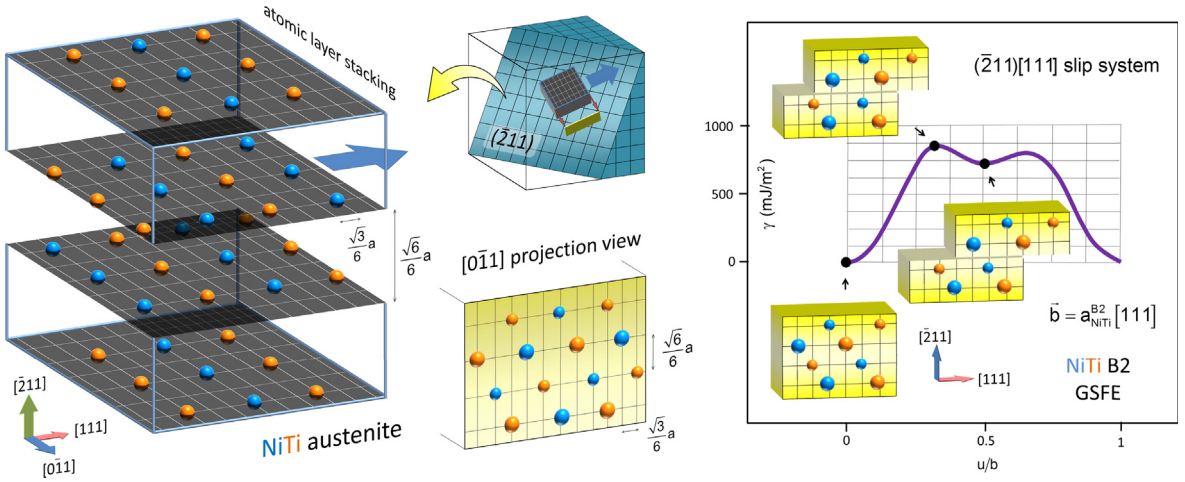

Fig. 14. Atomic stacking on the $(\bar{2}11)$ plane in NiTi austenite in three-dimensional view and the GSFE curve predicted from the DFT calculations [106]. The existence of a local energy minimum indicates a slight propensity for slip dissociation.

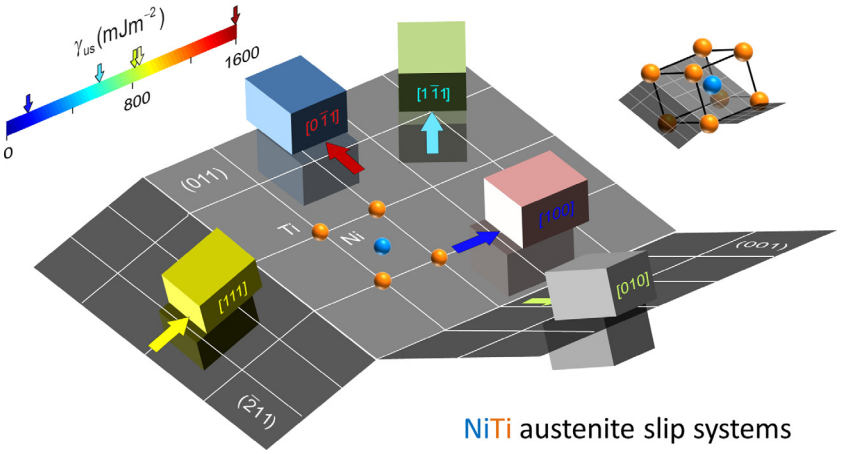

Fig. 15. A schematic summary of energetic analysis of all slip systems in NiTi austenite based on data from Ref. [106]. The colored arrows point towards the respective Burgers vector direction and they are colored according to the γ_{us} magnitude as indicated in the colorbar. The order of energy barriers for these systems is: $\gamma_{us}^{(0\,1\,1)[0\,\bar{1}\,1]} > \gamma_{us}^{(0\,0\,1)[0\,1\,0]} > \gamma_{us}^{(\bar{2}\,1\,1)[\bar{1}\,0\,1]} > \gamma_{us}^{(0\,1\,1)[1\,\bar{1}\,1]} > \gamma_{us}^{(0\,1\,1)[0\,0\,1]}$ [55].

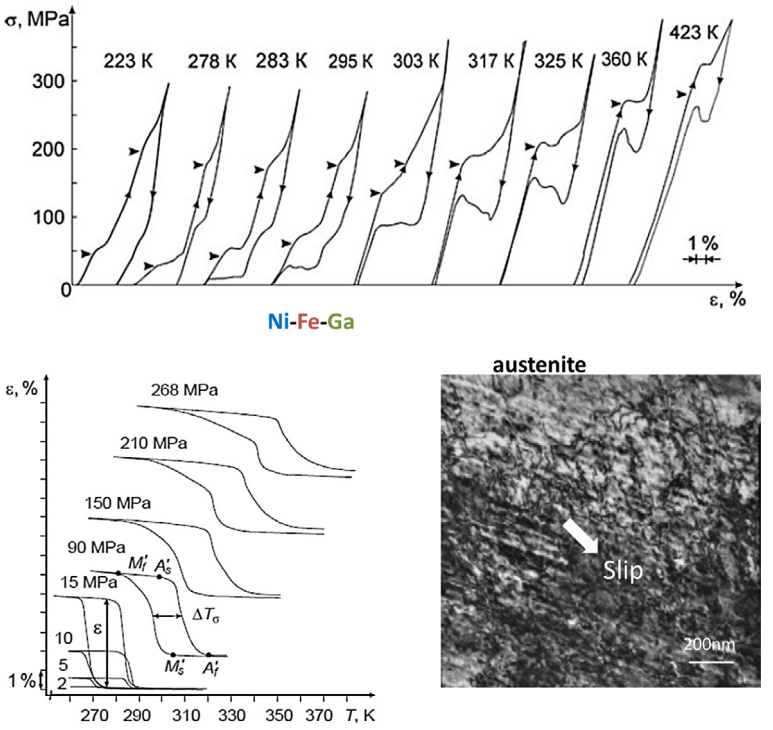

Fig. 16. (Top) experimental observation of plasticity induced deterioration of superelastic responses in Ni-Fe-Ga SMA with increasing temperature [126]; (bottom left) non-closure of isobaric strain-temperature cycles due to accumulation of plastic strain at gradually higher stresses [127]; (bottom right) TEM evidence of substantial dislocation activities in the austenitic phase of Ni-Fe-Ga SMA [128].

been conducted by Sehitoglu and co-workers [57,59] as is elaborated in the following sections. From the experimental studies [125], the slip systems in the Ni_2FeGa austenite are likely to be: $(0\,1\,1)\langle 1\,1\,1\rangle$ and $(0\,1\,1)\langle 0\,0\,1\rangle$ as in Fig. 17. The crystal lattice of Ni_2FeGa austenite is of $L1_2$ type as shown. It is worth mentioning here that the phase transformation process in Ni_2FeGa SMAs are rather complex involving multiple intermediate steps [79,129–131] such as $L2_1$ (austenite) → 10M → 14M → $L1_o$ (martensite). It suffices to consider the first and last steps i.e. the $L2_1$ and $L1_o$ lattices to understand the slip propensity of Ni_2FeGa. The energy barriers for the two slip and the geometry considered for the rigid shear based calculations are provided in Fig. 18.

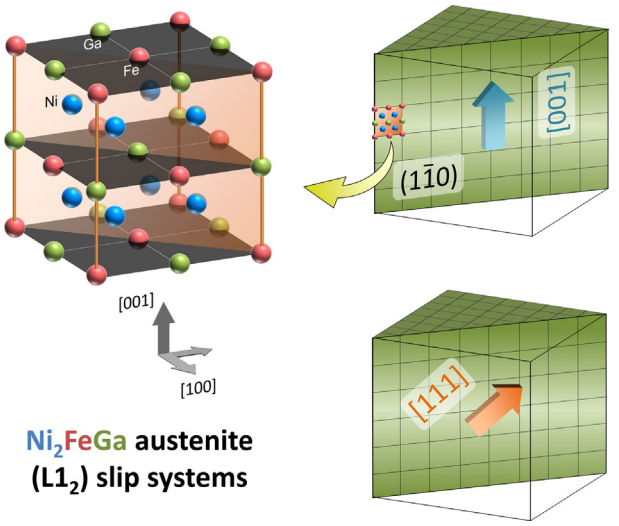

Fig. 17. Schematic illustration of $L1_2$ primitive cell in Ni_2FeGa austenite and the slip systems, which are: $(0\,1\,1)\langle 1\,1\,1\rangle$ and $(0\,1\,1)\langle 0\,0\,1\rangle$.

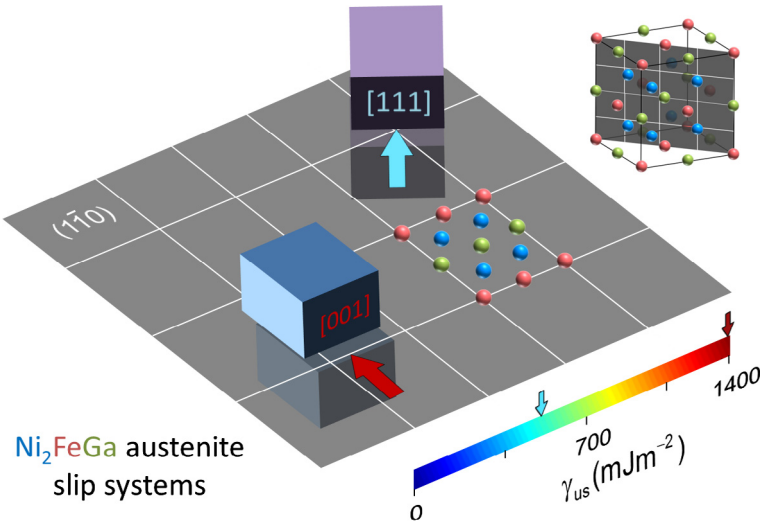

Fig. 18. By comparing the energy barrier for slip nucleation i.e. the unstable stacking fault energy (γ_{us}), the more likely slip systems to be activated in $L1_2$ Ni_2FeGa austenite is predicted to be the $(0\,1\,1)\langle 1\,1\,1\rangle$ [57].

5.1. $(0\,1\,1)[1\,1\,1]$ slip system in Ni_2FeGa austenite ($L2_1$)

The $(0\,1\,1)$ slip plane with the atoms positioned for a $L2_1$ lattice is illustrated in Fig. 19. The stacking sequence in the $[1\,1\,1]$ direction is found similar to that of bcc lattice of a single chemical species [79]. In the view projected along the $(1\,1\,\bar{2})$ direction, one can note that a total of six parallel layers on the $(1\,1\,\bar{2})$ planes are present.

The shape of the DFT-computed GSFE has multiple peaks and valleys [57]. Upon overcoming the first energy peak, the first saddle point is reached at a displacement of u = b where $\vec{b} = 1/4a^{austenite}_{Ni_2FeGa}[1\,1\,1]$. The crystal structure at this juncture gives rise to an antiphase boundary (APB). Particularly noteworthy is the ordering of atoms along the vertical direction i.e. $[1\,\bar{1}\,0]$ in the inset figure. In the original (un-displaced) crystal, atoms of a specific species (Ni, Fe or Ga) were aligned vertically (as discerned from the projection). Now, there exists an alternate pair of atoms belonging to the same element (Ni, Fe or Ga). While the very first saddle point is associated with an alteration of nearest neighbors (NN), the second one corresponds to the next nearest neighbors (NNN) being rearranged. The predicted GSFE profile essentially indicates that slip for this system would consist of four superpartial dislocations connected by two NN- and one NNN-APBs as depicted in Fig. 20 and presented in Eq. (3).

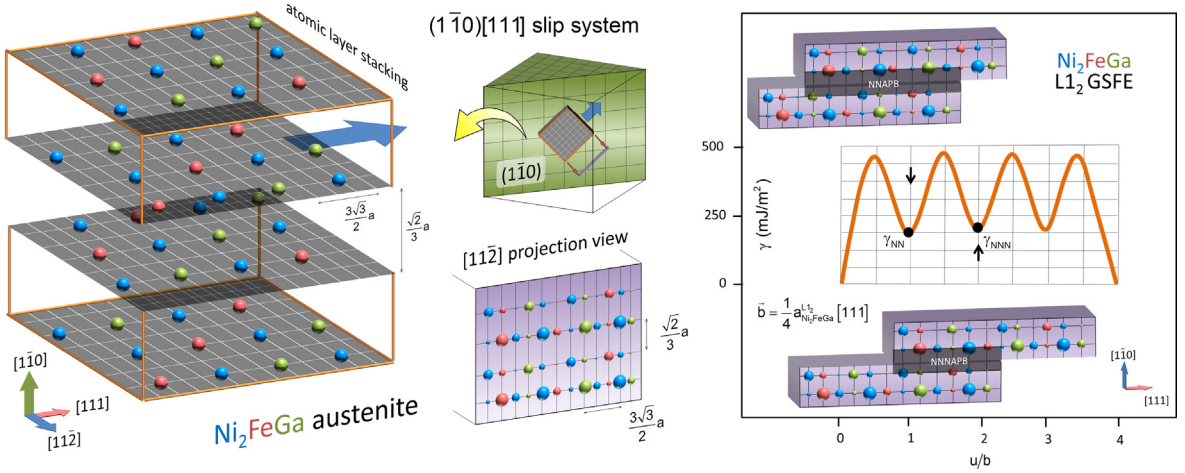

Fig. 19. (Left) atomic stacking on the $(1\bar{1}0)$ plane in Ni_2FeGa austenite and the projected view of the stacking along the $[11\bar{2}]$ direction. (Right) the GSFE curve for the same slip system (adapted from [57]). Notice the existence of multiple local energy minima unlike the binary NiTi case with single minimum in some cases. Also, the first energy saddle point corresponds to a near neighbor anti-phase boundary (NNAPB). Continued shearing along the same direction results in the formation of next nearest neighbor APB (NNNAPB) at the interface.

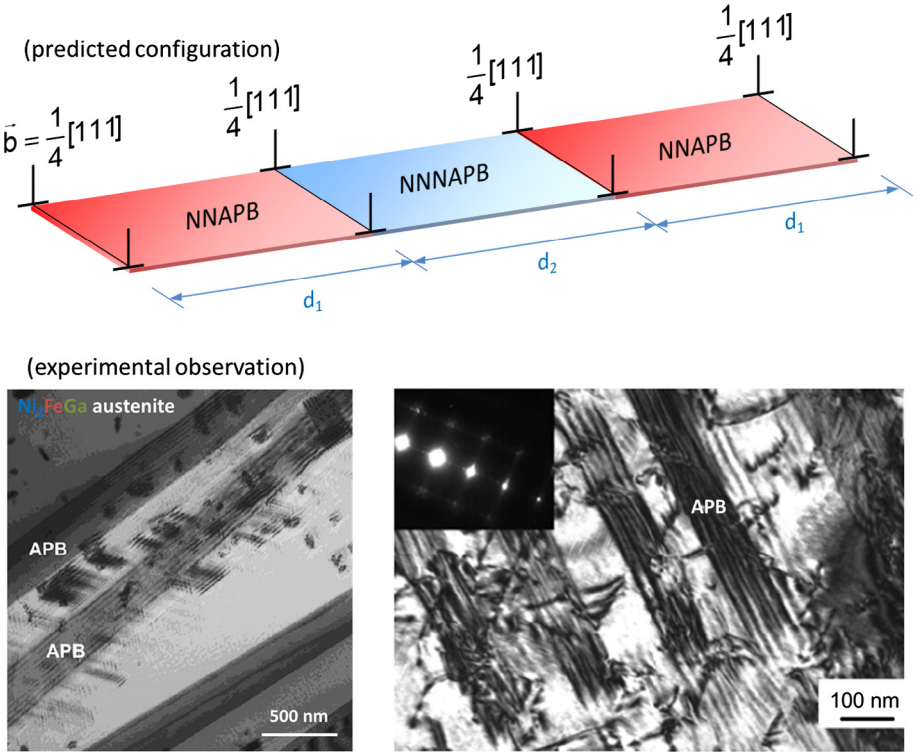

Fig. 20. (Top) Predicted dissociation of a full dislocation into four partial dislocation of $\frac{1}{4}\langle 1\,1\,1\rangle$ type connected by NNAPB and NNNAPB. (Bottom) TEM observation of APBs during the plastic deformation in the single crystal of Ni_2FeGa austenite [57,125].

$$\underset{\text{superdislocation}}{[111]} = \underset{\text{superpartial}}{\frac{1}{4}[111]} + \text{NNAPB} + \underset{\text{superpartial}}{\frac{1}{4}[111]} + \text{NNNAPB} + \underset{\text{superpartial}}{\frac{1}{4}[111]} + \text{NNAPB} + \underset{\text{superpartial}}{\frac{1}{4}[111]} \qquad (3)$$

Experimental validation of the APB formation during plastic deformation is reported by several research groups. For instance, Sehitoglu et al. and Chumlyakov et al. [57,125] conducted TEM analyses on the austenitic crystal and a substantial presence of APBs was noticed as in Fig. 20.

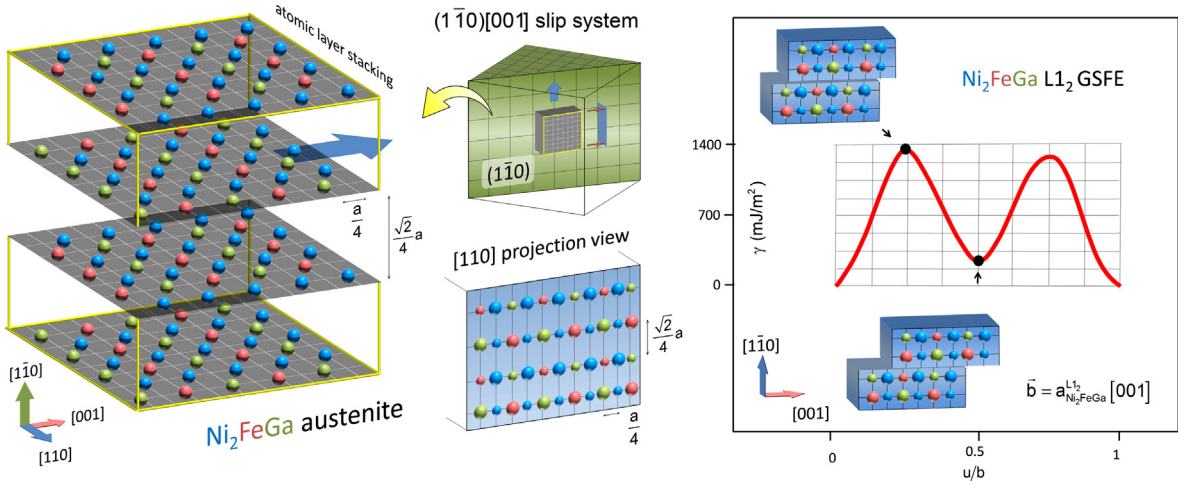

Fig. 21. (Left) stacking sequence of atoms on (1 $\bar{1}$ 0) plane in the Ni_2FeGa austenite and the projected view is along the [110] direction showing the same stacking in two-dimensional view (left). (Right) GSFE profile for the slip system (0 1 1)⟨0 0 1⟩ in Ni_2FeGa austenite with $L1_2$ lattice [57]; unlike the GSFE with multiple peaks for (0 1 1)⟨1 1 1⟩ slip system, there exists only one saddle point indicating the creation of one type of planar type fault only. Also, noticeable is the higher peak energy for this case.

5.2. (0 1 1)[0 0 1] slip system in Ni_2FeGa austenite ($L2_1$)

In Fig. 21, the atomic arrangement on four consecutive (0 1 1) planes, to be sheared along [0 0 1] direction is presented. Two energy peaks are noted with a local minimum in-between. The first peak energy has the magnitude of about 1400 mJ m^{-2}, which is considerably larger than the previous slip system discussed (470 mJ m^{-2}) [57]. The second peak energy is slightly lower than the first one. The energy magnitudes as well as the particular shape of the (0 1 1)[0 0 1] GSFE mean that the slip of the [0 0 1] type would disintegrate into two partials of type 1/2[0 0 1] bound by a planar fault. However, due to a high energy barrier of 1400 mJ m^{-2}, a large applied stress level would be required to activate this slip system. Consequently, the (0 1 1)[0 0 1] system would be rather less predominant compared to the (0 1 1)[1 1 1] system. A schematic comparison is presented for the peak energies (i.e. γ_{us}) for both cases in Fig. 18.

6. Slip dissociation and energy surface in Ni_2FeGa martensite ($L1_o$)

Four slip systems in the Ni_2FeGa martensite are all on the (1 1 1) plane, which contains the most densely packed arrangement of atoms. The Burgers vector directions of interest are: [$\bar{1}$ 0 1], [$\bar{2}$ 1 1], [1 1 $\bar{2}$] and [$\bar{1}$ 1 0]. The primitive unit cell in Ni_2FeGa

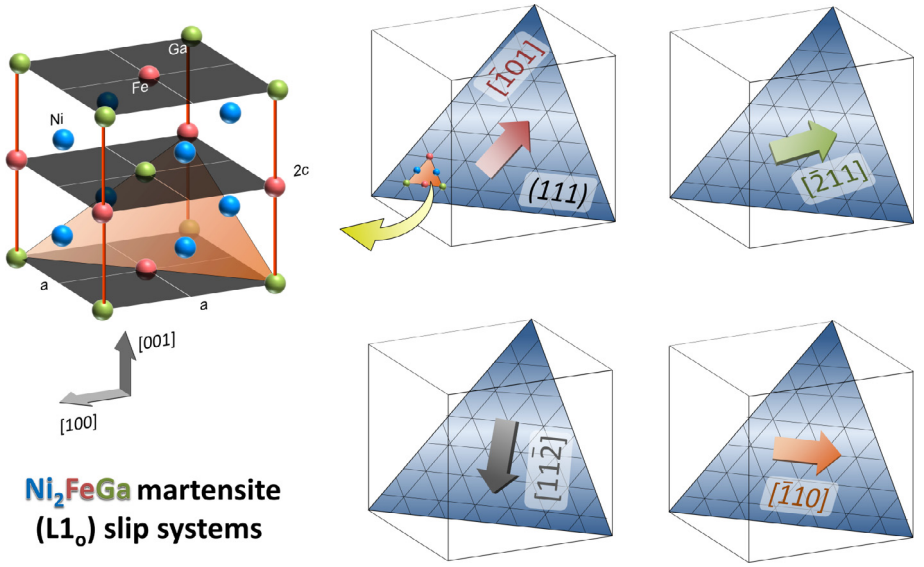

Fig. 22. The martensite crystal structure in Ni_2FeGa SMA is of $L1_o$ type. The likely slip systems for this lattice type are: (1 1 1)[$\bar{1}$ 0 1], (1 1 1)[$\bar{2}$ 1 1], (1 1 1)[1 1 $\bar{2}$] and (1 1 1)[$\bar{1}$ 1 0].

martensite is of $L1_o$ type lattice. The unit cell and the slip systems are schematically presented in Fig. 22. Fig. 23 shows the entire γ surface on $(1\,1\,1)$ plane with all energy peaks and valleys (reconstructed based on data from [59]). Important insight can be obtained from this γ surface. For example, if a superdislocation of Burgers vector $\frac{1}{2}[1\,1\,\bar{2}]$ is to be created, the relevant energy profile would be along the $[1\,1\,\bar{2}]$ edge. In essence, a consistent shearing along $[1\,1\,\bar{2}]$ direction means dissociation of $\frac{1}{2}[1\,1\,\bar{2}]$ slip into three $\frac{1}{6}[1\,1\,\bar{2}]$ partials. After a displacement $u = \frac{1}{2}[1\,1\,\bar{2}]$, a metastable structure is created corresponding to a local energy minimum whose magnitude is 85 mJ m^{-2}. This represents the creation of first partial. However, further shearing along the same direction poses a very high energy to overcome, for example, a peak magnitude of 475 mJ m^{-2} at $u = \frac{1}{3}[1\,1\,\bar{2}]$. Now, instead of overcoming this barrier, the material tends to slip with more ease along another family of $\langle 1\,1\,2\rangle$ direction.

In Fig. 24, the three layers of $(1\,1\,1)$ planes in Ni_2FeGa martensite $L1_o$ lattice are shown with their atomic stacking (adapted from [59]). The relative positioning of atoms on each plane is identical; however, their ordering on the vertical direction differs. It is known that a superdislocation lying on the $(1\,1\,1)$ plane in a $L1_o$ lattice can undergo dissociation creating partials with smaller Burgers vectors [132–134]. The superdislocations in the present case are $[\bar{1}\,1\,0]$, $\frac{1}{2}[1\,1\,\bar{2}]$ and $[\bar{1}\,0\,1]$ which are likely to undergo dissociating into partials of $\frac{1}{6}\langle 1\,1\,2\rangle$ type connected by various planar faults as given by the following reactions.

$$\underset{\text{superdislocation}}{[\bar{1}10]} = \underset{\text{partial}}{\frac{1}{6}[\bar{2}11]} + \text{CSF} + \underset{\text{partial}}{\frac{1}{6}[\bar{1}2\bar{1}]} + \text{APB} + \underset{\text{partial}}{\frac{1}{6}[\bar{2}11]} + \text{CSF} + \underset{\text{partial}}{\frac{1}{6}[\bar{1}2\bar{1}]} \tag{4}$$

$$\underset{\text{superdislocation}}{[\bar{1}01]} = \underset{\text{partial}}{\frac{1}{6}[\bar{1}\bar{1}2]} + \text{SISF} + \underset{\text{partial}}{\frac{1}{6}[\bar{2}11]} + \text{APB} + \underset{\text{partial}}{\frac{1}{6}[\bar{1}\bar{1}2]} + \text{CSF} + \underset{\text{partial}}{\frac{1}{6}[\bar{2}11]} \tag{5}$$

$$\underset{\text{superdislocation}}{\frac{1}{2}[11\bar{2}]} = \underset{\text{partial}}{\frac{1}{6}[11\bar{2}]} + \text{SISF} + \underset{\text{partial}}{\frac{1}{6}[\bar{1}2\bar{1}]} + \text{APB} + \underset{\text{partial}}{\frac{1}{6}[11\bar{2}]} + \text{CSF} + \underset{\text{partial}}{\frac{1}{6}[2\bar{1}\bar{1}]} \tag{6}$$

The CSF, APB and SISF respectively stand for complex stacking fault, antiphase boundary and superlattice intrinsic stacking fault in the above equations. All these dissociation reactions are also shown in their atomistic configurations in Fig. 24. It should be noted the net Burgers vector is conserved for each case.

It is apparent from the above analysis that the slip dissociation leads to the creation of stable planar faults. Thus the first step to understand these reactions would be to quantify the energy barriers (or rather the entire energy pathways) to generate various planar faults. Fig. 25 presents the calculated energy levels for these faults and the associated partial disloca-

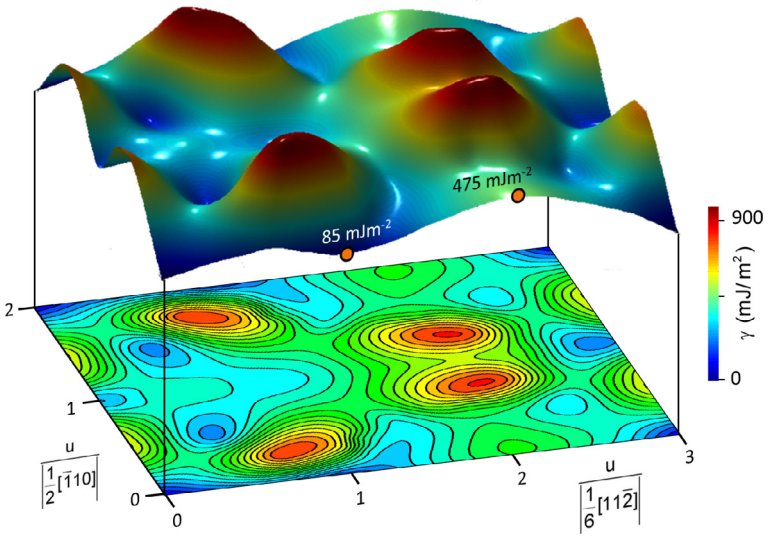

Fig. 23. The entire γ surface on the $(1\,1\,1)$ plane [59]. If sheared along a uniform direction only, say, $[1\,1\,\bar{2}]$, first a saddle point with fault energy of 85 mJ m^{-2} is encountered followed by a peak energy of 475 mJ m^{-2}. In nature, material would pick a set of directions belonging to the same family to avoid high barriers i.e. leading to a dissociation reaction.

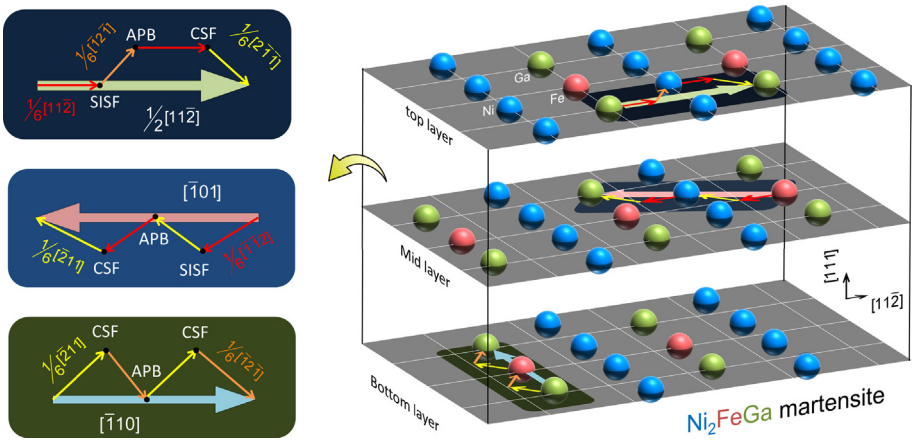

Fig. 24. (Left) Dissociation of full dislocations into a set of superpartials in the martensitic lattice ($L1_o$) of Ni_2FeGa SMA. (Right) Arrangement of atoms on consecutive layers of (1 1 1) planes in the $L1_o$ lattice in Ni_2FeGa martensite, whereupon dissociation reactions can occur as indicated with similarly colored arrows.

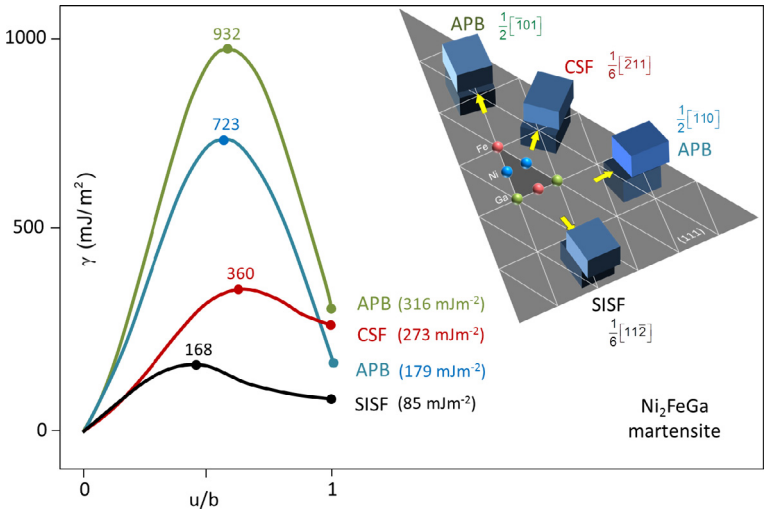

Fig. 25. The fault energy profile that the material would undergo during the creation of a certain type of planar fault such as APB, CSF or SISF. Notice that the creation of a certain type of planar fault is subjected to the specific crystallographic direction to which the material is being displaced (re-plotted using data from [59]).

tions that are nucleated in the process [59]. The crystallographic plane and directions adopted for the rigid block shear simulations (for generating respective planar faults) are presented as insets in Fig. 25.

It follows that in different crystal directions certain planar defects are preferred during shearing. This essentially underlies the propensity to a certain dissociation type since under applied mechanical forces the material would elect to deform along the energy path with lowest barrier(s). To illustrate, let us consider the case of $[\bar{1}\,1\,0]$ dissociation into a combination of four superpartials and two planar faults as in Fig. 26. The geometric arrangement of the line defects (i.e. the partial dislocations) and the planar defects (i.e. the CSF and APBs) for such case is illustrated in Fig. 27. The presence of the APB in this regard has also been observed in the electron microscopy study in the martensitic ($L1_o$) lattice of Ni_2FeGa [59].

7. Slip in high temperature SMAs (Ni-Ti-Pd and Ni-Ti-Pt)

7.1. Experimental results

Addition of a ternary element to the Ni-Ti binary composition has been utilized to improve the high temperature applicability. The most widely used ternary elements include Pd, Pt, Hf, Zr, etc. For example, with addition of Pd (>10%), the Ni-Ti-Pd demonstrates superior high temperature (>100 °C) SMA attributes [135–138]. Alloying with Pt also has similar effects; however, Pt remains an expensive choice for such benefits. Given the slated high temperature operating conditions, the

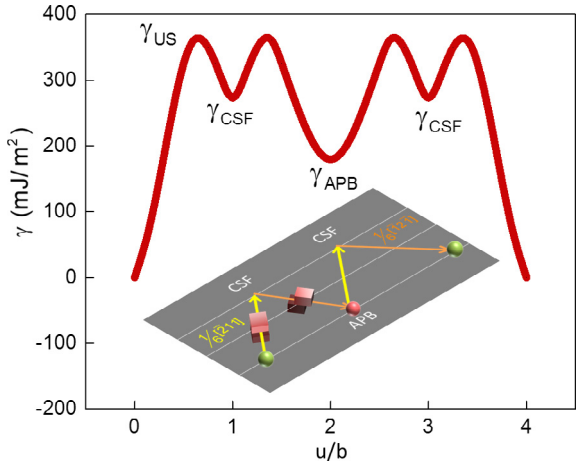

Fig. 26. The GSFE profile [59] for an example dissociation reaction. Note that the peak energy levels are now significantly lower compared to Fig. 23. From the energetic comparison, it follows that dissociated slip is more likely to occur than the full slip.

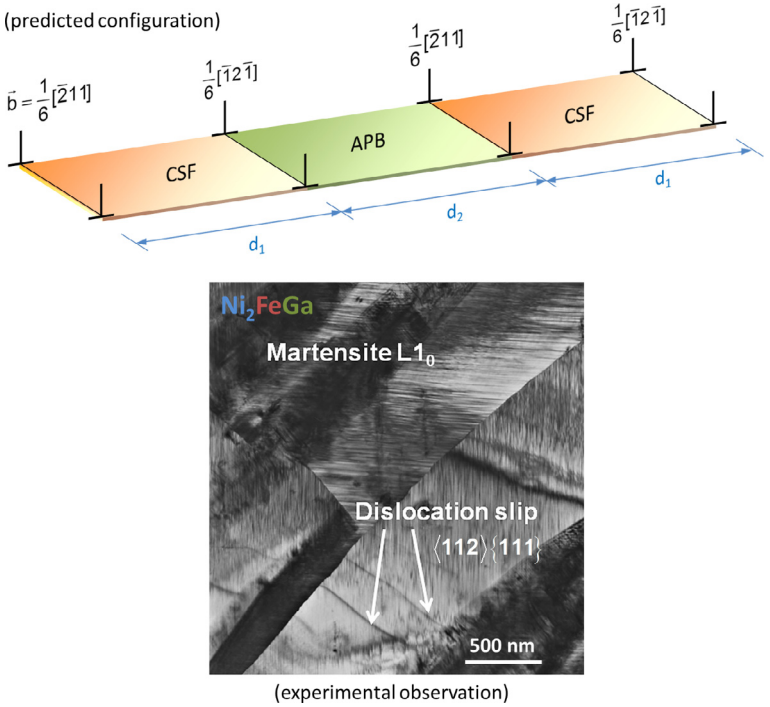

Fig. 27. (Top) Predicted slip configuration consisting of four partial dislocations of $\frac{1}{6}\langle 1\,1\,2\rangle$ type connected by complex stacking fault (CSF) and anti-phase boundary (APB) in the martensitic Ni_2FeGa [59]; (bottom) TEM evidence of $(1\,1\,1)[1\,1\,\bar{2}]$ type slip occurring in the Ni_2FeGa martensite.

enhanced tendency of slip generation due to thermal activation is a matter of design concern [139,140] for Ni-Ti-Pd and Ni-Ti-Pt SMAs. In general, increasing the slip resistance in these SMAs remains an ongoing pursuit, for which several empirical achievements are noted. For example, grain refinement, addition of a fourth element, precipitate hardening [141–144], etc. have proved as successful strategies in inhibiting slip considerably.

For example, a grain refinement up to 100 nm is achieved by subjecting Ni-Ti-Pd SMAs to equal channel angular extrusion (ECAE) method. Consequently, an increased resistance to dislocation slip was indeed achieved [145]. Fig. 28 presents both the microstructure and the constitutive response for such a case. The TEM image (in conjunction with selected area diffraction patterns) shows the austenitic phase of a Ni-Ti-Pd alloy following the ECAE process, where the nano-sized grain structures (about 100 nm of diameter) are noticed. At the upper right corner of Fig. 28 are the compressive stress-strain responses of the as-received and ECAE-hardened Ni-Ti-Pd specimens. Significant enhancing of the macroscopic yield strength is reported for the ECAE specimen (>1500 MPa). Another remarkable feature is that the transformation strengths for both cases

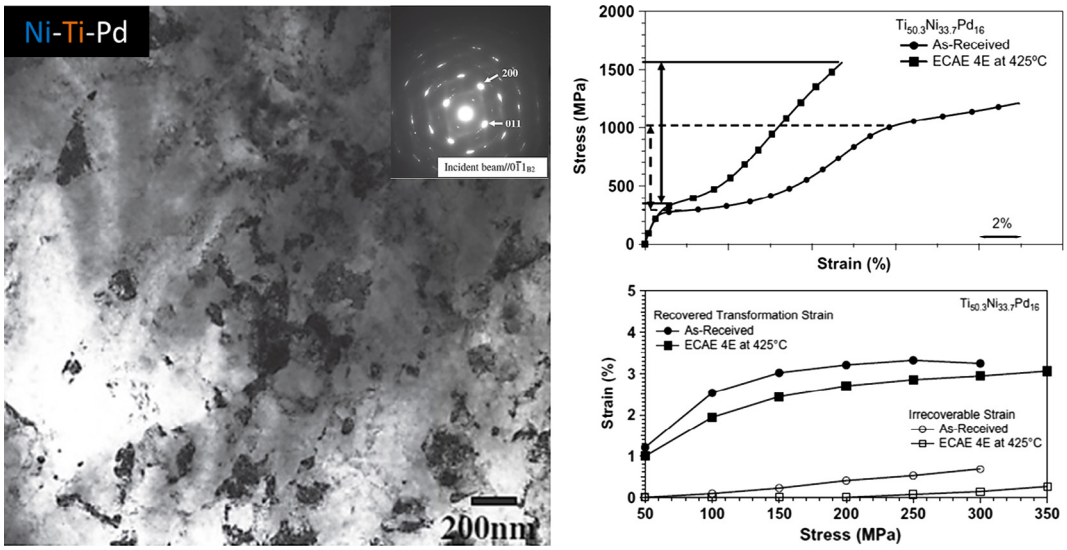

Fig. 28. (Left) austenitic NiTiPd crystal with nano-sized grains (100 nm on average) after ECAE process at 200 °C [145]. (Upper right) ECAE-processed specimens (having finer grains i.e. with higher slip resistance) demonstrating increased flow strength compared to the as-received ones (see text for more discussions). (Lower right) evolution of transformation and irreversible strain in the as-received and ECAE specimens.

remain almost unchanged. The nanocrystalline structure gave rise to superior plastic flow resistance without hampering the transformability. The lower right inset indicates that the grain refinement-induced decrease in the irrecoverable strain levels has indeed resulted in superior transformation strains. For example, the maximum recoverable strain of 3.3% at 250 MPa in the as-received sample is reduced by 0.4% in the ECAE one. Similarly, Ni-Ti-Pt alloys undergoing grain refinement treatments have demonstrated superior strain recovering properties at high temperature [146–148].

7.2. Predictions from first principles

Simulation-wise, the effect of adding a third element to the binary NiTi lattice is studied for the case Ni-Ti-Pt in details. Hatcher et al. [149,150] have examined the possibility of occurrence of slip on various slip planes, and pinpointed the minimum energy pathways using Ni-Ti-Pt lattice. It was noted that the addition of Pd have very similar effects as the Pt. The shape of the energy landscape was similar although the energy magnitudes differed as expected. It was found that the addition of Pt to the NiTi binary lattice overall reduces the energy barriers. This indicates a decreased resistance to lattice shearing (i.e. low impedance to dislocation slip). On physical ground, this finding particularly explains the relative poor plastic resistance in the as-received materials discussed in the previous section. With the introduction of an increased number of grain boundaries (i.e. slip obstacles), the overall plastic resistance was improved. The combined experimental and predictions reinforce the importance of mesoscale factors for improving SMA slip properties.

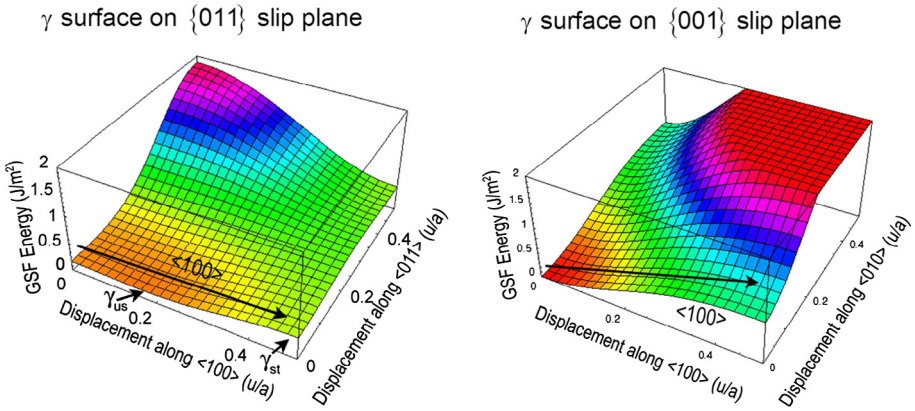

Fig. 29. DFT-computed γ surfaces on the planes {0 1 1} and {0 0 1} in the austenitic Ni-Ti-Pt lattice [149]. The arrows indicate minimum energy pathways. These energy considerations help understand the slip tendency in generic Ni-Ti-X (X = Pd or Pt) SMAs given the similarities of the lattice scale attributes of Pd and Pt.

On the atomistic ground, Hatcher et al. conducted extensive sensitivity tests on the number of layers used for γ surface calculation as well as on the adopted relaxation methods. A strong dependence of these variables on the energy magnitudes was reported. Upon establishing the functional dependence of layers and atomic relaxation, the minimum energy pathways to slip on the {0 1 1} and {0 0 1} planes were predicted as in Fig. 29. The arrows indicated the minimum energy pathways i.e. the most likely shear direction for slip nucleation on the designated plane. From the energetics, the slip systems, $\{0\,1\,1\}\langle 1\,0\,0\rangle$ and $\{0\,0\,1\}\langle 1\,0\,0\rangle$, were predicted to be the most likely ones.

8. Ni-Ti-Hf SMAs (experiments and atomistic predictions)

8.1. Experimental behaviors

Due to the low cost of Hf, the Ni-Ti-Hf remains a promising SMA particularly for high temperature applications. Plastic deformation is known to occur in both austenitic and martensitic phases in Ni-Ti-Hf based SMAs [142,151,152]. Examples of plasticity-dominated superelastic loops and the isobaric strain-temperature behavior are presented in Fig. 30 [151]. The superelastic behavior of Ni-Ti-Hf specimens aged at 650 °C for 3 hours is characterized by residual strains, which increases with temperature (from 210 °C to 250 °C). The enhanced degree of irreversible strain is attributed to the coarsening of precipitates as a direct outcome of heat treatments. This essentially indicates that finer precipitates would provide more effective resistance to plastic flow, a trend also observed in Ni-Ti-Pd and Ni-Ti-Pt based SMAs. Owing to the same reason, the isobaric shape memory responses (middle inset in Fig. 30) also undergo degradation in shape recovery attributes in the form of larger hysteresis and non-closure of strain-temperature loop, for example, at 500 MPa. An electron microscopy study of the microstructure further confirmed the presence of residual dislocation slip in the martensitic matrix (rightmost inset).

It follows from these experimental works that elevating the impedance to plastic flow (e.g. via severe plastic deformation) leads to an enhanced shape recoverability [142]. As the underlying rationale, it has been suggested that the mechanical treatment causes the pre-existent slip to undergo work-hardening facilitated by fine precipitates. In addition, it has been suggested that the presence of precipitates can also set local preference for martensitic variant nucleation, which may have profound effect on the macroscale response. Further discussion of these issues, particularly, the beneficial roles of precipitates are provided in Section 13. Calculation of atomistic resistance to slip for particular slip systems in martensitic crystal has been undertaken, to uncover the preference for different slip systems, which is described next.

8.2. Predictions of slip energetics

The lattice structure of Ni-Ti-Hf martensite can be of either monoclinic (B19′) or orthorhombic (B19) depending on the Hf content. We discuss two different compositions of Ni-Ti-Hf SMAs from literature [58] as follows. The martensite phase of the alloy $Ni_{50}Ti_{37.5}Hf_{12.5}$ has a monoclinic crystal with the slip system being $(0\,0\,1)[1\,0\,0]$ type as shown in Fig. 31 [58]. In the GSFE curve, the existence of the local energy minimum at the midpoint indicates a propensity to slip dissociation. With addition of more Hf, the orthorhombic crystal structure is found to be more energetically favorable in the martensitic phase of $Ni_{50}Ti_{25}Hf_{25}$ SMA. There exist two possible slip systems for the orthorhombic case: $(0\,1\,1)[0\,1\,\bar{1}]$ and $(0\,1\,1)[1\,0\,0]$ [58] (Fig. 32). The computed GSFE plots for these slip systems are presented in Fig. 33. It follows that the $(0\,1\,1)[0\,1\,\bar{1}]$ slip is likely to undergo dissociation reactions, generating planar faults (e.g. an APB). This fact is indicated by the presence of the energy saddle point at the mid-displacement (of the entire span of the Burgers vector). However, the energy barrier for this system is higher than the $(0\,1\,1)[1\,0\,0]$ one. The $(0\,1\,1)[1\,0\,0]$ slip system possesses a symmetric energy profile with lower peak energy. In other words, the $(0\,1\,1)[1\,0\,0]$ slip is predicted to be more favorable of the two systems studied. Experimentally, the pres-

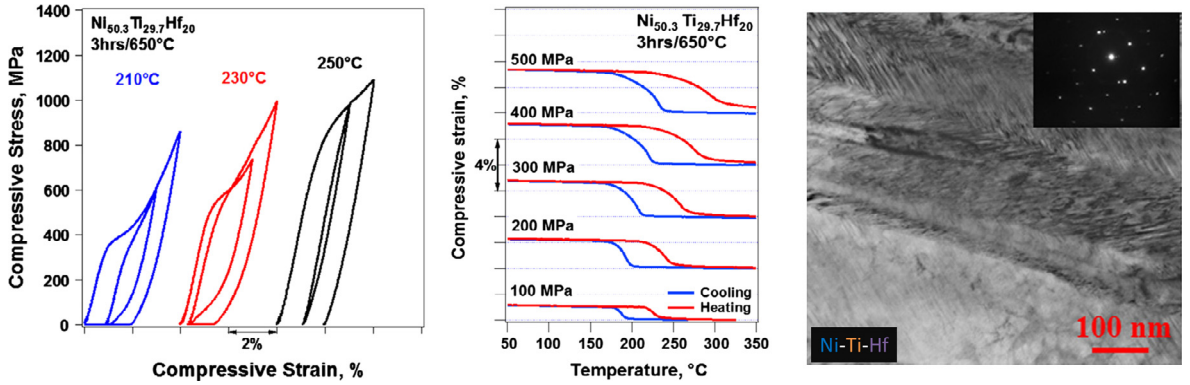

Fig. 30. Experimental observation of stress-strain (left) and strain-temperature (mid) responses subjected to plastic deformation in Ni-Ti-Hf SMAs; (right) TEM evidence of dislocations in the martensitic matrix of Ni-Ti-Hf alloys (as-extruded samples) [151].

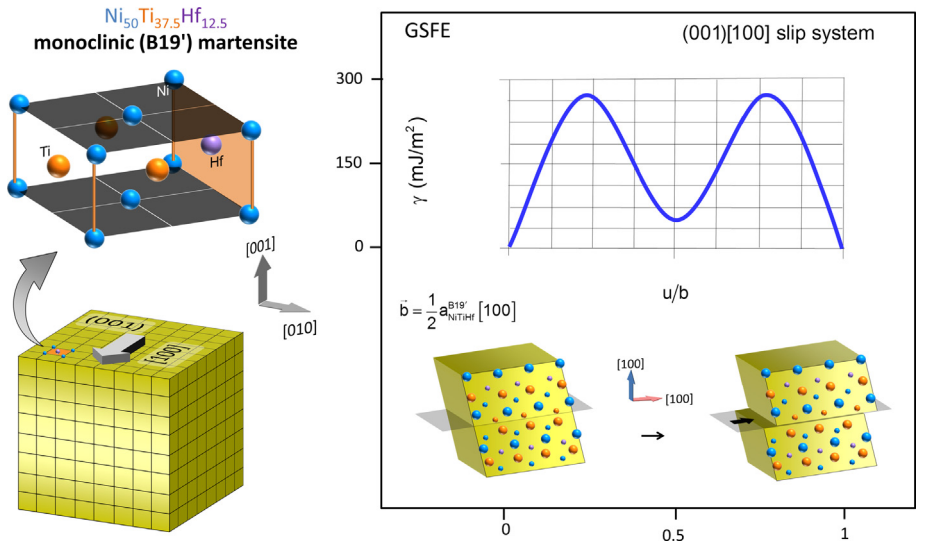

Fig. 31. (Left) the monoclinic (B19′) martensitic primitive cell (left) in $Ni_{50}Ti_{37.5}Hf_{12.5}$ SMA and the $(0\,1\,1)[1\,0\,0]$ slip system. (Right) the GSFE curve for the $(0\,1\,1)[1\,0\,0]$ slip system in $Ni_{50}Ti_{37.5}Hf_{12.5}$ SMA [58]. The fault energy profile is similar to many others discussed before with a characteristic energy minimum, which indicates a strong propensity of creating partial slip connected by a planar fault.

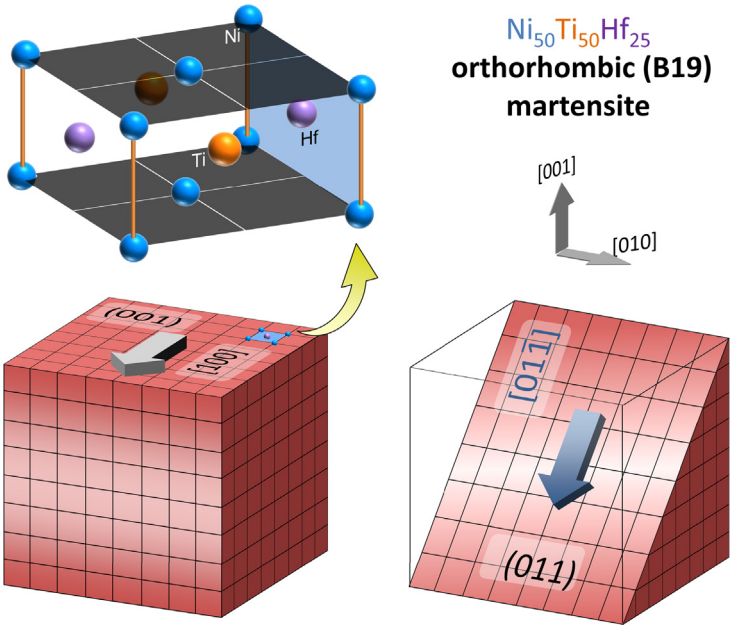

Fig. 32. The $Ni_{50}Ti_{50}Hf_{25}$ martensite consists of orthorhombic (B19) lattice type. The slip systems in the orthorhombic crystals are: $(0\,0\,1)[1\,0\,0]$ and $(0\,1\,1)[0\,1\,\bar{1}]$.

ence of planar faults (APBs) has been evidenced as shown in Fig. 34 [152], which is also predicted by the shapes of the GSFE curves. An additional commentary on the prediction of critical stresses from the energetics in Ni-Ti-Hf lattices is provided in Section 12.

9. Slip in Ti-based SMAs (Ti-Nb-Zr and Ti-Nb-Ta)

The case study of Ti-Nb-Zr and Ti-Nb-Ta SMAs is particularly interesting in view of their pronounced composition dependence. While the Ni-Ti-Pd and Ni-Ti-Hf cases exemplify significant case studies on mesoscale sensitivity (e.g. to grain refinement), the composition effects in Ti-Nb-Zr and Ti-Nb-Ta alloys create an opportunity to study a direct correlation between

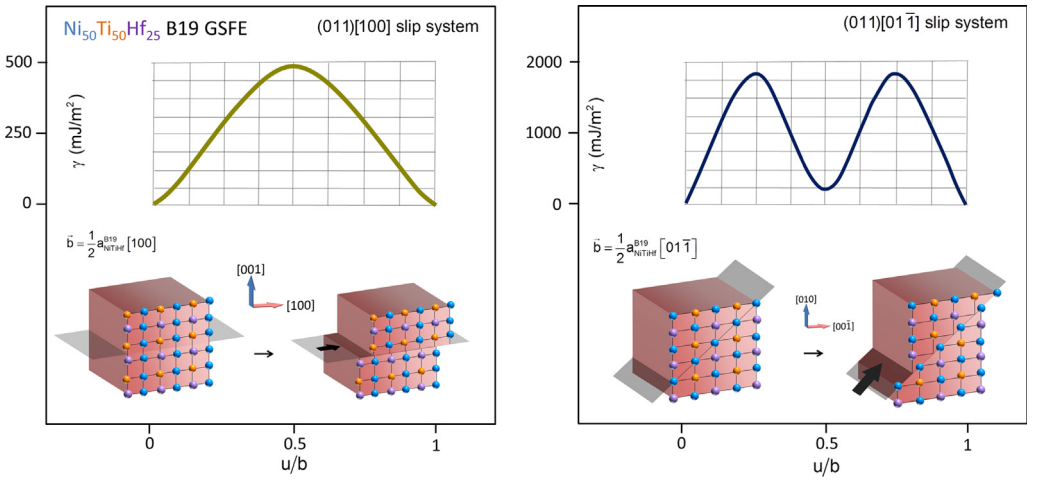

Fig. 33. The GSFE curves for the $(0\,0\,1)[1\,0\,0]$ and the $(0\,1\,1)[0\,1\,\bar{1}]$ slip systems in $Ni_{50}Ti_{50}Hf_{25}$ SMA. The former is more likely to occur in the orthorhombic crystals of $Ni_{50}Ti_{50}Hf_{25}$ due to its lower energy cost [58].

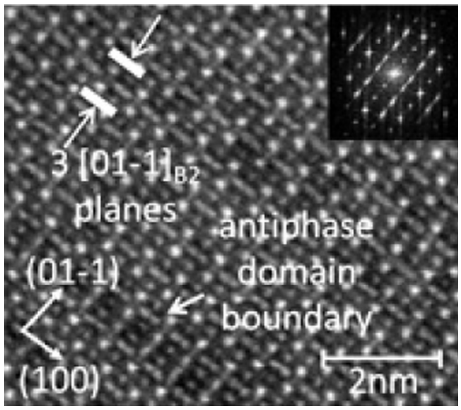

Fig. 34. Experimental evidence of anti-phase boundary (APB) in Ni-Ti-Hf martensite via high resolution TEM [152].

solid solution effects and macroscale properties. To gain a better insight, we put together experimental and predicted results side by side in Fig. 35. In the following sections, we explain the experimental behaviors first, and then the predicted results.

9.1. Empirical trends

The top left and right insets in Fig. 35 provide a summary of the experimental behaviors for a range of compositions for Ti-Nb-Zr and Ti-Nb-Ta SMAs respectively (adapted from [153,154]). The darkshaded region represents the degree of transformation strain (as quantified by the colorbar). The compositions exhibiting superelasticity and shape memory effects are marked with solid and open circles while the compositions having neither attribute are marked with up and down triangles respectively. The salient observations from the experiments can be summarized as follows:

- Strain recovery can be achieved (in the form of superelasticity and shape memory effects) over a wide range of compositions in these SMAs. The trends in terms of composition are of highly variable nature. The alloys showing high transformation strains belong to the darkest-shaded regions, which is also a strong function of composition.
- The impact of Ta or Zr alloying is possibly rooted on how they vary the lattice constants both in the austenitic and martensitic phases. Such modifications to the lattice scale would also have significant influences on the slip energetics. The DFT-computed slip energetics in particular shed further light on these empirical trends (discussed next).

9.2. Ab-initio predictions of γ energy levels

Predicted unstable stacking fault energy (γ_{us}) in both class of alloys [56] are shown in the bottom insets of Fig. 35. It follows that the γ_{us} magnitudes for all Ti–Nb–Ta alloys are higher than that of Ti–Nb–Zr alloys for the same Ti and Nb contents.

For the Ti–Nb–Zr alloys, the maximum γ_{us} values lie in the regime of high Nb and high Zr content. For Ti–Nb–Ta alloys, the maximum γ_{us} values are predicted in low Nb and high Ta contents. The lower γ_{us} values for Ti–Nb–Zr lie at the constant Nb content (of 12.5 at.%). By contrast, for the Ti–Nb–Ta alloys, the same is observed in low Ta and low Nb composition.

Quite interestingly, the trends of the composition dependence of the γ_{us} is strongly correlated with experimental behaviors [153,154]. For instance, the composition ranges with low slip energy barriers (marked as blue regions in the lower insets) correspond to the high transformation strain in the experiments (dark shaded). Similarly, the regions with no empirical superelasticity or shape memory effects (white areas in the upper insets) correspond to the high γ_{us} regimes in the theoretical maps (shaded with red). This strongly suggests that the origin of the empirical composition effects can be traced directly to the discrete lattice effects subjected to alloying. It is very likely that the influence of atomistic energetics may be mitigated to some extent while being translated to the macroscale attribute due to the predominance of mesoscopic factors (grain size, boundary distribution, etc.). Nonetheless, the discovery of the alloying-dependent energy considerations instigates further examination.

10. Perspective on slip and transformation: comparing experiment and theory

As discussed earlier, slip-induced degradation in SMAs can occur in conjunction with evolving transformed domains. It is not contingent upon reaching the macroscopic plastic yield in order for microscopic dislocation activities to initiate. Mesoscale incentives (e.g. interfacial incompatibility, preferentially oriented grains) can generate sufficiently high internal stresses to trigger plasticity locally. Manifestation of microscopic irreversible straining has been empirically associated, for example, with functional fatigue, and gradual degradation of recoverability. A comprehensive physical theory delineating these mesoscale phenomena remains an open and promising research avenue. In this context, the energetic assessment from first principles in particular can assist in establishing the relative plastic predisposition of defect-free phases, as a first step.

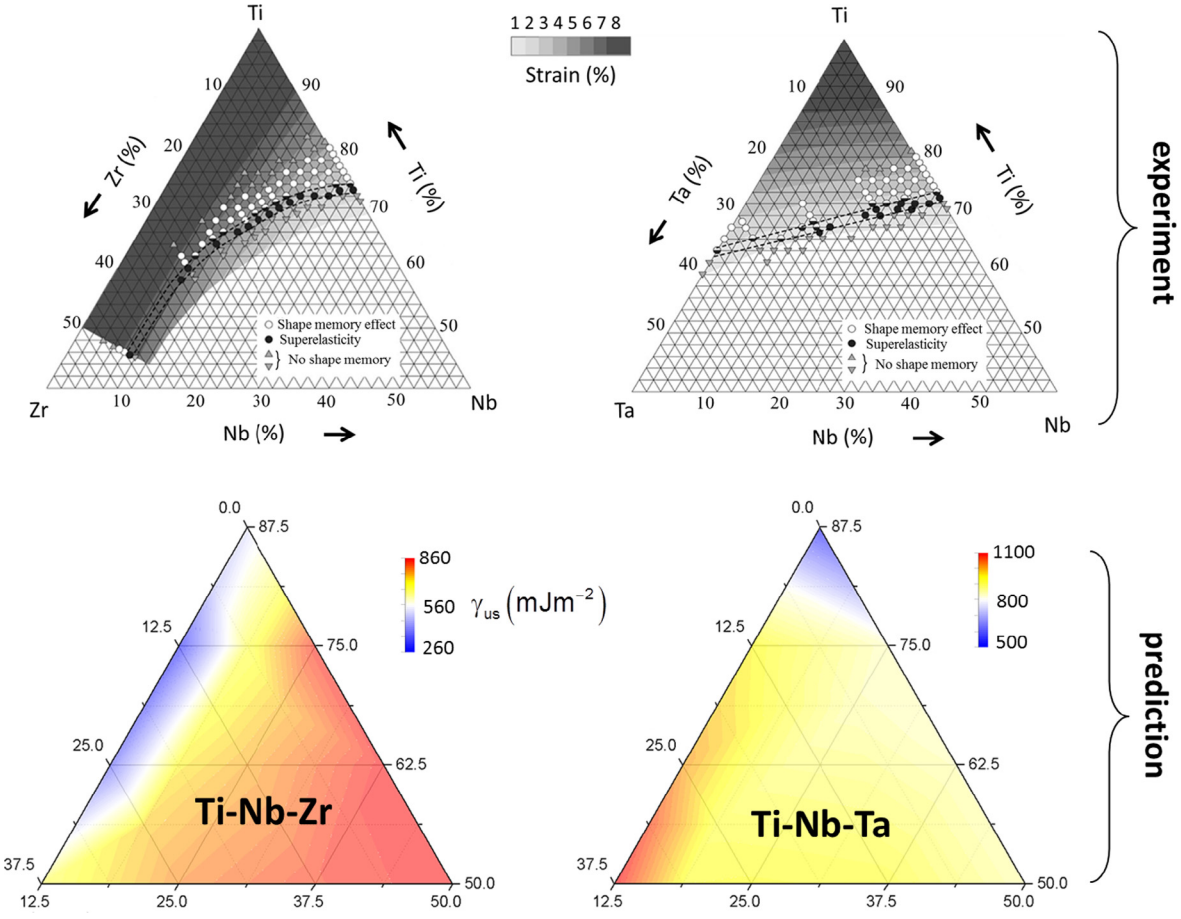

Fig. 35. (Top) A summary of experimental constitutive behaviors in Ti-Nb-X (X = Zr or Ta) alloys for a wide range of compositions (adapted from [153]). (Bottom) Composition dependence of fault energetics (expressed in terms of unstable stacking fault energy, γ_{us}) in Ti-Zr-Nb and Ti-Nb-Ta based SMAs [56]. The existence of such composition sensitivity of the fault energetics is predicted to be the cause of a considerable variation in the slip resistances (i.e. Peierls stresses).

To make our point, we first present a 3D-like compendium of experimental and theoretical data [55,155] for a range of SMAs in the form of Fig. 36. The plotted parameters are: (a) *"transformation temperature"* (in °C) i.e. the austenite finish temperature (Af), (b) *"slip strength"* (in MPa), which is the stress to initiate macroscale plasticity (measured at M_d, the highest temperature beyond which no superelasticity occurs), (c) *"recoverable strain"* which is the transformation strain (i.e. total strain minus elastic and plastic ones) and (d) theoretical (normalized) slip resistance of pristine phase, γ_{us}/b. The left, bottom and right (blue, maroon and dark-shaded) graphs respectively contain: (i) *recoverable strain* against *slip strength* (both experimental), (ii) *recoverable strain* versus *transformation temperature* (both experimental) for the same set of materials and (iii) γ_{us}/b (predicted) versus *transformation temperature* (experimental) for select SMAs. Ellipse-type data representations are adopted to indicate their scattering. Extending lines connecting left and right graphs to the bottom one indicate the plotting of the same magnitudes of the temperature and strain. To understand the significance of Fig. 36, it is helpful to recall that the desired SMA properties include: (i) very high slip resistance so that irreversible deformation is precluded, (b) low transformation stress such that two-way phase transformation occurs with increased spontaneity, (c) high recoverable strain, which imparts enhanced degree of deformation healing ability, and (d) high/low transformation temperatures (A_f) depending on application. Keeping these facts in mind, the graph-wise salient observations and explanations are provided as follows.

– Transformation temperature versus recoverable strain (bottom, maroon-shaded graph):
- At the extremities of the temperature and strain spectra are Ni-Ti-Hf (highest) and Fe-Ni-Co-Ti (lowest) alloys.
- In particular, Ni-Ti-Hf SMAs demonstrate considerable composition dependence. While a recoverable strain as high as 20% is achievable in one composition (designated "NiTi13Hf"), high transforming temperature can also be accomplished by another alloy, "NiTiHf25", reaching about 380 °C (although at the expense of recoverable strain).

– *Recoverable strain* versus *slip strength* (left, blue-shaded graph):
- NiTiHf25 possesses the maximum slip strength while Cu-Ni-Al having the least plastic resistance. Since Cu-Ni-Al also has lower transformation temperature (less than 150 °C), it is mostly suitable for low temperature applications. On the other hand, Ni-Ti-Hf outweighs all other SMAs in terms of slip strength (reaching 1500 MPa), recoverable strain (20%) and transformation temperature (nearly 400 °C).

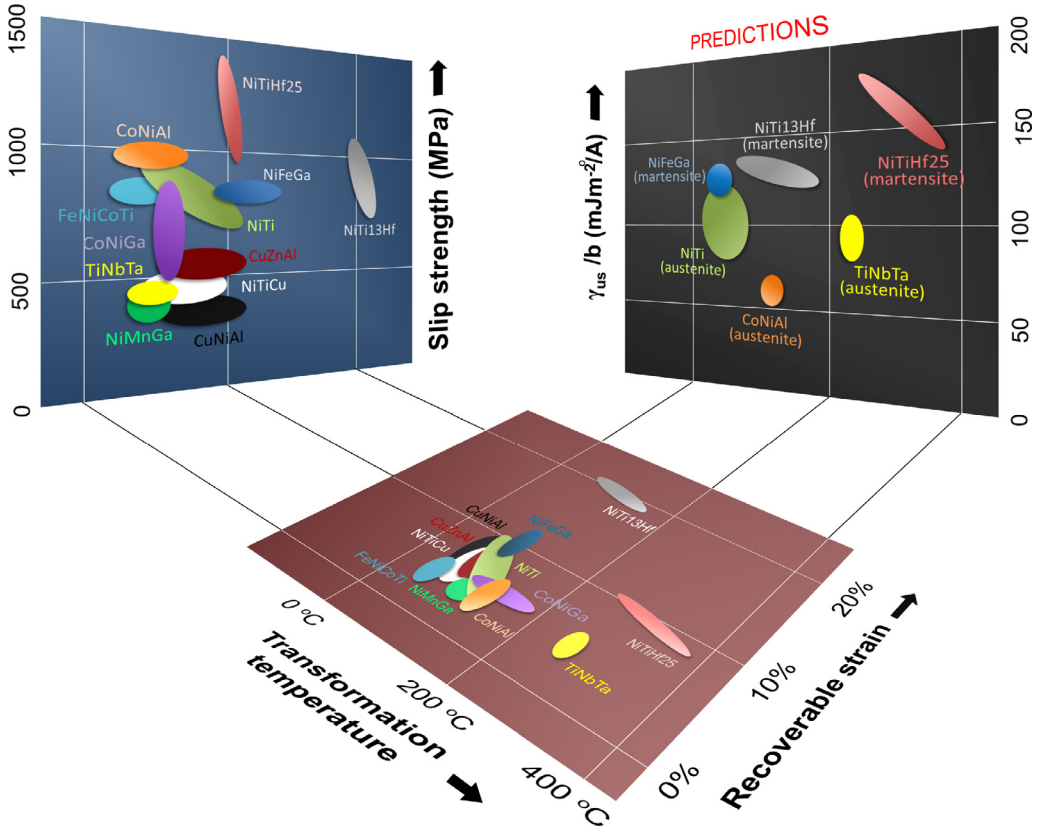

Fig. 36. (Left – navy blue shaded plot) the spread of slip resistance (MPa), and transformation strain (%) in SMAs; (bottom – maroon shaded plot) the scatter of transformation strain and transformation temperature (°C) for the same set of materials; (right - dark-shaded) predicted slip resistance of defect-free austenite or martensite crystals in selected SMAs from the other two plots. Adapted from [55,155].

- From bottom and left graphs together, one can seek out other desired combinations in the presented alloys such as Ni-Fe-Ga (>750 MPa and > 10%).

– Predicted γ_{us}/b versus experimental *transformation temperature* (right, dark-shaded graph):
- Theoretical slip energy barriers of select SMA phases conform to their experimental trends in terms of slip strength (compare with the left graph).
- It is important to note that experimental slip strengths plotted include single- and poly-crystal data while the predictions are based on pristine single crystals. Due to numerous mesoscale effects, empirical and theoretical slip resistances are not expected to have one-to-one correspondence. Nevertheless, it is remarkable that the relative slipping propensity is strikingly comparable between experiment and theory. This finding bears significant mechanistic insight. From this comparison, it is quite reasonable to assume that the pristine slipping resistances of individual phase most possibly determine the plastic deformation tendency.

By juxtaposing the available empirical and predictive literature, the diagram has unveiled a concise yet informative framework for performing comparison and developing intuition. The most important takeaway message probably is the fact that the energy-based dislocation impedance of defect-free lattice could prove a reliable metric to consider for modeling SMA plasticity. Potential avenues to that end are discussed in Section 13.

11. Prediction of Peierls stresses using DFT-based energetics

To begin our discussion on predicting the critical stress demarcating the onset of plasticity, it is important to first elucidate the concept of the upper bound for the lattice friction stress, the so-called ideal shear strength, τ_{ideal}. This parameter can be directly calculated from the maximum slope of the GSFE curve [156].

$$\tau_{ideal} = \left(\frac{\partial\gamma}{\partial u}\right)_{max} \tag{7}$$

Thus-calculated τ_{ideal} values in austenitic and martensitic phases are presented in Table 1 for several SMAs. It follows that the magnitudes of the τ_{ideal} levels are fairly high. However, the usefulness of this metric remains in the form of comparing the relative slip strengths in different crystal lattices. To compare with experimentally determined critical resolved shear stress (CRSS), we need the Peierls stresses. It should be noted that the τ_{ideal} calculated from the GSFE accounts for the anisotropy of the system and includes no continuum approximation. Consequently, the τ_{ideal} differs from actual experimental CRSS levels since the energy associated with the creation of a ledge (as denoted by the Burgers vector) during slip nucleation, and effects related to reconstruction of the non-continuum dislocation core are neglected. Consideration of both elastic and discrete lattice aspects of slip leads to the prediction of accurate levels of friction stresses comparable to experimentally determined CRSS.

11.1. Fundamentals of Peierls-Nabarro (PN) stress prediction

The Peierls-Nabarro (PN) model can be used for predicting lattice frictional stresses [60,61,157,158] comparable to experimental CRSS magnitudes. The fundamental assumption is that a dislocation is embedded in a continuous elastic medium, and glides on a plane having periodically varying potential energy surface [42]. The presence of the dislocation creates a long-range elastic disturbance field known as the so-called "disregistry". The physical significance of the disregistry (denoted by a function, $f_{disregistry}$) is that it represents the horizontal displacement differential of the atoms (before and after the occurrence of slip) across the slip plane [159,160]. The lattice energy topography gives rise to the resistance to dislocation slip. The critical stress to nucleate dislocation slip (τ^{slip}_{CRSS}) is a function of the $f_{disregistry}$ and the γ surface, both of which can be parameterized into one variable, $E_{GSFE} = E_{GSFE}(f_{disregistry}, \gamma)$. The E_{GSFE} is the total energy expenditure that is to be overcome by applied stresses. Thus, the τ^{slip}_{CRSS} for nucleating a single dislocation located at u with a Burgers vector $\vec{b}$ can be obtained as follows:

$$\tau^{slip}_{CRSS} = \left(\frac{1}{b}\frac{\partial E_{GSFE}}{\partial u}\right)_{max} \tag{8}$$

The first step to predicting the τ^{slip}_{CRSS} is to assign the accurate disregistry for any geometry of slip. For example, a full slip has the mathematical expression for the $f_{disregistry}$ [42]:

$$f_{disregistry} = \frac{b}{2} + \frac{b}{\pi}\tan^{-1}\left(\frac{x}{\zeta}\right) \tag{9}$$

where x is the position of the dislocation such that $x = ma' - u$; m is ideally infinity but assumed a large number for numerical efficiency; ζ the core half-width of individual partials ($\zeta_{screw} = a/2\sqrt{3}$ and $\zeta_{edge} = a/2\sqrt{3}(1-\upsilon)$; υ is the Poisson's ratio a' is the lattice periodicity i.e. the shortest distance between two equivalent atomic rows in the Burgers vector direction. Typ-

Table 1
Slip system, slip energy barrier (γ_{us}), predicted critical resolved shear stress (τ_{CRSS}^{slip}) and experimental CRSS levels for select SMAs.

Material (lattice type)	Slip system	γ_{us} (mJ m^{-2})	τ_{ideal} (MPa)	Predicted τ_{CRSS}^{slip} (MPa)	Experimental CRSS range (MPa)
NiTi austenite (B2)	$(0\,1\,1)[1\,0\,0]$	142	2667	710 [59]	400–800 [106,125,164,165]
	$(0\,1\,1)[1\,\bar{1}\,1]$	660	5561	1200 [59]	
	$(0\,1\,1)[0\,\bar{1}\,1]$	1545	12,847	–	
	$(\bar{2}\,1\,1)[1\,1\,1]$	847	7430	–	
	$(0\,0\,1)[0\,1\,0]$	863	9320	–	
Ni_2FeGa austenite ($L1_2$)	$(1\,\bar{1}\,0)[1\,1\,1]$	200	3700	630 [59]	400–650 [126]
	$(1\,\bar{1}\,0)[0\,0\,1]$	263	9500	–	
Ni_2FeGa martensite ($L1_o$)	$(1\,1\,1)[\bar{1}\,0\,1]$	932	9760	5800 [59]	700–1000 [59]
	$(1\,1\,1)[\bar{1}\,1\,0]$	723	8360	3130 [59]	
	$(1\,1\,1)[\bar{2}\,1\,1]$	360	4700	1260 [59]	
	$(1\,1\,1)[1\,1\,\bar{2}]$	168	3650	1100 [59]	

ically, a′ is the entire span of displacement of a GSFE curve spanning two closest zero γ values. Once the $f_{disregistry}$ is established, the energy expenditure term, E_{GSFE} can be modeled, the most generic form of which in the literature is written as below [42,159,160].

$$E_{GSFE} = \sum \gamma(f_{disregistry})a' \tag{10}$$

Let us consider the simplest shape of a GSFE plot i.e. a symmetric one with only one energy peak (γ_{us}) with no local minimum, and is symmetric about the midpoint (e.g. those in Figs. 9, 12, and 33). The E_{GSFE} term for such a case can be expressed in terms of a simple cosine function:

$$E_{GSFE} = \frac{\gamma_{us}}{2}\left(1 - \cos\frac{2\pi f_{disregistry}}{b}\right) \tag{11}$$

11.2. Specializing PN model for slip in ordered SMA lattices

As discussed earlier, in various ordered lattices (austenitic or martensitic) in SMAs, the slip energy pathways imply to the existence of either partial or full slip. The τ_{CRSS}^{slip} in case of a full slip can be predicted using Eqs. (8)–(11). Sometimes, more than two partials can form upon splitting of a full dislocation along with specific planar faults (for example, slip in Ni_2FeGa austenite in Fig. 26). Prior to modeling such case, let us first consider an extended dislocation consisting of a pair of partials separated by a planar fault of width d. The $f_{disregistry}$ for a single planar fault is modified as follows [160,161].

$$f_{disregistry} = b + \frac{b}{\pi}\left[\tan^{-1}\left(\frac{x}{\zeta}\right) + \tan^{-1}\left(\frac{x-d}{\zeta}\right)\right] \tag{12}$$

For complex shapes of GSFE profiles (e.g. Figs. 8, 10, 14, 19, 21 and 26), multiple trigonometric functions can be used formulating Fourier-like expressions. For example, a symmetric GSFE curve with two maxima (γ_{us}) and one minimum, γ_{isf} (e.g. Figs. 8, 14, 21, and 33) can be segmented using trigonometric functions. Note that such a shape of GSFE is typical of fcc partial slip. Thus, the expression for the E_{GSFE} becomes as follows:

$$E_{GSFE} = \underbrace{\sum_{m=-\infty}^{m=+\infty}\left[\gamma_{us}\sin\frac{\pi f_{disregistry}}{b_{\langle 1\,1\,2\rangle}}\right]b_{\langle 1\,1\,2\rangle}}_{\text{GSFE for } 0\leqslant u_{\langle 1\,1\,2\rangle}/b_{\langle 1\,1\,2\rangle}\leqslant 0.5} + \underbrace{\sum_{m=-\infty}^{m=+\infty}\left[\frac{\gamma_{us}+\gamma_{isf}}{2} - \frac{\gamma_{us}-\gamma_{isf}}{2}\sin\frac{\pi f_{disregistry}}{b_{\langle 1\,1\,2\rangle}}\right]b_{\langle 1\,1\,2\rangle}}_{\text{GSFE for } 0.5<u_{\langle 1\,1\,2\rangle}/b_{\langle 1\,1\,2\rangle}\leqslant 1} \tag{13}$$

Now, for multiple planar faults (e.g. Figs. 20 and 26), one needs to determine the splitting distances among the dislocations. The separations, d_1 and d_2, of the partial dislocations can be obtained by balancing the attractive (due to planar fault) and repulsive forces (due to elastic interaction) among partial dislocations [162,163].

$$\gamma_{NN} = \frac{\mu b^2}{2\pi}\left(\frac{1}{d_1} + \frac{1}{d_1+d_2} + \frac{1}{2d_1+d_2}\right) \tag{14}$$

$$\gamma_{NNN} - \gamma_{NN} = \frac{\mu b^2}{2\pi}\left(\frac{1}{d_2} + \frac{1}{d_1+d_2} - \frac{1}{d_1}\right) \tag{15}$$

Eqs. (14) and (15) can be solved simultaneously to obtain d_1 and d_2 in $L2_1$ Ni_2FeGa austenite. Similarly, d_1 and d_2 for most favorable slip (extended) in Ni_2FeGa martensite (Fig. 26) can be calculated by using γ_{CSF} and $\gamma_{APB} - \gamma_{CSF}$ in the right hand

sides of Eqs. (14) and (15) respectively. Once the inter-dislocation splitting distances are known, the total disregistry for the extended slip can be obtained by linear algebraic summation as in Eq. (16):

$$f_{disregistry} = 2b + \frac{b}{\pi}\left[\tan^{-1}\left(\frac{x}{\zeta}\right) + \tan^{-1}\left(\frac{x-d_1}{\zeta}\right) + \tan^{-1}\left(\frac{x-d_1-d_2}{\zeta}\right) + \tan^{-1}\left(\frac{x-2d_1-d_2}{\zeta}\right)\right] \quad (16)$$

Fig. 37 illustrates the fundamental assumptions of the Peierls-Nabarro concept. The upper schematic represents the atomic geometry of a dissociated dislocation (pure edge type). The lattice resistance is given by the GSFE curve and the elastic distortion in terms of the disregistry ($f_{disregistry}$) for several dissociation geometries after Eqs. (9), (12) and (16) for full slip, two partials and four partials respectively. Once the $f_{disregistry}$ is modeled appropriately for a certain slip geometry, the corresponding E_{GSFE} can be computed using functions similar to Eq. (13). Using the appropriate $f_{disregistry}$ and E_{GSFE}, one can compute the τ_{CRSS}^{slip} using (8). Next, we discuss the predicted levels of τ_{CRSS}^{slip} in austenitic and martensitic lattices of various SMAs.

11.3. Predicted slip strengths (ideal shear and Peierls stresses) in various SMAs

The predictions of the ideal shear strength as well as the Peierls stress provide a convenient proving ground for comparing the atomistic theories with experimental measurements. For instance, while the τ_{ideal} can be used as a parameter for upper bound of slip strength, the τ_{CRSS}^{slip} can directly relate to the experimentally determined CRSS values of various SMAs. In this context it should be noted that the critical stress for initiating martensitic transformation increases with temperature (above A_f) whereas the τ_{CRSS}^{slip} (say, for austenite) decreases with temperature. Thus, the experimental slip stress should be determined from the empirical plot of critical stress vs. temperature. Near the M_d temperature, the material starts undergoing slip permitting no more phase transformation. Since at this stage the dislocation slip of austenite dominates the mechanical response, the CRSS at M_d is considered as the relevant experimental metric to be compared to the Peierls stress. Table 1 notes a compilation of predicted τ_{CRSS}^{slip} and τ_{ideal} for various possible slip systems in the SMAs, whose energetics has been discussed already in the previous sections. Table 2 lists more examples of the τ_{CRSS}^{slip} prediction in the B2 austenitic phases of several SMAs (Co_2NiGa, Co_2NiAl and CuZn). Among them, the critical stress for CuZn is of lowest magnitude. This is consistent with the observation that although having excellent transformation properties, CuZn suffers from considerable plastic deformation.

12. SMA slip - implications of predicted surface and Peierls stress

Determination of slip resistance is of paramount importance in the context of advancing novel shape memory alloys. Although it is the reversible martensitic phase transformations that govern the shape recoverability, the presence of slip would hamper such mechanism [16,170]. There are many SMAs studied in the literature, which possess large transformation strain however with a strong propensity to plastic deformation. Examples include Cu based [171–175] and Fe based [176–179] SMAs. On the continuum lengthscale, plastic deformation is modeled based on the interaction among the dislocation slip and phase transformation [180–182]. While knowing the atomistic strengths of various slip systems could be intuitive, the prediction of mesoscale flow stress would provide a convenient conduit to directly compare the results with experimentally measured CRSS, a vital parameter for assessing plastic resistance [142].

12.1. Plastic deformation of NiTi

NiTi has remained the most widely applied and researched shape memory alloy [183]. Nonetheless, its performance in many applications has been continually plagued by the plasticity induced deterioration, particularly when it undergoes austenite to martensite transformation [184]. Austenitic phase of NiTi SMAs is known to have substantial ductility although somewhat unexpected from B2 type intermetallic lattices as discussed by Duerig [185]. One rationale for internal accommodation of plastic strain to a considerable degree (which gives rise to the macroscopic ductility) can likely be the availability of sufficient number of slip systems. Conventionally, three independent slip systems based on $\{110\}\langle 100\rangle$ family are considered when modeling NiTi plasticity as debated by Kelly [186] and Pelton et al. [114]. Experimentally, slip systems such as $\{111\}\langle 100\rangle$, $\{100\}\langle 001\rangle$ has been widely observed in a number of studies [8,11,89,90,187]. However, it is well accepted in continuum plasticity theory that a minimum of five independent slip systems are requisite for sustaining arbitrary plastic deformation in conventional (e.g. fcc) materials [188]. However, for SMAs, slip and transformation can occur simultaneously if a sufficient number of slip systems is unavailable at lower applied stress (as discussed in Section 3). Nevertheless, it is reasonable to assume that high energy barrier systems can be active at higher applied stresses (i.e. when macroscopic yielding occurs) in SMAs. To test such hypothesis, one can start examining the equivalent lattice structure in other materials. For instance, the slip system $\{110\}\langle 111\rangle$ has been observed in ordered intermetallic alloys with B2 lattice such as β-CuZn [189] and Fe-Co alloys [124]. Although not widely evidenced in the experimental studies in NiTi alloys, the possibility of the occurrence of this plastic system in NiTi has been predicted on atomistic grounds. The predictions [106] show that there exists an order of relative strengths among the possible systems as follows:

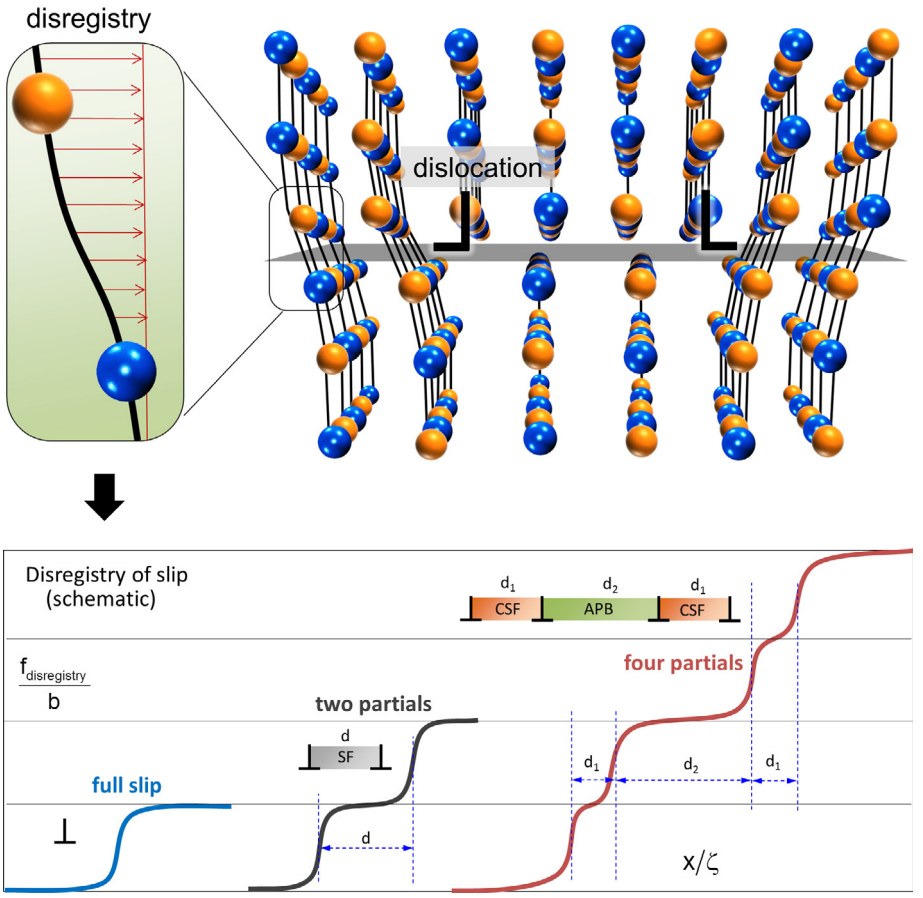

Fig. 37. (Top) a schematic illustration of Peierls-Nabarro model for predicting critical slip nucleation stress by using γ surface and the so-called "disregistry". (Bottom) Models of disregistry functions for various geometries of slip.

Table 2
Predicted τ_{CRSS}^{slip} levels (in austenite phase) are compared with experimental CRSS range for some sample SMAs.

Material (lattice type)	Slip system	Predicted τ_{CRSS}^{slip} (MPa)	Experimental CRSS range (MPa)
Co_2NiGa (B2)	$(0\,1\,1)[1\,0\,0]$	760 [59]	400–700 [166,167]
Co_2NiAl (B2)	$(0\,1\,1)[1\,0\,0]$	720 [59]	600–800 [73,166]
CuZn (B2)	$(0\,1\,1)[1\,\bar{1}\,1]$	80 [59]	30–70 [168,169]

$(0\,1\,1)[0\,\bar{1}\,1] > (0\,0\,1)[0\,1\,0] > (\bar{2}\,1\,1)[\bar{1}\,0\,1] > (0\,1\,1)[1\,\bar{1}\,1] > (0\,1\,1)[0\,0\,1]$. This fact is quantitatively corroborated both in terms of the unstable stacking energy, γ_{us}, and the ideal shear stress, τ_{ideal} as in Table 1.

12.2. Slip in Ni_2FeGa austenite and martensite

Ni_2FeGa SMAs are known to possess considerably large transformation strain (>12% in tension and >6% in compression) [79,125,128] and low temperature hysteresis. They hold significant potential for magnetic [131,190–192] and hot section applications. However, the full deformation recovery either under thermal or magnetic load is susceptible to slip induced deterioration, which can occur both in the austenitic and martensitic phases. From prediction standpoint, the minimum energy pathways control the inherent slip propensity. In particular, the most unique feature in austenitic Ni_2FeGa slip is the predominance of dissociated slip, which occur concurrently with the formation of various planar faults [57,59]. The predicted γ energy landscape clearly rationalized that the material tendency for disintegration of a full slip into multiple superpartials is caused by a lower energy cost. One qualitative way of substantiating such predictions is by means of the TEM experiments, which can provide evidence of planar defects (e.g. the APBs in Fig. 20). A prevalence of APBs in austenitic Ni–Fe–Ga has also been noted in experimental studies by Chumlyakov et al. [125]. The existence of the APBs provides

important signature of plastic deformation in this class of SMAs. As for the relative strengths of various slip systems in the austenitic Ni_2FeGa, predicting the ideal shear stress (τ_{ideal}) can serve as a rapid evaluation recipe (as in Table 1).

Evidence of dissociation-based slipping mechanism could be found in the austenitic crystal structure of $L1_2$ lattice in other shape memory alloys such as Cu-Zn-Al. For instance, observation of $\langle 1\,1\,1\rangle$ glide planes in conjunction with APBs was reported by Damiani et al. [171] and Romero et al. [168]. It has been indicated that $\langle 1\,1\,1\rangle$ type slip dominates when the APB energy (γ_{APB}) is low. With increasing γ_{APB}, the $\langle 1\,0\,0\rangle$ type slip becomes predominant [193]. The relevant atomistic energy pathways conform to such trend, in that the energy barrier for $\langle 1\,0\,0\rangle$ slip is much higher than the $\langle 1\,1\,1\rangle$ one (Fig. 18). The energy barrier for martensitic phase transformation [57] was found to be much lower (only 8.5 mJ m^{-2}) compared to that of the most likely slip systems i.e. the $\langle 1\,1\,1\rangle$ type slip (470 mJ m^{-2}). This indicates that reversible transformation (which drives the strain recovery process in SMAs) can occur without the undesired interference from slip-mediated plasticity. It should be noted that at elevated temperatures or higher strain-rates, the propensity of slip increases unlike the phase transformation.

Similar modeling approach on the martensitic ($L1_o$) lattice of Ni_2FeGa brings forth a rationale for the slip dissociation as the preferred mode of plastic deformation [59]. The γ energy topography (Fig. 23) for a full dislocation has a higher γ_{us} (475 mJ m^{-2}) compared to the energy barrier (360 mJ m^{-2}) corresponding to one of the dissociation reactions (Fig. 26). For the nucleation of individual partials on the $(1\,1\,1)$ slip plane in $L1_o$ Ni_2FeGa, the energy barrier and the Peierls stress differ significantly. For instance, the minimum energy barrier is found to be 168 mJ m^{-2} for the $[1\,1\,\bar{2}](1\,1\,1)$ slip system. The corresponding τ^{slip}_{CRSS} of 1.1 GPa is predicted to be remarkably close to the experimentally determined CRSS of 0.75 GPa [59]. The predicted CRSS magnitudes for all the slip systems in the $L1_o$ lattice of Ni_2FeGa martensite are presented in Table 1. It should be noted that despite the high CRSS value, presence of dislocation slip to some extent has been observed in the electron microscopy study. The reason could be attributed to internal stress sources caused by interfacial defects (e.g. grain and phase boundaries).

12.3. Critical slip stress in martensitic Ni-Ti-Hf alloys

As reported by Wang et al. [58], a gradual rise in the predicted τ^{slip}_{CRSS} levels with Hf addition has been noticed. The authors have attributed the origin of such trend to a very similar variation in the overall γ surface magnitude as computed from DFT simulations. Among the ternary elements (i.e. Ni, Ti and Hf), Hf has a large atomic radius of 1.55 Å [194] compared to the other species that can be alloyed with binary Ni-Ti system, e.g. Pt (1.35 Å), Pd (1.4 Å), Cu (1.35 Å), Fe (1.4 Å). The large atomic radius of Hf gives rise to an increase in the Ni–Ni and Ti–Ti bond lengths. Consequently, a high γ_{us} is encountered during the shear simulations, which in turn increases slip resistance.

It is also worth noting that the plastic deformation in the low symmetry monoclinic Ni_4Ti_3Hf lattice occurs by one available slip system of $(0\,0\,1)\,[1\,0\,0]$ type. However, in order for deformation to proceed, more independent straining systems are necessary. As a result, transformative straining would accompany the plastic flow. Also, deformation twinning would be active in the transformed regions, leading to the creation of variants and self-accommodated (martensitic) structure. One of the primary factors bringing about the observed dramatic change in the composition-dependent fault energetics is the alloying-induced modification in crystal variables such as lattice constants and monoclinic angle. From modeling perspective, such effects can be understood in terms of the geometrical relationship between the lattice constant and the Burgers vector. Since the Burgers vector is a function of the lattice constant, a modified lattice constant will eventually alter the magnitude of the Burgers vector provided the slip system remains the same. Both the lattice angle and the lattice parameter are strongly composition-dependent, which has been confirmed from DFT predictions. Given the lengthscale of the γ surface calculation, an apparently minute alteration in the bonding length/strength gives rise to dramatic variations in the fault energy levels. Most striking examples of such phenomena have been noted in the cases of Ti-Nb-Zr and Ti-Nb-Ta SMAs.

12.4. Composition dependence of martensitic slip in Ti-Nb-Zr and Ti-Nb-Ta

In Fig. 38, the predicted levels of τ^{slip}_{CRSS} as a function of Zr and Nb contents are presented based on data from [56], utilizing the DFT-computed fault energetics. The most notable finding is the highly variable nature of the τ^{slip}_{CRSS} with respect to the alloy composition in terms of both Zr and Nb contents. As observed, the role of Nb content is rather uniform, in that the CRSS level increases monotonically with increasing Nb solutes. On the other hand, addition of Zr has a more dramatic effect, which is particularly characterized by the existence of a critical composition (i.e. with the lowest magnitude). Beyond this amount, the CRSS level continues to increase. It should be noted here that such a trend is essentially founded on the composition-dependent γ_{us} variations (Fig. 35) stemming from the complex interactions among the solute atoms of different chemical species. A careful study of experimental constitutive behaviors reveals that this class of alloys indeed demonstrate such composition dependence. For example, it is observed from experiments that Ti–24Zr–13Nb does not possess superelastic attributes [153]. This particular observation is consistent with the predictions, where slip is more likely to be triggered at a predicted τ^{slip}_{CRSS} of 125 MPa for the alloy with such composition. Thus, it is only reasonable to attribute the loss of strain recoverability in Ti–24Zr–13Nb alloys to an apparent preference of slip-mediated plastic mechanism over phase transformation. Such inference can be further corroborated by observations such as Ti–25Nb alloy experimentally demonstrating pro-

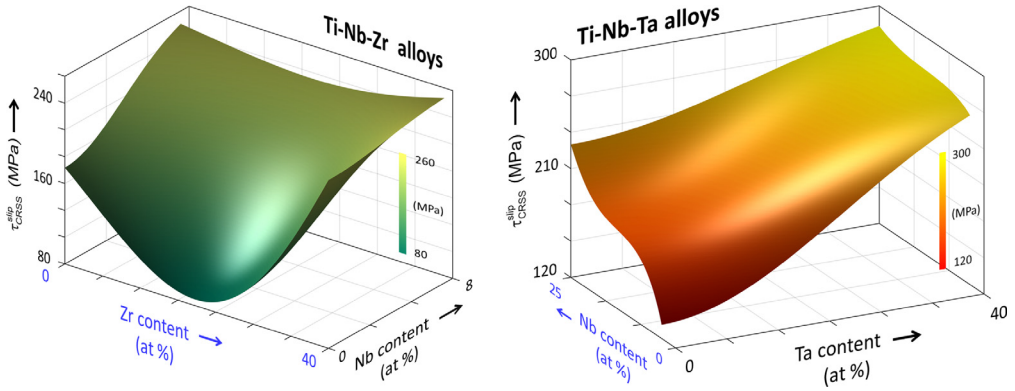

Fig. 38. Highly non-linear variation of τ_{CRSS}^{slip} with respect to composition in the martensitic Ti-Nb-Zr and Ti-Nb-Ta SMAs (adapted from Ref. [56]). Such composition dependence is reportedly related to alloying-induced γ surface variations.

nounced superelasticity. This alloy is predicted to possess a τ_{CRSS}^{slip} value of 228 MPa, which is significantly higher than that of Ti–12.5Nb–25Zr (124 MPa).

Similarly, slip resistance in Ti-Nb-Ta SMAs exhibits strong composition-dependence although less dramatic than the Ti-Nb-Zr alloys. Particularly noteworthy is the initial drop (or rise) in τ_{CRSS}^{slip} level with respect to addition Zr (or Ta), a trend that has also been noticed experimentally [154,195,196]. From the foregoing discussions, it follows that Ta can more pronouncedly increase martensitic slip resistance compared to Zr. It remains to be seen how future experimental findings further corroborate these predictions.

13. Outstanding problems and future promises

It is imperative to note that while GSFEs and Peierls stresses under pristine lattice condition accurately capture the inherent plastic strength, in real materials much more complicated deformation scenarios would be prevalent. Fracture/fatigue (i.e. cracking under static or cyclic thermo-mechanical loading), interfacial plasticity, texture effects, particle strengthening (i.e. role of precipitates), etc. constitute some outstanding problems at the sub-structural level, to be addressed. Deformation micromechanisms for these issues can also benefit hugely from similar atomistic rationalizations. We point out several potential avenues of investigations as follows.

13.1. Atomistic modeling at mesoscale: precipitates and slip

It is well known that the precipitates in SMA microstructure strongly influence the phase transformation by setting local preference for different variant nucleation [197–200]. The way that a precipitate controls the microscopic deformation is through creating internal stress gradient, which asymptotically extends into the matrix [201]. There are evidences in the literature that the precipitate-induced stress concentration can influence slip response as much as it does the transformation behavior [117]. In Fig. 39, experimental stress-strain responses of a precipitated single crystal loaded along [1 1 1] direction is presented. The increase in transformation strain towards saturation can also be noticed. A significant presence of entangled dislocations is confirmed via the TEM image. In general, a large density of nano-sized coherent precipitates has empirically been associated with having beneficial effects, say, in the form of decreasing the stress hysteresis, transformation stress as well as strain [117,202,203]. The role of precipitates could be construed as mostly obstructive to dislocation activities, rather than facilitating slip [196]. Recent molecular dynamics simulation revealing the mesoscale deformation mechanism within a precipitated austenite further attests to their beneficial role.

Many cases of using molecular dynamics simulations are already noted for solutionized NiTi [204–209]. Recently the role of precipitate is also undertaken [210]. In the left inset of Fig. 40, the superelastic response and an atomic snapshot of deformed austenite single crystal containing a coherent Ni_4Ti_3 precipitate (of 7 nm diameter) are shown (from molecular dynamics simulation). The dark lenticular region indicates the rhombohedral lattice of the Ni_4Ti_3 precipitate. Red, blue and green regions surrounding the precipitate represent different variants (consisting of B19′ lattice). It follows that the red-color variant is predominant. Despite having a high stress concentration around the precipitate periphery, no dislocation slip was generated during the deformation. The simulation results are consistent with earlier electron microscopy finding, which is shown in the right inset of Fig. 40. A preferred variant is observed to nucleate from the precipitate in the TEM (which is also schematically illustrated) in absence of slip. These studies combined with previous discussions suggest that the role of precipitate is not associated with promoting slip. In the experimental studies where considerable slip is generated in the austenitic channels, the precipitates would provide additional resistance to plasticity, thereby curtailing slip-induced straining. This notion is supported by the fact that the presence of precipitates always results in the improvement of overall

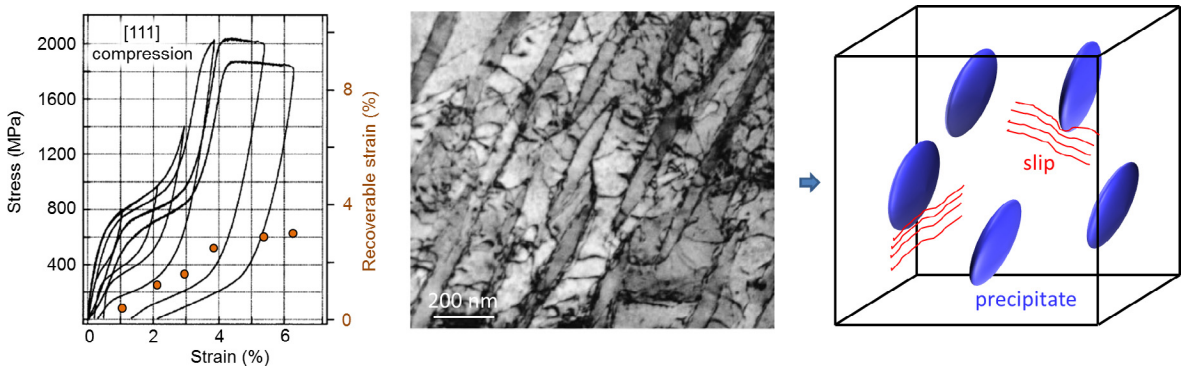

Fig. 39. (Left); Constitutive responses and recoverable strain of overaged Ti-51.5%Ni single crystal loaded along [111] crystallographic orientation (mid) presence of dislocation slip around precipitates in the austenite phase as evidenced through TEM [165]; (right) the schematic demonstrating slip-precipitate interactions based on the TEM analysis [117].

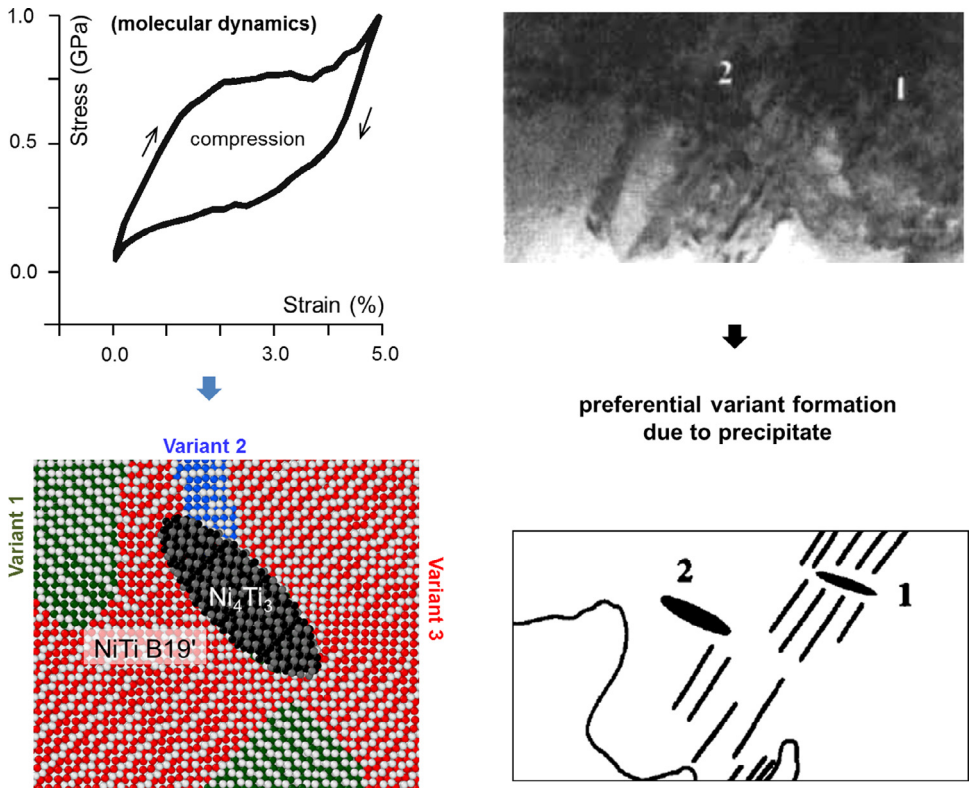

Fig. 40. (Upper left) Simulated superelastic stress-strain response of a NiTi single crystal with an embedded Ni_4Ti_3 precipitate [210]; (lower left) from molecular dynamics, a preference of one variant (red-colored) over others surrounding the precipitate is observed; (Upper and lower right) TEM microscopy evidence of one martensitic variant near the precipitates [200].

SMA properties as noted empirically. Then, the question arises regarding how resistant a precipitate can be against oncoming plastic flow. DFT based calculations can provide useful answers there as well.

Using ab initio approach, Wang et al. [211] examined the shearability of precipitates by computing the GSFE curves in some precipitate structures of $L1_2$ type lattice (considering Ni-based alloys). In general, glissile dislocations are known to have the ability to shear precipitates (in addition to being pinned or gliding around them) [212]. Thus, the DFT-based predictions of the shear resistance (i.e. GSFE curves and the associated Peierls stresses) can serve as a very useful metric to rapidly assess the slip-barrier role of a certain precipitate lattice. Furthermore, DTF-based calculations have recently established the existence of an elastic moduli mismatch between the Ni_4Ti_3 precipitate and the B2 NiTi matrix [213], indicative of the strong directional nature of the distortion fields. This finding particularly assists in forming a rationale for the directional

nature of the near-precipitate strain distributions observed experimentally [214,215]. These distortion fields give rise to the previously discussed variant nucleation preference, and most possibly resistance to the oncoming avalanche of slip. While these findings are informative, further research is needed to establish the mechanistic processes of interactions among slip, precipitate and transformed domains.

In that regard, one particularly interesting study on the concurrence of slip and transformation is reported by Pfetzing-Micklich et al. [216]. They observed dislocation slip nucleation during nano-indentation experiments on austenitic NiTi. Underneath the indent, a significant presence of slip was evidenced by TEM microscopy (Fig. 41). Experimentally it was not confirmed whether slip occurred in the austenite or martensite, which was next clarified by molecular dynamics simulations. In simulations, single crystals along [0 0 1] orientation was subjected to nano-sized indenter. With increasing indent depth, martensite starts to form (the interface between the austenite and martensite colored red in Fig. 41). At some state (when depth is 3 nm), dislocation slip (indicated by dark lines) started to nucleate in the martensitic lattice. While the volume fraction of martensite continues to increase, the presence of slip entanglements also becomes considerable. Upon withdrawing the indent (i.e. at the unloaded state), residual martensite and slip residue remained in the parent (austenitic) crystal. The simulation results are consistent with experimental findings.

13.2. Cracking of SMAs: residual austenite, martensite and slip

Damage propagation in SMAs is of a major engineering concern [217–219]. During multiple cycles, microscopic crack would generate due to massive strain localization, which progressively becomes larger and leads to the fracture of the component. The previous studies have brought into attention some important features on the mechanistic aspect of fatigue mechanisms drawing examples on NiTi [218]. During the fatigue cycling, a considerable presence of combined slip, austenite and martensites are found in the microstructure. One example is presented in Fig. 42 (adapted from [220]), where the residual microstructure is shown after 10 cycles. The TEM image (along with selected area diffraction spots in the inset) testifies to the presence of austenite and martensite bands with a high density of dislocation slip ($\sim 10^{14}$ m^{-2}). The geometry of slip is identified as the $\langle 1\,0\,0\rangle\{0\,1\,1\}$ type. It is reasonable to assume that the degree of these residues would only be augmented over cycles.

Once a microscopic crack is initiated at local weak spots, it would progressively grow to become a catastrophic one [221,222]. The scenario ahead of an advancing microscopic crack in an SMA is schematically presented in the lower inset of Fig. 42. The crack needs to propagate through the composite structure of slip, austenite and the internally twinned martensite. It is important to note that general cracking mechanisms in ductile solids are governed by the degree of irreversible processes at the tip. Generally speaking, the net irreversibility of permanent deformation for SMA fatigue could stem from: (1) residual martensite and/or (2) residual dislocation slip both ahead and in the wake of crack-tip [223–225]. Individuating the relative contributions of each physical phenomenon is a challenging task empirically, and could benefit hugely

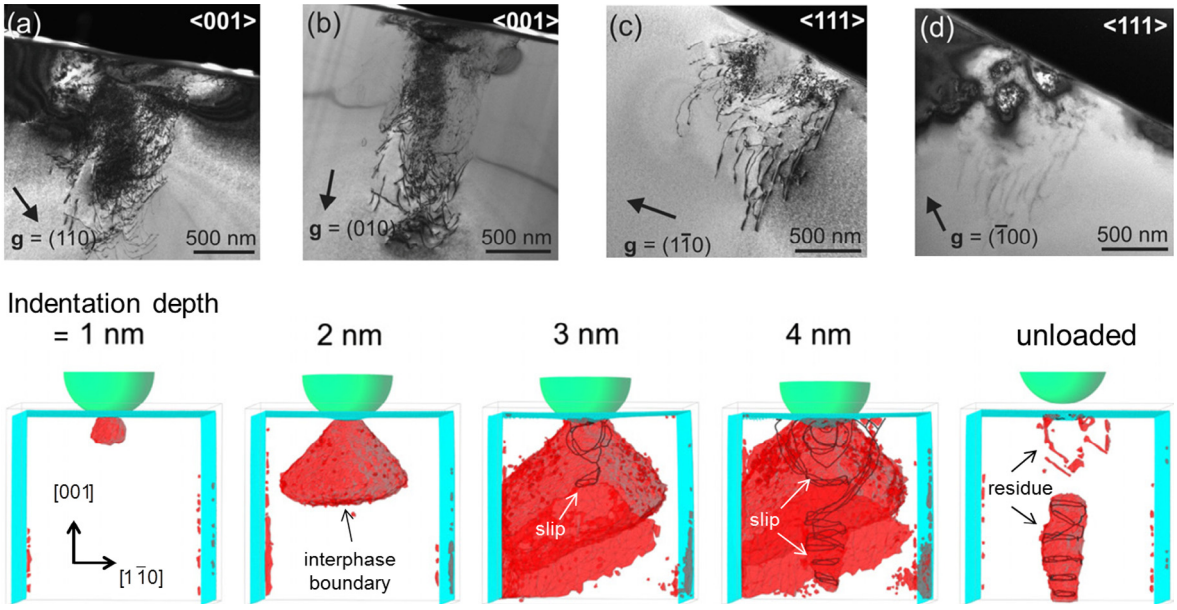

Fig. 41. (Top) Evolution of dislocation slip in NiTi austenite subjected to nano-indentation from as observed via TEM (a)–(d) [216]. (Bottom) molecular dynamics simulations of nano-indentation of NiTi austenite reproducing the slip pattern in conjunction with martensite (red colored regions indicate austenite-martensite periphery and the dark lines are the dislocations); with greater indentation depth, martensitic domains increase and slip occurs at 3 nm). The residual martensite and slip are noticed upon withdrawing the indent (i.e. at unloaded condition).

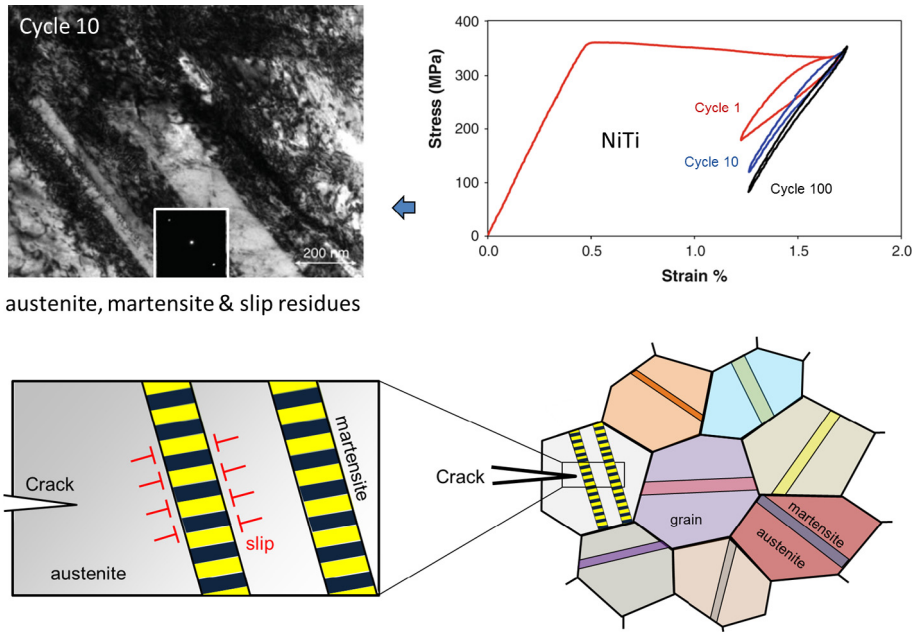

Fig. 42. (Upper right) Cyclic stress-strain curves for NiTi SMAs up to 100 cycles. (Upper Left) TEM image after 10th cycle showing residual austenite, martensite and slip [220]. (Lower) Schematic of a microscopic crack and the microstructural environment surrounding it based on the experimental observations.

from atomistically based mesoscale simulations [216,226]. Significant advances are recorded in the earlier literature with regard to modeling cracking physics using atomistic concepts. Cyclic crack growth simulations in a multi-grain environment revealed massive slip activities triggering material separation at vulnerable points such as triple joints [227–229]. Other phenomena such as twinning, void nucleation, crack branching, cleavage etc. are also addressed within the context of conventional materials [227,229–232] using molecular dynamics simulations. These developments could provide important ideas regarding the most feasible approach for the SMA damage problem with similar physical emphasis. Since the current understanding of fracture and fatigue remains a highly empirical field, it is worthwhile to purse the atomistic avenues. The pertinent challenges to that end would essentially involve separating contributions of localized dislocation slip, parent and transformed phases as well as their apparently complex interactions [223].

From the perspective of theorizing SMA cracking problem, the benefits of utilizing the γ energetics is considerable. At the discrete lattice level, the combined effects of slip resistance, phase transformation and twinning (since martensite undergoes twining) need to be incorporated. The energy barrier for slip is already addressed in this article for a range of SMAs. Prediction of energy pathway from first principles has also been undertaken in the literature for twinning [233] and phase transformation [35,234]. Attempts have been made to incorporate the slip and twinning energetics to address the cracking issue. For example, Warner et al. [231] used γ surfaces specific to slip and twinning for a crack that advances by means of slip and/or twinning. Tadmor and co-workers [235,236] provided a robust modeling framework to utilize twinning-specific γ energy landscape to assess fracture resistance. Moreover, the Peierls-Nabarro framework is also found useful for modeling crack-induced irreversible (slip-based) processes [38,222,237–241] utilizing atomistic fault energies (in conventional fcc materials). For the SMA cracking problem, the contribution of phase transition in conjunction with slip and twinning needs to be considered. Thus, it remains to be seen how similar models would be advanced based on the combination of slip, transformation and twinning energies. Given the relatively unexplored theoretical territory of SMA cracking, such an endeavor is certainly worthwhile to pursue.

13.3. Constitutive modeling: prospects of incorporating atomistics

Currently, there exist a number of SMA constitutive models in the literature. They cover the micro-mechanics of SMA deformation, which enables predictions of a wide spectrum of macroscale thermo-mechanical responses [242–246]. The prospects of fine-tuning continuum theories are far-reaching since they are directly related to engineering component issues [247]. Today, the principal challenge therein is about formulating laws to physically represent multiple mechanisms (plastic flow and phase transformation) and their subtle interactions. For example, in order to sustain plasticity to have significant influences on the macroscale constitutive responses a minimum of five independent slip systems are needed in crystal plasticity models [188]. In the event of their unavailability, transformative straining would accompany plastic flow. The phenomenological approaches simplify the mechanistic aspects of microscopic deformation by means of empirical constants

into the constitutive formulations to account for their effects. These adjusting parameters are rooted upon experimental stress-strain behaviors, and oftentimes are representative of certain microstructural features (e.g. texture, grain size). It is still a matter of further research to establish the possible slip systems in SMAs. Given that some systems would prevail over others (which require higher activation energy), their experimental determination becomes rather challenging. As a result, certain generalizations are made in the continuum theories, which may not be truly representative of actual microscopic physics (for example, assumptions of uniform strength for all slip systems). Although, atomistic considerations have not directly figured into the continuum constitutive models yet, they hold considerable promises in terms of: (i) providing detailed crystallographic analyses on the relative activation propensity of different slip systems, (ii) establishing a database of the associated Peierls stress (i.e. CRSS) to be used in mesoscale constitutive equations, and (iii) developing a hypothetical proving ground for examining alloy property enhancement strategies via fine-tuning lattice attributes.

Since most densely packed planes and directions are most vulnerable to slipping, it is worthwhile to assess their likelihood (in terms of activation energy barriers) given the availability of well-developed computational foundation discussed heretofore. The atomistic evaluations of possible crystallographic planes and directions could be particularly useful in pinpointing the mostly likely plastic systems along with predicted CRSS levels. It is important to note that a myriad of mesoscopic variables (e.g. grain distribution, size, thermo-mechanical treatment history) would ultimately factor in the overall plastic response. Nonetheless, the exploration of the theoretical territories at the pristine level could help to identify isolated roles of each factor. These predictions can serve as an educated basis of reducing trial-and-errors in the experimental test matrix when formulating novel SMA compositions.

Acknowledgement

This research is conducted with the financial support from the Nyquist Chair funds and partial support from NSF CMMI-13-33884. We are also grateful to the reviewers for insightful comments.

References

[1] Otsuka K, Wayman CM. Shape memory materials. Cambridge University Press; 1999.
[2] Shaw JA, Kyriakides S. Thermomechanical aspects of NiTi. J Mech Phys Solids 1995;43:1243–81.
[3] Yamauchi K, Ohkata I, Tsuchiya K, Miyazaki S. Shape memory and superelastic alloys: applications and technologies. Elsevier; 2011.
[4] Hartl DJ, Lagoudas DC. Aerospace applications of shape memory alloys. Proc Inst Mech Eng, Part G: J Aerosp Eng 2007;221:535–52.
[5] Jani JM, Leary M, Subic A, Gibson MA. A review of shape memory alloy research, applications and opportunities. Mater Des 2014;56:1078–113.
[6] Olson G, Cohen M. Stress-assisted isothermal martensitic transformation: application to TRIP steels. Metall Trans A 1982;13:1907–14.
[7] Bhattacharya K. Microstructure of martensite: why it forms and how it gives rise to the shape-memory effect. Oxford University Press; 2003.
[8] Simon T, Kröger A, Somsen C, Dlouhy A, Eggeler G. On the multiplication of dislocations during martensitic transformations in NiTi shape memory alloys. Acta Mater 2010;58:1850–60.
[9] Delville R, Malard B, Pilch J, Sittner P, Schryvers D. Transmission electron microscopy investigation of dislocation slip during superelastic cycling of Ni–Ti wires. Int J Plast 2011;27:282–97.
[10] Treppmann D, Hornbogen E. The effect of dislocation substructure and decomposition on the course of diffusionless transformations. Le Journal de Physique IV 1995;5. C2-211–C2-6.
[11] Norfleet D, Sarosi P, Manchiraju S, Wagner M-X, Uchic M, Anderson P, et al. Transformation-induced plasticity during pseudoelastic deformation in Ni–Ti microcrystals. Acta Mater 2009;57:3549–61.
[12] Malarría J, Lovey FC, Sade M. Two way shape memory effect in CuZnAl single crystals after pseudoelastic cycling at low temperatures. Mater Sci Eng, A 2009;517:118–24.
[13] Manchiraju S, Anderson PM. Coupling between martensitic phase transformations and plasticity: a microstructure-based finite element model. Int J Plast 2010;26:1508–26.
[14] Hamilton RF, Sehitoglu H, Chumlyakov Y, Maier HJ. Stress dependence of the hysteresis in single crystal NiTi alloys. Acta Mater 2004;52:3383–402.
[15] Lagoudas DC. Shape memory alloys: modeling and engineering applications. Springer Science & Business Media; 2008.
[16] Duerig TW, Melton K, Stöckel D. Engineering aspects of shape memory alloys. Butterworth-Heinemann; 2013.
[17] Mecking H, Kocks U. Kinetics of flow and strain-hardening. Acta Metall 1981;29:1865–75.
[18] Ma J, Karaman I, Noebe RD. High temperature shape memory alloys. Int Mater Rev 2010;55:257–315.
[19] Firstov GS, Van Humbeeck J, Koval YN. High-temperature shape memory alloys: some recent developments. Mater Sci Eng, A 2004;378:2–10.
[20] Sehitoglu H, Zhang XY, Kotil T, Canadinc D, Chumlyakov Y, Maier HJ. Shape memory behavior of FeNiCoTi single and polycrystals. Metall Mater Trans A 2002;33:3661–72.
[21] Wu Y, Patriarca L, Sehitoglu H, Chumlyakov Y. Ultrahigh tensile transformation strains in new $Ni_{50.5}Ti_{36.2}Hf_{13.3}$ shape memory alloy. Scripta Mater 2016;118:51–4.
[22] Patriarca L, Wu Y, Sehitoglu H, Chumlyakov Y. High temperature shape memory behavior of $Ni_{50.3}Ti_{25}Hf_{24.7}$ single crystals. Scripta Mater 2016;115:133–6.
[23] Nemat-Nasser S, Choi J-Y, Guo W-G, Isaacs JB. Very high strain-rate response of a NiTi shape-memory alloy. Mech Mater 2005;37:287–98.
[24] Sehitoglu H, Karaman I, Anderson R, Zhang X, Gall K, Maier H, et al. Compressive response of NiTi single crystals. Acta Mater 2000;48:3311–26.
[25] Kimiecik M, Jones JW, Daly S. The effect of microstructure on stress-induced martensitic transformation under cyclic loading in the SMA Nickel-Titanium. J Mech Phys Solids 2016;89:16–30.
[26] Yawny A, Sade M, Eggeler G. Pseudoelastic cycling of ultra-fine-grained NiTi shape-memory wires. Zeitschrift für metallkunde 2005;96:608–18.
[27] Eucken S, Duerig TW. The effects of pseudoelastic prestraining on the tensile behaviour and two-way shape memory effect in aged NiTi. Acta Metall 1989;37:2245–52.
[28] Kimiecik M, Jones JW, Daly S. Grain orientation dependence of phase transformation in the shape memory alloy Nickel-Titanium. Acta Mater 2015;94:214–23.
[29] Sedmák P, Šittner P, Pilch J, Curfs C. Instability of cyclic superelastic deformation of NiTi investigated by synchrotron X-ray diffraction. Acta Mater 2015;94:257–70.
[30] Kang G. Advances in transformation ratcheting and ratcheting-fatigue interaction of NiTi shape memory alloy. Acta Mech Solida Sin 2013;26:221–36.
[31] Frick CP, Clark BG, Schneider AS, Maaß R, Van Petegem S, Van Swygenhoven H. On the plasticity of small-scale nickel–titanium shape memory alloys. Scripta Mater 2010;62:492–5.

[32] Pfetzing-Micklich J, Ghisleni R, Simon T, Somsen C, Michler J, Eggeler G. Orientation dependence of stress-induced phase transformation and dislocation plasticity in NiTi shape memory alloys on the micro scale. Mater Sci Eng, A 2012;538:265–71.
[33] Novák V, Šittner P, Pilch J, Delville R. Effect of plastic slip on thermomechanical behavior of NiTi polycrystals investigated by micromechanics modelling. In: European symposium on martensitic transformations. EDP Sciences; 2009. p. 03009.
[34] Richards AW, Lebensohn R, Bhattacharya K. Interplay of martensitic phase transformation and plastic slip in polycrystals. Acta Mater 2013;61:4384–97.
[35] Huang X, Ackland GJ, Rabe KM. Crystal structures and shape-memory behaviour of NiTi. Nat Mater 2003;2:307–11.
[36] Barman S, Chakrabarti A, Singh S, Banik S, Bhardwaj S, Paulose P, et al. Theoretical prediction and experimental study of a ferromagnetic shape memory alloy: Ga_2MnNi. Phys Rev B 2008;78:134406.
[37] Schoeck G. Peierls energy of dislocations: a critical assessment. Phys Rev Lett 1999;82:2310.
[38] Rice JR. Dislocation nucleation from a crack tip: an analysis based on the Peierls concept. J Mech Phys Solids 1992;40:239–71.
[39] Vitek V. Intrinsic stacking faults in body-centred cubic crystals. Phil Mag 1968;18:773–86.
[40] Lu G, Kioussis N, Bulatov VV, Kaxiras E. Generalized-stacking-fault energy surface and dislocation properties of aluminum. Phys Rev B 2000;62:3099.
[41] Chowdhury P, Sehitoglu H, Abuzaid W, Maier H. Mechanical response of low stacking fault energy Co–Ni alloys–continuum, mesoscopic and atomic level treatments. Int J Plast 2015;71:32–61.
[42] Hirth JP, Lothe J. Theory of dislocations; 1982.
[43] Hosford WF. Mechanical behavior of materials. Cambridge University Press; 2010.
[44] Chowdhury P, Sehitoglu H, Maier HJ, Rateick R. Strength prediction in NiCo alloys–the role of composition and nanotwins. Int J Plast 2015;79:237–58.
[45] Otsuka H, Yamada H, Maruyama T, Tanahashi H, Matsuda S, Murakami M. Effects of alloying additions on Fe-Mn-Si shape memory alloys. ISIJ Int 1990;30:674–9.
[46] Hull D, Bacon DJ. Introduction to dislocations. Oxford: Pergamon Press; 1984.
[47] Neuhäuser H, Schwink C. Solid solution strengthening. Mater Sci Technol 1993:193–250.
[48] Pfeiler W. Alloy physics: a comprehensive reference. John Wiley & Sons; 2008.
[49] Uijttewaal M, Hickel T, Neugebauer J, Gruner ME, Entel P. Understanding the phase transitions of the Ni_2MnGa magnetic shape memory system from first principles. Phys Rev Lett 2009;102:035702.
[50] Planes A, Mañosa L, Acet M. Magnetocaloric effect and its relation to shape-memory properties in ferromagnetic Heusler alloys. J Phys: Condens Matter 2009;21:233201.
[51] Siewert M, Gruner ME, Dannenberg A, Chakrabarti A, Herper HC, Wuttig M, et al. Designing shape-memory Heusler alloys from first-principles. Appl Phys Lett 2011;99:191904.
[52] Özdemir Kart S, Karaman I. DFT studies on structure, mechanics and phase behavior of magnetic shape memory alloys: Ni_2MnGa. Phys Status Solidi (a) 2008;205:1026–35.
[53] Entel P, Buchelnikov VD, Khovailo VV, Zayak AT, Adeagbo WA, Gruner ME, et al. Modelling the phase diagram of magnetic shape memory Heusler alloys. J Phys D Appl Phys 2006;39:865.
[54] Ito W, Nagasako M, Umetsu RY, Kainuma R, Kanomata T, Ishida K. Atomic ordering and magnetic properties in the $Ni_{45}Co_5Mn_{36.7}In_{13.3}$ metamagnetic shape memory alloy. Appl Phys Lett 2008;93:1–232503.
[55] Chowdhury P, Sehitoglu H. Significance of slip propensity determination in shape memory alloys. Scripta Mater 2016;119:82–7.
[56] Ojha A, Sehitoglu H. Slip resistance of Ti-based high-temperature shape memory alloys. Shape Mem Superelast 2016;2:50–61.
[57] Sehitoglu H, Wang J, Maier H. Transformation and slip behavior of Ni_2FeGa. Int J Plast 2012;39:61–74.
[58] Wang J, Sehitoglu H. Modelling of martensite slip and twinning in NiTiHf shape memory alloys. Phil Mag 2014;94:2297–317.
[59] Wang J, Sehitoglu H, Maier H. Dislocation slip stress prediction in shape memory alloys. Int J Plast 2014;54:247–66.
[60] Peierls R. The size of a dislocation. Proc Phys Soc 1940;52:34.
[61] Nabarro F. Dislocations in a simple cubic lattice. Proc Phys Soc 1947;59:256.
[62] Chowdhury P. Modeling mechanical properties–linking atomistics to continuum. Urbana-Champaign: University of Illinois; 2016.
[63] Gall K, Sehitoglu H, Anderson R, Karaman I, Chumlyakov YI, Kireeva IV. On the mechanical behavior of single crystal NiTi shape memory alloys and related polycrystalline phenomenon. Mater Sci Eng, A 2001;317:85–92.
[64] Liu Y, Xie Z, Van Humbeeck J, Delaey L. Deformation of shape memory alloys associated with twinned domain re-configurations. Mater Sci Eng, A 1999;273:679–84.
[65] Xie Z, Liu Y, Van Humbeeck J. Microstructure of NiTi shape memory alloy due to tension–compression cyclic deformation. Acta Mater 1998;46:1989–2000.
[66] Miyazaki S, Otsuka K, Wayman C. The shape memory mechanism associated with the martensitic transformation in Ti-Ni alloys—I. Self-accommodation. Acta Metall 1989;37:1873–84.
[67] Waitz T. The self-accommodated morphology of martensite in nanocrystalline NiTi shape memory alloys. Acta Mater 2005;53:2273–83.
[68] Liu Y, Xie Z, Humbeeck JV, Delaey L, Liu Y. On the deformation of the twinned domain in NiTi shape memory alloys. Philos Mag A 2000;80:1935–53.
[69] Liu Y, Xie Z. Twinning and detwinning of⟨0 1 1⟩ type II twin in shape memory alloy. Acta Mater 2003;51:5529–43.
[70] McKelvey AL, Ritchie RO. On the temperature dependence of the superelastic strength and the prediction of the theoretical uniaxial transformation strain in Nitinol. Philos Mag A 2000;80:1759–68.
[71] Miyazaki S, Otsuka K, Suzuki Y. Transformation pseudoelasticity and deformation behavior in a Ti-50.6 at.% Ni alloy. Scr Metall 1981;15:287–92.
[72] McCormick J, Tyber J, DesRoches R, Gall K, Maier HJ. Structural engineering with NiTi. II: mechanical behavior and scaling. J Eng Mech 2007;133:1019–29.
[73] Dilibal S, Sehitoglu H, Hamilton R, Maier H, Chumlyakov Y. On the volume change in Co–Ni–Al during pseudoelasticity. Mater Sci Eng, A 2011;528:2875–81.
[74] Hamilton R, Dilibal S, Sehitoglu H, Maier H. Underlying mechanism of dual hysteresis in NiMnGa single crystals. Mater Sci Eng, A 2011;528:1877–81.
[75] Karaca HE, Karaman I, Basaran B, Ren Y, Chumlyakov YI, Maier HJ. Magnetic field-induced phase transformation in NiMnCoIn magnetic shape-memory alloys—a new actuation mechanism with large work output. Adv Funct Mater 2009;19:983–98.
[76] Otsuka K, Sakamoto H, Shimizu K. Successive stress-induced martensitic transformations and associated transformation pseudoelasticity in Cu-Al-Ni alloys. Acta Metall 1979;27:585–601.
[77] Miyazaki S, Kimura S, Otsuka K. Shape-memory effect and pseudoelasticity associated with the R-phase transition in Ti-50 5 at.% Ni single crystals. Philos Mag A 1988;57:467–78.
[78] Karaca H, Karaman I, Chumlyakov Y, Lagoudas D, Zhang X. Compressive response of a single crystalline CoNiAl shape memory alloy. Scripta Mater 2004;51:261–6.
[79] Hamilton R, Sehitoglu H, Efstathiou C, Maier H. Inter-martensitic transitions in Ni–Fe–Ga single crystals. Acta Mater 2007;55:4867–76.
[80] Delaey L, Krishnan R, Tas H, Warlimont H. Thermoelasticity, pseudoelasticity and the memory effects associated with martensitic transformations. J Mater Sci 1974;9:1521–35.
[81] Kockar B, Karaman I, Kim J, Chumlyakov Y, Sharp J, Yu C-JM. Thermomechanical cyclic response of an ultrafine-grained NiTi shape memory alloy. Acta Mater 2008;56:3630–46.
[82] Lu G, Kioussis N, Bulatov VV, Kaxiras E. The peierls-nabarro model revisited. Philos Mag Lett 2000;80:675–82.
[83] Melton K, Mercier O. Fatigue of NiTi thermoelastic martensites. Acta Metall 1979;27:137–44.
[84] Miyazaki S, Imai T, Igo Y, Otsuka K. Effect of cyclic deformation on the pseudoelasticity characteristics of Ti-Ni alloys. Metall Trans A 1986;17:115–20.

[85] Prokoshkin S, Khmelevskaya IY, Dobatkin S, Trubitsyna I, Tatyanin E, Stolyarov V, et al. Alloy composition, deformation temperature, pressure and post-deformation annealing effects in severely deformed Ti–Ni based shape memory alloys. Acta Mater 2005;53:2703–14.
[86] Strnadel B, Ohashi S, Ohtsuka H, Ishihara T, Miyazaki S. Cyclic stress-strain characteristics of Ti-Ni and Ti-Ni-Cu shape memory alloys. Mater Sci Eng, A 1995;202:148–56.
[87] Strnadel B, Ohashi S, Ohtsuka H, Miyazaki S, Ishihara T. Effect of mechanical cycling on the pseudoelasticity characteristics of Ti-Ni and Ti-Ni-Cu alloys. Mater Sci Eng, A 1995;203:187–96.
[88] Nemat-Nasser S, Choi JY. Strain rate dependence of deformation mechanisms in a Ni–Ti–Cr shape-memory alloy. Acta Mater 2005;53:449–54.
[89] Surikova N, Chumlyakov YI. Mechanisms of plastic deformation in titanium nickelide single crystals; 2000.
[90] Tyumentsev A, Surikova N, Litovchenko IY, Pinzhin YP, Korotaev A, Lysenko O. Mechanism of deformation and crystal lattice reorientation in strain localization bands and deformation twins of the B2 phase of titanium nickelide. Acta Mater 2004;52:2067–74.
[91] Adharapurapu RR, Jiang F, Vecchio KS, Gray GT. Response of NiTi shape memory alloy at high strain rate: a systematic investigation of temperature effects on tension–compression asymmetry. Acta Mater 2006;54:4609–20.
[92] Bowers M, Chen X, De Graef M, Anderson PM, Mills M. Characterization and modeling of defects generated in pseudoelastically deformed NiTi microcrystals. Scripta Mater 2014;78:69–72.
[93] Song Y, Chen X, Dabade V, Shield TW, James RD. Enhanced reversibility and unusual microstructure of a phase-transforming material. Nature 2013;502:85–8.
[94] Lagoudas DC, Entchev PB, Popov P, Patoor E, Brinson LC, Gao X. Shape memory alloys, part II: modeling of polycrystals. Mech Mater 2006;38:430–62.
[95] Gall K, Sehitoglu H. The role of texture in tension–compression asymmetry in polycrystalline NiTi. Int J Plast 1999;15:69–92.
[96] Waitz T, Antretter T, Fischer F, Simha N, Karnthaler H. Size effects on the martensitic phase transformation of NiTi nanograins. J Mech Phys Solids 2007;55:419–44.
[97] Liu Y, Xie ZL, Van Humbeeck J, Delaey L. Effect of texture orientation on the martensite deformation of NiTi shape memory alloy sheet. Acta Mater 1999;47:645–60.
[98] Wu Y, Patriarca L, Li G, Sehitoglu H, Soejima Y, Ito T, et al. Shape memory response of polycrystalline NiTi12∗ 5Hf alloy: transformation at small scales. Shape Mem Superelast 2015;1:387–97.
[99] Gruner ME, Entel P, Opahle I, Richter M. Ab initio investigation of twin boundary motion in the magnetic shape memory Heusler alloy Ni_2MnGa. J Mater Sci 2008;43:3825–31.
[100] Patoor E, Lagoudas DC, Entchev PB, Brinson LC, Gao X. Shape memory alloys, part I: general properties and modeling of single crystals. Mech Mater 2006;38:391–429.
[101] Hamilton R, Sehitoglu H, Chumlyakov Y, Maier H. Stress dependence of the hysteresis in single crystal NiTi alloys. Acta Mater 2004;52:3383–402.
[102] Dadda J, Maier H, Karaman I, Karaca H, Chumlyakov YI. Pseudoelasticity at elevated temperatures in [001] oriented $Co_{49}Ni_{21}Ga_{30}$ single crystals under compression. Scripta Mater 2006;55:663–6.
[103] Liu Y, Xie Z. Detwinning in shape memory alloy. Progress in smart materials and structures. Nova Science Publishers Inc; 2007. p. 29–65.
[104] Lopez H, Salinas A, Calderon H. Plastic straining effects on the microstructure of a Ti-rich NiTi shape memory alloy. Metall Mater Trans A 2001;32:717–29.
[105] Tadmor EB, Miller RE. Modeling materials: continuum, atomistic and multiscale techniques. Cambridge University Press; 2011.
[106] Ezaz T, Wang J, Sehitoglu H, Maier H. Plastic deformation of NiTi shape memory alloys. Acta Mater 2013;61:67–78.
[107] Hatcher N, Kontsevoi OY, Freeman A. Role of elastic and shear stabilities in the martensitic transformation path of NiTi. Phys Rev B 2009;80:144203.
[108] Kibey SA. Mesoscale models for stacking faults, deformation twins and martensitic transformations: linking atomistics to continuum. ProQuest; 2007.
[109] Engel E, Dreizler RM. Relativistic density functional theory. Density Funct Theory 2011:351–99.
[110] Dreizler RM, Engel E. Density functional theory. Springer; 2011.
[111] Cheng B, Ngan AH. The crystal structures of sintered copper nanoparticles: a molecular dynamics study. Int J Plast 2013;47:65–79.
[112] Büsgen T, Feydt J, Hassdorf R, Thienhaus S, Moske M, Boese M, et al. Ab initio calculations of structure and lattice dynamics in Ni−Mn−Al shape memory alloys. Phys Rev B 2004;70:014111.
[113] Buehler WJ, Gilfrich J, Wiley R. Effect of low-temperature phase changes on the mechanical properties of alloys near composition TiNi. J Appl Phys 1963;34:1475–7.
[114] Pelton A, Huang G, Moine P, Sinclair R. Effects of thermal cycling on microstructure and properties in Nitinol. Mater Sci Eng, A 2012;532:130–8.
[115] Liu Y, Xie Z, Van Humbeeck J, Delaey L. Asymmetry of stress–strain curves under tension and compression for NiTi shape memory alloys. Acta Mater 1998;46:4325–38.
[116] Chumlyakov Y, Kireeva I, Panchenko E, Karaman I, Maier HJ, Timofeeva E. Shape memory effect and high-temperature superelasticity in high-strength single crystals. J Alloy Compd 2013;577:S393–8.
[117] Sehitoglu H, Jun J, Zhang X, Karaman I, Chumlyakov Y, Maier HJ, et al. Shape memory and pseudoelastic behavior of 51.5% Ni–Ti single crystals in solutionized and overaged state. Acta Mater 2001;49:3609–20.
[118] Ishida A, Takei A, Sato M, Miyazaki S. Shape memory behavior of Ti-Ni thin films annealed at various temperatures. MRS Proceedings. Cambridge Univ Press; 1994. p. 381.
[119] Benafan O, Noebe RD, Padula SA, Brown DW, Vogel S, Vaidyanathan R. Thermomechanical cycling of a NiTi shape memory alloy-macroscopic response and microstructural evolution. Int J Plast 2014;56:99–118.
[120] Miller DA, Lagoudas DC. Influence of cold work and heat treatment on the shape memory effect and plastic strain development of NiTi. Mater Sci Eng, A 2001;308:161–75.
[121] Mercier O, Melton KN, Gremaud G, Hägi J. Single-crystal elastic constants of the equiatomic NiTi alloy near the martensitic transformation. J Appl Phys 1980;51:1833–4.
[122] Van Swygenhoven H, Derlet PM, Frøseth AG. Stacking fault energies and slip in nanocrystalline metals. Nat Mater 2004;3:399–403.
[123] Siegel DJ. Generalized stacking fault energies, ductilities, and twinnabilities of Ni and selected Ni alloys. Appl Phys Lett 2005;87:121901.
[124] Stoloff N, Davies R. The plastic deformation of ordered FeCo and Fe_3Al alloys. Acta Metall 1964;12:473–85.
[125] Chumlyakov YI, Kireeva I, Panchenko EY, Timofeeva E, Pobedennaya Z, Chusov S, et al. High-temperature superelasticity in CoNiGa, CoNiAl, NiFeGa, and TiNi monocrystals. Russ Phys J 2008;51:1016–36.
[126] Timofeeva E, Panchenko EY, Chumlyakov YI, Maier H. Development of thermoelastic martensitic transformations in ferromagnetic [011]-oriented NiFeGa single crystals in compression. Russ Phys J 2012;1–4.
[127] Timofeeva E, Panchenko EY, Chumlyakov YI, Tagiltsev A. Intermartensitic thermoelastic transformations in [012]-oriented single crystals of ferromagnetic NiFeGa alloys under compressive loading. Russ Phys J 2015;57:1268–77.
[128] Hamilton R, Sehitoglu H, Efstathiou C, Maier H. Mechanical response of NiFeGa alloys containing second-phase particles. Scripta Mater 2007;57:497–9.
[129] Efstathiou C, Sehitoglu H, Carroll J, Lambros J, Maier H. Full-field strain evolution during intermartensitic transformations in single-crystal NiFeGa. Acta Mater 2008;56:3791–9.
[130] Masdeu F, Pons J, Segui C, Cesari E, Dutkiewicz J. Some features of Ni–Fe–Ga shape memory alloys under compression. J Magn Magn Mater 2005;290:816–9.
[131] Sutou Y, Kamiya N, Omori T, Kainuma R, Ishida K, Oikawa K. Stress-strain characteristics in Ni–Ga–Fe ferromagnetic shape memory alloys. Appl Phys Lett 2004;84:1275–7.
[132] Ehmann J, Fähnle M. Generalized stacking-fault energies for TiAl: mechanical instability of the (1 1 1) antiphase boundary. Philos Mag A 1998;77:701–14.

[133] Liu Y, Liu L, Wang S, Ye H. First-principles study of shear deformation in TiAl and Ti_3Al. Intermetallics 2007;15:428–35.
[134] Paidar V. Behaviour of dislocations in TiAl intermetallics. Mater Sci Eng, A 2004;387:977–80.
[135] Golberg D, Xu Y, Murakami Y, Morito S, Otsuka K, Ueki T, et al. Characteristics of $Ti_{50}Pd_{30}$ Ni_{20} high-temperature shape memory alloy. Intermetallics 1995;3:35–46.
[136] Golberg D, Xu Y, Murakami Y, Otsuka K, Ueki T, Horikawa H. High-temperature shape memory effect in $Ti_{50}Pd_{50-x}Ni_x$ (x = 10, 15, 20) alloys. Mater Lett 1995;22:241–8.
[137] Bigelow GS, Padula II SA, Garg A, Gaydosh D, Noebe RD. Characterization of ternary NiTiPd high-temperature shape-memory alloys under load-biased thermal cycling. Metall Mater Trans A 2010;41:3065–79.
[138] Kumar PK, Lagoudas DC. Experimental and microstructural characterization of simultaneous creep, plasticity and phase transformation in $Ti_{50}Pd_{40}Ni_{10}$ high-temperature shape memory alloy. Acta Mater 2010;58:1618–28.
[139] Cai W, Tanaka S, Otsuka K. Thermal cyclic characteristics under load in a $Ti_{50.6}Pd_{30}Ni_{19.4}$ alloy. Materials science forum. Trans Tech Publ; 2000. p. 279–82.
[140] Otsuka K, Oda K, Ueno Y, Piao M, Ueki T, Horikawa H. The shape memory effect in a $Ti_{50}Pd_{50}$ alloy. Scr Metall Mater 1993;29:1355–8.
[141] Hornbogen E. Ausforming of NiTi. J Mater Sci 1999;34:599–606.
[142] Kockar B, Karaman I, Kim J, Chumlyakov Y. A method to enhance cyclic reversibility of NiTiHf high temperature shape memory alloys. Scripta Mater 2006;54:2203–8.
[143] Shimizu S, Xu Y, Okunishi E, Tanaka S, Otsuka K, Mitose K. Improvement of shape memory characteristics by precipitation-hardening of Ti·Pd·Ni alloys. Mater Lett 1998;34:23–9.
[144] Yang WS, Mikkola D. Ductilization of Ti-Ni-Pd shape memory alloys with boron additions. Scr Metall Mater 1993;28:161–5.
[145] Kockar B, Atli K, Ma J, Haouaoui M, Karaman I, Nagasako M, et al. Role of severe plastic deformation on the cyclic reversibility of a $Ti_{50.3}Ni_{33.7}Pd_{16}$ high temperature shape memory alloy. Acta Mater 2010;58:6411–20.
[146] Lin B, Gall K, Maier HJ, Waldron R. Structure and thermomechanical behavior of NiTiPt shape memory alloy wires. Acta Biomater 2009;5:257–67.
[147] Rios O, Noebe R, Biles T, Garg A, Palczer A, Scheiman D, et al. Characterization of ternary NiTiPt high-temperature shape memory alloys. Smart Structures and Materials. International Society for Optics and Photonics; 2005. p. 376–87.
[148] Noebe R, Draper S, Gaydosh D, Garga A, Lerch B, Penney N, et al. Effect of thermomechanical processing on the microstructure, properties, and work behavior of a $Ti_{50.5}Ni_{29.5}Pt_{20}$. High-Temp Shape Memory Alloy 2006.
[149] Hatcher N, Kontsevoi OY, Freeman A. Structural stabilities, elastic constants, generalized stacking fault energetics, and the martensitic transformation mechanisms for the $Ni_{50-x}TiPt_x$ (x = 0–30) ternary system: ab initio investigation. In: European symposium on martensitic transformations. EDP Sciences; 2009. p. 02010.
[150] Hatcher NB. Electronic and phononic origins of martensitic behavior in nickel titanium-based binary and ternary shape memory alloys; 2010.
[151] Karaca H, Saghaian S, Ded G, Tobe H, Basaran B, Maier H, et al. Effects of nanoprecipitation on the shape memory and material properties of an Ni-rich NiTiHf high temperature shape memory alloy. Acta Mater 2013;61:7422–31.
[152] Coughlin D, Phillips P, Bigelow G, Garg A, Noebe R, Mills M. Characterization of the microstructure and mechanical properties of a 50.3Ni–29.7Ti–20Hf shape memory alloy. Scripta Mater 2012;67:112–5.
[153] Kim HY, Fu J, Tobe H, Kim JI, Miyazaki S. Crystal structure, transformation strain, and superelastic property of Ti–Nb–Zr and Ti–Nb–Ta alloys. Shape Mem Superelast 2015;1:107–16.
[154] Kim J, Kim H, Inamura T, Hosoda H, Miyazaki S. Shape memory characteristics of Ti–22Nb–(2–8) Zr (at.%) biomedical alloys. Mater Sci Eng, A 2005;403:334–9.
[155] Sehitoglu H, Patriarca L, Wu Y. Shape memory strains and temperatures in the extreme. Curr Opin Solid State Mater Sci 2016. doi: http://dx.doi.org/10.1016/j.cossms.2016.06.005 (in press).
[156] Ogata S, Li J, Yip S. Ideal pure shear strength of aluminum and copper. Science 2002;298:807–11.
[157] Carrez P, Cordier P, Mainprice D, Tommasi A. Slip systems and plastic shear anisotropy in Mg_2SiO_4 ringwoodite insights from numerical modelling. Eur J Mineral 2006;18:149–60.
[158] Hartford J, Von Sydow B, Wahnström G, Lundqvist B. Peierls barriers and stresses for edge dislocations in Pd and Al calculated from first principles. Phys Rev B 1998;58:2487.
[159] Joos B, Ren Q, Duesbery M. Peierls-Nabarro model of dislocations in silicon with generalized stacking-fault restoring forces. Phys Rev B 1994;50:5890.
[160] Schoeck G. The generalized Peierls-Nabarro model. Philos Mag A 1994;69:1085–95.
[161] Schoeck G. The Peierls model: progress and limitations. Mater Sci Eng, A 2005;400:7–17.
[162] Crawford R, Ray I, Cockayne D. The weak-beam technique applied to superlattice dislocations in iron-aluminium alloys: II. Fourfold dissociation in do3-type order. Phil Mag 1973;27:1–7.
[163] Stroh A. Dislocations and cracks in anisotropic elasticity. Phil Mag 1958;3:625–46.
[164] Efstathiou C, Sehitoglu H. Local transformation strain measurements in precipitated NiTi single crystals. Scripta Mater 2008;59:1263–6.
[165] Sehitoglu H, Jun J, Zhang X, Karaman I, Chumlyakov Y, Maier H, et al. Shape memory and pseudoelastic behavior of 51.5% Ni–Ti single crystals in solutionized and overaged state. Acta Mater 2001;49:3609–20.
[166] Chumlyakov YI, Kireeva I, Panchenko EY, Kirillov V, Timofeeva E, Kretinina I, et al. Thermoelastic martensitic transformations in single crystals with disperse particles. Russ Phys J 2012;54:937–50.
[167] Karaman I, Lagoudas DC. Magnetic shape memory alloys with high actuation forces. DTIC Document; 2006.
[168] Romero R, Lovey F, Ahlers M. Plasticity in β phase Cu-Zn-Al alloys. Philos Mag A 1988;58:881–903.
[169] Wollmershauser J, Kabra S, Agnew S. In situ neutron diffraction study of the plastic deformation mechanisms of B2 ordered intermetallic alloys: NiAl, CuZn, and CeAg. Acta Mater 2009;57:213–23.
[170] Otsuka K, Wayman C. Mechanism of shape memory effect and superelasticity. Shape Mem Mater 1998:27–49.
[171] Damiani C, Lovey F, Sade M. Plastic deformation under compression of Cu–Zn–Al martensitic single crystals. Mater Sci Eng, A 2002;323:436–44.
[172] Malarría J, Lovey F, Sade M. Two way shape memory effect in CuZnAl single crystals after pseudoelastic cycling at low temperatures. Mater Sci Eng, A 2009;517:118–24.
[173] Roqueta D, Lovey F, Sade M. Hysteresis evolution in the martensitic transformation cycling in β-Cu-Zn-Al samples with γ-phase precipitates. Scripta Mater 1997;36:385–91.
[174] Sade M, Hazarabedian A, Uribarri A, Lovey F. Effects of cycling through stress-induced martensitic transformation in Cu–Zn–Al alloys on dislocation structures and two-way memory. Phase Transformations'87. 1987:279–81.
[175] Šittner P, Novák V, Zárubová N. Martensitic transformations in [001] CuAlZnMn single crystals. Acta Mater 1998;46:1265–81.
[176] Tsuzaki K, Natsume Y, Kurokawa Y, Maki T. Improvement of the shape memory effect in Fe-Mn-Si alloys by the addition of carbon. Scr Metall Mater 1992;27:471–3.
[177] Jost N. Thermal fatigue of Fe–Ni–Co–Ti shape-memory-alloys. Mater Sci Eng, A 1999;273:649–53.
[178] Morito S, Moritani T, Furuhara T, Maki T. Martensitic transformation in thin foils of an Fe-Ni-Co-Ti shape memory alloy. Materials science forum. Trans Tech Publ; 2000. p. 207–10.
[179] Tsuzaki K, Ikegami M, Tomota Y, Kurokawa Y, Nakagawara W, Maki T. Effect of thermal cycling on the martensitic transformation in an Fe–24Mn–6Si shape memory alloy. Mater Trans, JIM 1992;33:263–70.
[180] Bartel T, Menzel A, Svendsen B. Thermodynamic and relaxation-based modeling of the interaction between martensitic phase transformations and plasticity. J Mech Phys Solids 2011;59:1004–19.

[181] Idesman AV, Levitas VI, Stein E. Structural changes in elastoplastic material: a unified finite-element approach to phase transformation, twinning and fracture. Int J Plast 2000;16:893–949.
[182] Levitas VI. Critical thought experiment to choose the driving force for interface propagation in inelastic materials. Int J Plast 2002;18:1499–525.
[183] Otsuka K, Ren X. Physical metallurgy of Ti–Ni-based shape memory alloys. Prog Mater Sci 2005;50:511–678.
[184] Olson G, Cohen M. Thermoelastic behavior in martensitic transformations. Scr Metall 1975;9:1247–54.
[185] Duerig T. Some unsolved aspects of Nitinol. Mater Sci Eng, A 2006;438:69–74.
[186] Kelly A, Groves GW, Kidd P. Crystallography and crystal defects. John Wiley & Sons; 2000.
[187] Moberly W, Proft J, Duerig T, Sinclair R. Deformation, twinning and thermo-mechanical strengthening of $Ti_{50}Ni_{47}Fe_3$. Acta Metall Mater 1990;38:2601–12.
[188] Taylor GI. The mechanism of plastic deformation of crystals. Part I. Theoretical. Proc R Soc Lond Ser A, Contain Pap Math Phys Charact 1934;145:362–87.
[189] Ardley G, Cottrell A. Yield points in brass crystals. Proc R Soc Lond A: Math, Phys Eng Sci: R Soc 1953:328–41.
[190] Omori T, Kamiya N, Sutou Y, Oikawa K, Kainuma R, Ishida K. Phase transformations in Ni–Ga–Fe ferromagnetic shape memory alloys. Mater Sci Eng, A 2004;378:403–8.
[191] Barandiarán J, Gutiérrez J, Lázpita P, Chernenko V, Seguí C, Pons J, et al. Martensitic transformation in Ni–Fe–Ga alloys. Mater Sci Eng, A 2008;478:125–9.
[192] Oikawa K, Ota T, Ohmori T, Tanaka Y, Morito H, Fujita A, et al. Magnetic and martensitic phase transitions in ferromagnetic Ni–Ga–Fe shape memory alloys. Appl Phys Lett 2002;81:5201–3.
[193] Rachinger W, Cottrell A. Slip in crystals of the caesium chloride type. Acta Metall 1956;4:109–13.
[194] Slater JC. Atomic radii in crystals. J Chem Phys 1964;41:3199–204.
[195] Kim H, Hashimoto S, Kim J, Inamura T, Hosoda H, Miyazaki S. Effect of Ta addition on shape memory behavior of Ti–22Nb alloy. Mater Sci Eng, A 2006;417:120–8.
[196] Kim H, Ikehara Y, Kim J, Hosoda H, Miyazaki S. Martensitic transformation, shape memory effect and superelasticity of Ti–Nb binary alloys. Acta Mater 2006;54:2419–29.
[197] Chumlyakov YI, Kireeva I, Panchenko EY, Timofeeva EE, Kretinina I, Kuts O, et al. Shape memory effect and superelasticity in single crystals of high-strength ferromagnetic alloys. Advanced materials research. Trans Tech Publ; 2014. p. 15–22.
[198] Tanaka Y, Himuro Y, Kainuma R, Sutou Y, Omori T, Ishida K. Ferrous polycrystalline shape-memory alloy showing huge superelasticity. Science 2010;327:1488–90.
[199] Khalil-Allafi J, Dlouhy A, Eggeler G. Ni_4Ti_3-precipitation during aging of NiTi shape memory alloys and its influence on martensitic phase transformations. Acta Mater 2002;50:4255–74.
[200] Bataillard L, Bidaux JE, Gotthardt R. Interaction between microstructure and multiple-step transformation in binary NiTi alloys using in-situ transmission electron microscopy observations. Philos Mag A 1998;78:327–44.
[201] Tirry W, Schryvers D. Quantitative determination of strain fields around Ni_4Ti_3 precipitates in NiTi. Acta Mater 2005;53:1041–9.
[202] Gall K, Sehitoglu H, Chumlyakov YI, Kireeva IV, Maier HJ. The influence of aging on critical transformation stress levels and martensite start temperatures in NiTi: part II—discussion of experimental results. J Eng Mater Technol 1999;121:28–37.
[203] Treppmann D, Hornbogen E, Wurzel D. The effect of combined recrystallization and precipitation processes on the functional and structural properties in NiTi alloys. J Phys IV 1995;5. C8-569–C8-74.
[204] Chowdhury P, Ren G, Sehitoglu H. NiTi superelasticity via atomistic simulations. Philos Mag Lett 2015:1–13.
[205] Zhong Y, Gall K, Zhu T. Atomistic characterization of pseudoelasticity and shape memory in NiTi nanopillars. Acta Mater 2012;60:6301–11.
[206] Mutter D, Nielaba P. Simulation of the shape memory effect in a NiTi nano model system. J Alloy Compd 2013;577:S83–7.
[207] Lai W, Liu B. Lattice stability of some Ni-Ti alloy phases versus their chemical composition and disordering. J Phys: Condens Matter 2000;12:L53.
[208] Farkas D, Roqueta D, Vilette A, Ternes K. Atomistic simulations in ternary Ni-Ti-Al alloys. Modell Simul Mater Sci Eng 1996;4:359.
[209] Sato T, Saitoh K, Shinke N. Atomistic modelling of reversible phase transformations in Ni–Ti alloys: a molecular dynamics study. Mater Sci Eng, A 2008;481:250–3.
[210] Chowdhury P, Patriarca L, Ren G, Sehitoglu H. Molecular dynamics modeling of NiTi superelasticity in presence of nanoprecipitates. Int J Plast 2016;81:152–67.
[211] Wang J, Sehitoglu H. Dislocation slip and twinning in Ni-based L1 2 type alloys. Intermetallics 2014;52:20–31.
[212] Nembach E. Particle strengthening of metals and alloys; 1997.
[213] Wagner MFX, Windl W. Elastic anisotropy of Ni_4Ti_3 from first principles. Scripta Mater 2009;60:207–10.
[214] Tirry W, Schryvers D. Quantitative determination of strain fields around Ni_4Ti_3 precipitates in NiTi. Acta Mater 2005;53:1041–9.
[215] Yang Z, Tirry W, Schryvers D. Analytical TEM investigations on concentration gradients surrounding Ni_4Ti_3 precipitates in Ni–Ti shape memory material. Scripta Mater 2005;52:1129–34.
[216] Pfetzing-Micklich J, Somsen C, Dlouhy A, Begau C, Hartmaier A, Wagner MFX, et al. On the crystallographic anisotropy of nanoindentation in pseudoelastic NiTi. Acta Mater 2013;61:602–16.
[217] Eggeler G, Hornbogen E, Yawny A, Heckmann A, Wagner M. Structural and functional fatigue of NiTi shape memory alloys. Mater Sci Eng, A 2004;378:24–33.
[218] Robertson SW, Pelton AR, Ritchie RO. Mechanical fatigue and fracture of Nitinol. Int Mater Rev 2012;57:1–37.
[219] Wu Y, Ojha A, Patriarca L, Sehitoglu H. Fatigue crack growth fundamentals in shape memory alloys. Shape Mem Superelast 2015;1:18–40.
[220] Pelton A. Nitinol fatigue: a review of microstructures and mechanisms. J Mater Eng Perform 2011;20:613–7.
[221] Chowdhury P, Sehitoglu H. Mechanisms of fatigue crack growth–a critical digest of theoretical developments. Fatigue Fract Eng Mater Struct 2016;39 (6):652–74.
[222] Chowdhury P, Sehitoglu H, Rateick R. Recent advances in modeling fatigue cracks at microscale in the presence of high density coherent twin interfaces. Curr Opin Solid State Mater Sci 2016;20:140–50.
[223] McMeeking RM, Evans AG. Mechanics of transformation-toughening in brittle materials. J Am Ceram Soc 1982;65:242–6.
[224] Lexcellent C, Thiebaud F. Determination of the phase transformation zone at a crack tip in a shape memory alloy exhibiting asymmetry between tension and compression. Scripta Mater 2008;59:321–3.
[225] Stam G, van der Giessen E. Effect of reversible phase transformations on crack growth. Mech Mater 1995;21:51–71.
[226] Grujicic M, Dang P. Atomic-scale analysis of martensitic transformation in titanium alloyed with vanadium. Part II: molecular dynamics simulations. Mater Sci Eng, A 1996;205:153–65.
[227] Farkas D, Willemann M, Hyde B. Atomistic mechanisms of fatigue in nanocrystalline metals. Phys Rev Lett 2005;94:165502.
[228] Horstemeyer MF, Farkas D, Kim S, Tang T, Potirniche G. Nanostructurally small cracks (NSC): a review on atomistic modeling of fatigue. Int J Fatigue 2010;32:1473–502.
[229] Nishimura K, Miyazaki N. Molecular dynamics simulation of crack growth under cyclic loading. Comput Mater Sci 2004;31:269–78.
[230] Argon AS, Yip S. Molecular dynamics simulation of crack tip processes in alpha-iron and copper. J Appl Phys 1983;54:4864–78.
[231] Warner DH, Curtin WA, Qu S. Rate dependence of crack-tip processes predicts twinning trends in fcc metals. Nat Mater 2007;6:876–81.
[232] Tang T, Kim S, Horstemeyer MF. Fatigue crack growth in magnesium single crystals under cyclic loading: molecular dynamics simulation. Comput Mater Sci 2010;48:426–39.
[233] Ogata S, Li J, Yip S. Energy landscape of deformation twinning in bcc and fcc metals. Phys Rev B 2005;71:224102.
[234] Hatcher N, Kontsevoi OY, Freeman AJ. Martensitic transformation path of NiTi. Phys Rev B 2009;79:020202.

[235] Hai S, Tadmor EB. Deformation twinning at aluminum crack tips. Acta Mater 2003;51:117–31.
[236] Tadmor EB, Bernstein N. A first-principles measure for the twinnability of FCC metals. J Mech Phys Solids 2004;52:2507–19.
[237] Chowdhury PB, Sehitoglu H, Rateick RG, Maier HJ. Modeling fatigue crack growth resistance of nanocrystalline alloys. Acta Mater 2013;61:2531–47.
[238] Alkan S, Chowdhury P, Sehitoglu H, Rateick RG, Maier HJ. Role of nanotwins on fatigue crack growth resistance–experiments and theory. Int J Fatigue 2016;84:28–39.
[239] Chowdhury PB, Sehitoglu H, Rateick RG. Predicting fatigue resistance of nano-twinned materials: part I-Role of cyclic slip irreversibility and Peierls stress. Int J Fatigue 2014;68:277–91.
[240] Chowdhury PB, Sehitoglu H, Rateick RG. Predicting fatigue resistance of nano-twinned materials: part II–effective threshold stress intensity factor range. Int J Fatigue 2014;68:292–301.
[241] Chowdhury P. Fatigue crack growth (FCG) modeling in the presence of nano-obstacles. Urbana-Champaign: University of Illinois; 2011.
[242] Yu C, Kang G, Song D, Kan Q. Effect of martensite reorientation and reorientation-induced plasticity on multiaxial transformation ratchetting of superelastic NiTi shape memory alloy: new consideration in constitutive model. Int J Plast 2015;67:69–101.
[243] Thamburaja P, Anand L. Polycrystalline shape-memory materials: effect of crystallographic texture. J Mech Phys Solids 2001;49:709–37.
[244] Lagoudas DC, Entchev PB. Modeling of transformation-induced plasticity and its effect on the behavior of porous shape memory alloys. Part I: constitutive model for fully dense SMAs. Mech Mater 2004;36:865–92.
[245] Auricchio F, Taylor RL. Shape-memory alloys: modelling and numerical simulations of the finite-strain superelastic behavior. Comput Methods Appl Mech Eng 1997;143:175–94.
[246] Lu Z, Weng G. A self-consistent model for the stress–strain behavior of shape-memory alloy polycrystals. Acta Mater 1998;46:5423–33.
[247] Zaki W, Moumni Z. A three-dimensional model of the thermomechanical behavior of shape memory alloys. J Mech Phys Solids 2007;55:2455–90.